COLLISIONAL MOLECULAR ORIENTATION TRANSFER FACILITATED POLARIZATION SPECTRA OF THE $A^1\Sigma_u^+$ AND $b^3\Pi_u$ STATES OF THE $^{85}Rb_2$ AND Cs_2 DIMERS

A Dissertation
Submitted to
The Temple University Graduate Board

In Partial Fulfillment
of the Requirements for the Degree of
Doctor of Philosophy

Jianmei Bai
August, 2011

Examining committee members:

Marjatta Lyyra, Physics
Theodore Burkhardt, Physics
Peter Riseborough, Physics
Stephanie Wunder, Chemistry
Spiridoula Matsika, Chemistry

ABSTRACT

COLLISIONAL MOLECULAR ORIENTATION TRANSFER FACILITATED POLARIZATION SPECTRA OF THE $A^1\Sigma_u^+$ AND $b^3\Pi_u$ STATES OF THE $^{85}Rb_2$ AND Cs_2 DIMERS

By Jianmei Bai
Doctor of Philosophy
Temple University, 2011
Thesis Advisor: Dr. A. Marjatta Lyyra

The focus of this thesis is the study of the strongly perturbed $A^1\Sigma_u^+ \sim b^3\Pi_u$ complex of electronic states of the Rb_2 and Cs_2 dimers. Using collisional molecular orientation transfer facilitated high resolution V- type optical-optical double-resonance (OODR) polarization spectroscopy, it was possible to observe a much larger number of rovibrational levels in the $A^1\Sigma_u^+ \sim b^3\Pi_u$ complex of states than anticipated.

In addition to the direct *P, R* doublets, we have observed probe laser signals from a large number of collisionally populated rotational levels. Angular momentum changes up to ΔJ = 58 were observed in the recorded $^{85}Rb_2$ spectra. Observation of these satellite lines is based on transfer of both population and orientation from the rovibrational levels involved in the pump laser excitation to neighboring levels in a collision of the molecule with atomic perturbers.

The Discrete variable representation (DVR) method was used to analyze this data combined with other available data in a global deperturbation analysis of the spin-orbit interaction of the strongly perturbed $A^1\Sigma_u^+ \sim b^3\Pi_u$ complex of Rb_2 and Cs_2 electronic states. The resulting experimentally derived potential energy curves and internuclear distance dependent spin-orbit functions are presented in H. Salami et al., Phys. Rev. A**80**, 022515 (2009) and Jianmei Bai et al., Phys. Rev. A**83**, 032514 (2011). In addition, the analysis yields the term values of the rovibrational energy levels and their percentage of singlet and triplet character.

This work was supported by the National Science Foundation through awards PHY 0555608 and PHY 0855502.

ACKNOWLEDGEMENTS

First, let me express my sincere gratitude to my academic advisor, Professor Marjatta Lyyra, for her valuable academic advising and constant encouragement during my PhD study. I appreciate her kindness and hospitality from the bottom of my heart.

I am grateful to Dr. Ergin Ahmed for the training he gave me when I was new to the lab and for his help when I did the experiments. I would like to thank Professor John Huennekens and Professor Chin-Chun Tsai for their help with the theory and equipment in the lab. I wish to thank Professor Li Li for her encouragement. I also want to thank Professor Tom Bergeman for patiently spending a lot of time explaining the DVR program to me. I am grateful to Professor Ted Burkhardt, Professor Peter Riseborough, Professor Spiridoula Matsika, and Professor Setphanie Wunder for spending their precious time reading and revising my thesis.

I also thank Professor Jenny Magnes and her family for the friendship and encouragement they gave me. I feel happy whenever I think about the time I spent with Dr. Bediha Beser and Dr. Omer Salihoglu. I thank them so much for sharing the stress and the happiness with me, and they are my best friends.

I would like to thank our group members Yafei Guan, Derya Kanbur, Xinhua Pan and Aydin Sanli for their help. I also thank Seth Ashman and Chris Wolfe for their valuable advice and their help in the lab.

Last but not the least, I would like to give my deepest thanks to my family. I wish to thank my parents for their unconditional love and support and my brother, my sister-in-law and my lovely niece for their kindness. Deepest thanks to my husband Dr. Haisun Zhu for his constant encouragement and love.

To my parents:

Bai Lanhai and Sun Hongying

TABLE OF CONTENTS

LIST OF FIGURES

LIST OF TABLES

Page

CHAPTER 1

INTRODUCTION

The lowest electronically excited states of alkali dimers, namely the $A^1\Sigma_u^+$ and $b^3\Pi_u$ electronic states (see Figure 1), have been of interest for a long time because they can be used as 'window' states for the excitation of higher singlet or triplet states.

In this Thesis we use collisional orientation transfer facilitated V-type double-resonance polarization spectroscopy to record rovibrational energy level data for the strongly perturbed $A^1\Sigma_u^+ \sim b^3\Pi_u$ complex of electronic states of Rb_2 [1] and Cs_2 [2]. Observation of collisional orientation transfer in polarization spectroscopy was first reported by Schawlow et al. [3] with a buffer gas pressure of several hundred Torr. This led to a loss of spectral resolution, and much lower pressure is needed for the more dense spectra of the heavier alkali dimers. More recently, N. Okada and coworkers [4] observed collisional orientation transfer facilitated polarization spectra of $^{39}K^{85}Rb$ with much lower buffer gas pressure (0.5 Torr) and high resolution.

In this Thesis we utilize this technique for heavier molecules such as Cs_2 for which spectral congestion makes it difficult to find isolated pump transitions. One of the advantages of this approach is the enhanced yield of observed rotational energy levels through the many collisional satellite lines observed per single pump transition compared to the customary strong $\Delta J = \pm 1$ transitions. Another attractive aspect of this technique is

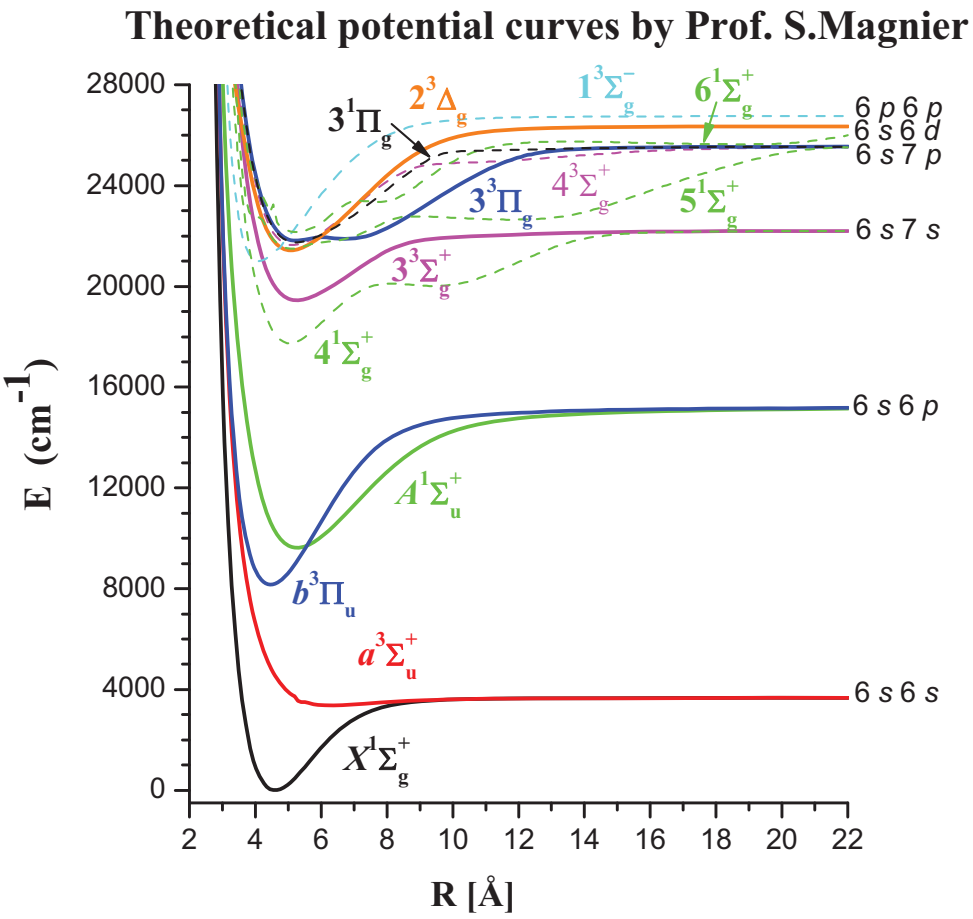

Figure 1.1 Theoretical potential curves of Cs_2 calculated by Prof. S. Magnier [5].

its high sensitivity. As a result we have been able to record spectra for Cs_2 in the probe laser scan range that was previously inaccessible due to very weak Franck-Condon factors from the thermal population of the $X^1\Sigma_g^+$ ground state.

This Thesis consists of 6 chapters. Chapter 2 gives an introduction to diatomic molecules. It starts with the Born-Oppenheimer approximation followed by the Schrodinger equation for the diatomic molecular system. The Rydberg-Klein-Rees (RKR) method for constructing molecular potential curves and Hund's coupling cases are introduced in this chapter. This chapter also includes a brief introduction to electric dipole selection rules for transitions between electronic states and the spin-orbit operator for molecular transitions. The spin-orbit coupling operator will be also described.

In Chapter 3 we describe different types of polarization spectroscopy. These include polarization spectroscopy with 1) a single tunable laser and 2) two independently tunable lasers including collisional transfer of molecular orientation. The advantages of the polarization technique are presented at the end of the chapter. In Chapter 4 we describe the setup with a brief description of the equipment used in the experiment.

In Chapter 5 we present the spectra of the Rb_2 and Cs_2 polarization experiments. Spectral lines due to collision-induced energy transfer with ΔJ up to 58 were observed in the Rb_2 spectra. With a very weak probe laser Franck-Condon factors, collisional satellite lines with ΔJ up to 12 were observed per vibrational level in the Cs_2 spectra.

Finally, Chapter 6 introduces the theoretical discrete variable representation (DVR) method for the analysis of the experimental data.

References:

1. Salami, H., Bergeman, T., Beser, B., Bai, J., Ahmed, E. H., Kotochigova, S., Lyyra, A. M., Huennekens, J., Lisdat, C., Stolyarov, A. V., Dulieu, O., Crozet, P., and Ross, A. J., Phys. Rev. A **80**, 022515 (2009).
2. Bai, J., Ahmed, E. H., Beser, B., Guan, Y., Kotochigova, S., Lyyra, A. M., Ashman, S., Wolfe, C. M., Huennekens, J., Xie, F., Li, D., Li, L., Tamanis, M., Ferber, R., Drozdova, A., Pazyuk, E. A., Stolyarov, A. V., Danzl, J. G., Nagerl, H. C., Bouloufa, N., Duleiu, O., Amiot, C., Salami, H., and Bergeman, T., Phys. Rev. A **83**, 032514 (2011).
3. Teets, R., Feinberg, R., Hansch, T. W., and Schawlow, A. L., Phys. Rev. Lett. **37** (11), 683 (1976).
4. Okada, N., Kasahara, S., Ebi, T., Baba, M., and Kato, H., J. Chem. Phys. **105**, 3458 (1996).
5. Private communication with Prof. S. Magnier.

CHAPTER 2

INTRODUCTION TO DIATOMIC MOLECULAR SPECTROSCOPY

2.1 Introduction to Diatomic Molecule

The experiments described in this thesis involve diatomic molecules, their energy levels, and perturbations such as the spin-orbit interaction.

Let's have a brief look at the properties of diatomic molecules. Each diatomic molecule consists of two atoms with internal degrees of motion such as rotation and vibration, which complicate the spectroscopy of molecules compared to that of atoms. The origins of molecular spectroscopy go back more than a century to the 1880s. It continues to play an important role in science and currently is at the heart of ultracold molecule formation research. In this context accurate spectroscopic determination of the energies of the rovibrational levels and their quantum state character is critical fundamental information.

2.2 Energy Level Structure of Diatomic Molecules

2.2.1 The Born – Oppenheimer Approximation

A molecule is a system that contains many electrons and nuclei. For example, Rb_2 molecule is composed of two Rubidium atoms, and each of them has 37 electrons. There are two Rubidium dimer isotopomers, $^{85}Rb_2$ and $^{87}Rb_2$. Quantum mechanically, it is

impossible to find an exact solution to a multi-body system like this. The mass of the nuclei is much higher than that of an electron, and therefore an electron moves much faster than a nucleus. As a result, the electrons follow the movement of the nuclei and quickly build up a new equilibrium. The Born – Oppenheimer approximation [1], proposed in 1927, assumes that the motion of the electrons and the motion of nuclei can be treated separately. This assumption significantly simplifies the problem of solving the Schrodinger equation for the molecular system.

2.2.2 The Schrodinger Equation of a Diatomic Molecular System

To describe the diatomic molecular system, let's start from the Schrodinger equation for a diatomic molecule:

$$\hat{H}\Psi_i = E_i\Psi_i \tag{2.1}$$

where $\hat{H}$ is the diatomic molecular Hamiltonian, Ψ_i is the eigenfunction of the molecular state i and E_i is the eigenvalue of the corresponding state. The Hamiltonian for a diatomic molecule can be written as:

$$\begin{aligned} H &= H^N + H^e + V \\ &= H^N + H^e + V^{NN} + V^{Ne} + V^{ee} \end{aligned} \tag{2.2}$$

where H^N and H^e are the nuclear and electronic energy, respectively. Here V stands for the potential energy, and V^{NN}, V^{Ne}, and V^{ee} are the nuclear – nuclear repulsive energy,

the attractive Coulomb interaction energy between the electrons and the nuclei, and the electron – electron repulsive Coulomb interaction energy, respectively. The Hamiltonian for the diatomic molecule can be further written as:

$$H = \sum_{a=1,2} \frac{P_a^2}{2M_a} + \sum_i \frac{P_i^2}{2m} + \frac{Z_1 Z_2 e^2}{4\pi\varepsilon_0 R} - \sum_a \sum_i \frac{Z_a e^2}{4\pi\varepsilon_0 r_{ia}} + \sum_i \sum_{j>i} \frac{e^2}{4\pi\varepsilon_0 r_{ij}} \tag{2.3}$$

The Greek subscripts refer to the nuclei, and the Roman subscripts refer to the electrons. R is the internuclear distance.

Schrodinger equation determines the energy level structure of the diatomic molecules, but it is not easy to solve approximately. References [2-5] present useful approaches for solving it.

To simplify the Schrodinger equation, two coordinate transformations are applied. The first transformation is from a space system which has an arbitrary origin (xyz) to a space coordinate system (XYZ) with the origin at the center mass of the nuclei. In the second transformation the space coordinate system (XYZ) is then transformed into a molecular coordinate system. Both systems share the same origin.

The second transformation can be described by the three Euler angles R, θ and ϕ. In terms of Euler angles, we can express the Hamiltonian in the form:

$$H = H^N(R,\theta,\phi) + H^e(r) + V(r,R) \tag{2.4}$$

As stated earlier, the velocities of the electrons are much bigger than those for the nuclei. In the Born-Oppenheimer approximation, the motions of the electrons and the nuclei can be treated separately. The wavefunction can be written as

$$\Psi_i^{BO} = \varphi_{ie}(r,R)\chi_{v,J}(R,\theta,\phi) \tag{2.5}$$

where $\varphi_{ie}(r,R)$ stands for the electronic wavefunction and $\chi_{v,J}(R,\theta,\phi)$ stands for the vibrational- rotational wavefunction of the nuclei. Here v is the vibrational quantum number and J is rotational quantum number.

The energy of the molecule can be written approximately as the sum of the electronic energy $T_{i,e}$, the vibrational energy G(v) and the rotational energy F(J):

$$E_i = T_{i,e} + G(v) + F(J) \tag{2.6}$$

The time independent Schrodinger equation can be separated into electronic and nuclear wave equations:

$$[H^e(r,R) + V(r,R)]\varphi_{i,e}(r,R) = E_{i,e}(R)\varphi_{i,e}(r,R) \tag{2.7}$$

$$[H^N(R,\theta,\phi) + E_{i,e}(R)]\chi_{v,J}(R,\theta,\phi) = E_N\chi_{v,J}(R,\theta,\phi) \tag{2.8}$$

The potential energy curve $E_{i,e}(R)$ can be obtained by solving the electronic eigenvalue equation for different internuclear distance values R.

2.2.3 Electronic States of Diatomic Molecular

According to the Born- Oppenheimer approximation, the motion of the electrons and the motion of nuclei can be treated separately. As a result, the molecular energy levels can be classified in terms of electronic and nuclear states. The nuclear states include vibrational states and rotational states.

Figure 2.1 illustrates the angular momenta for a diatomic molecule and their projections on the internuclear axis. $\boldsymbol{L}$ is the electronic orbital angular momentum. Neglecting the electron spin, $\boldsymbol{L}$ is not a constant, although the component about the inter-nuclear axis $\boldsymbol{L}_z$ is conserved. In a diatomic molecule the potential in which the electrons move is symmetric about the internuclear axis.

Let Λ represent the absolute value of the projection of the electronic orbital momentum (L) along the internuclear axis. For a given value of the orbital electronic quantum number (L), Λ can take the values

$$\Lambda = 0, 1, 2, \ \ldots, L . \tag{2.9}$$

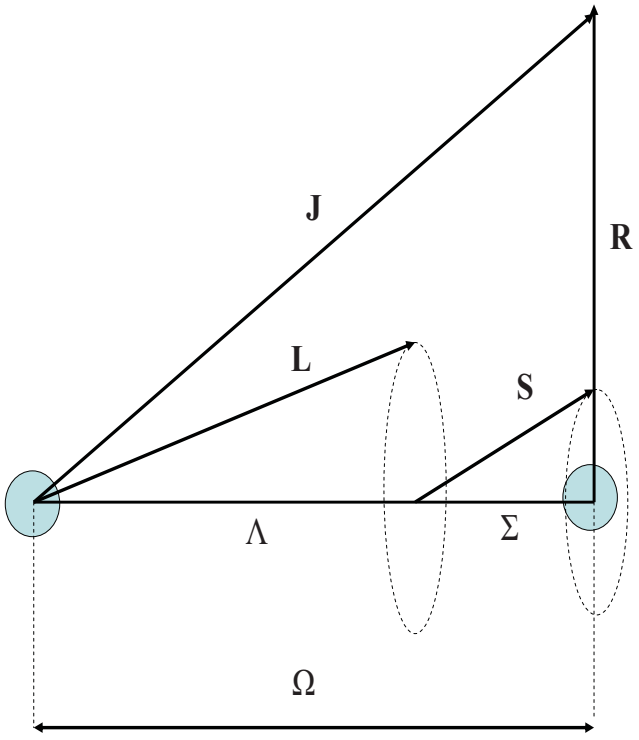

Figure 2.1 Angular momentum and good quantum numbers in a diatomic molecule.

When $\Lambda = 0, 1, 2, 3, \ldots$, the electronic state is accordingly labeled $\Sigma, \Pi, \Delta, \Phi, \ldots$ state. $\Pi, \Delta, \Phi, \ldots$ states are doubly degenerate, while the Σ states are non – degenerate.

Now let's consider the electron spin for diatomic molecules. The spins of the individual electrons form a resultant spin $\boldsymbol{S}$. The electron spin component along the internuclear axis M_S is conserved, and it is denoted by Σ. Σ can have $2S + 1$ different possible values:

$$\Sigma = S, S-1, S-2, \ldots, -S \tag{2.10}$$

In general these $2S+1$ states are non-degenerate.

When we add the electronic angular momentum $\boldsymbol{L}$ and the component of $\boldsymbol{S}$ along the internuclear axis together, the resultant is the total electronic angular momentum about the internuclear axis, which is denoted by $\boldsymbol{\Omega}$:

$$\boldsymbol{\Omega = \Lambda + \Sigma} \tag{2.11}$$

If $\Lambda \neq 0$, for a given value of Λ bigger than S, $\Lambda + \Sigma$ can have $2S+1$ different values with different energies. This is called spin-orbit splitting. However, if $\Lambda = 0$, there is no magnetic field in the direction of the internuclear axis and no energy splitting. The vector **R** in Figure 2.1 represents the quantized rotational angular momentum of the nuclei.

2.2.4 Vibrational States and Rotational States of a Diatomic Molecule

The vibrational and rotational spectra of diatomic molecules are an important area of spectroscopy with many practical applications and is discussed in [2,6] and many other books.

A diatomic molecule is composed of two atoms and can be considered a vibrating rotator. To understand the rovibrational states of the diatomic molecule, let's start from the so-called dumbbell model, which is shown in Figure 2.2. In this model, we assume that the distance between the two atoms is fixed, which means the molecule is considered to be a rigid rotor. This leads to the equation for the rotational energy:

$$E= \frac{1}{2} I\omega^2 \tag{2.12}$$

where ω is the angular velocity of the rotation, and I is the moment of interia of the system about the axis of rotation given by:

$$I = \mu r^2 \tag{2.13}$$

Here m_1 and m_2 are the masses of the first atom and the second atom, respectively, $\mu = \frac{m_1 m_2}{m_1 + m_2}$ is the reduced mass of the molecule and r is the distance between the atoms.

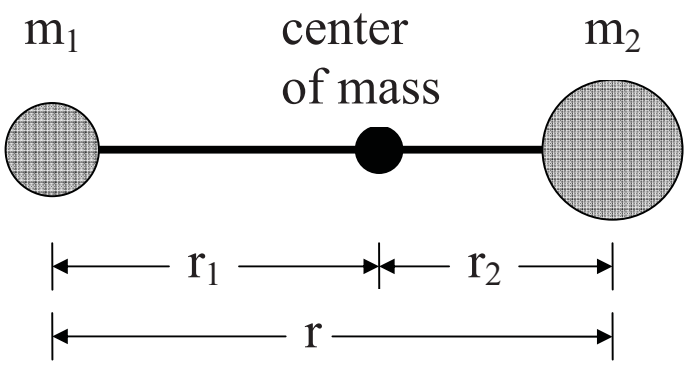

Figure 2.2 Dumbbell model of a diatomic molecule.

We now consider that the diatomic molecule is also vibrating while it is rotating. The Schrodinger equation for this vibrating rotor can be written as:

$$\left[\frac{-\hbar^2}{2\mu}\nabla^2 + V(R)\right]\Psi = E\Psi \,. \tag{2.15}$$

According to Ref [7,8] , the potential energy curve V(R) can be expanded in the form of a polynomial around the equilibrium point $R=R_e$

$$V(R) = a_0(\frac{R-R_e}{R_e})^2[1 + a_1(\frac{R-R_e}{R_e}) + a_2(\frac{R-R_e}{R_e})^2 + \cdots] \tag{2.16}$$

By using the first – order semiclassical quantization condition from Wentzel – Kramers – Brillouin (WKB) theory, Dunham obtained an analytical expression for the energy levels of the vibrating rotor. Experimentally, the Dunham coefficients [8] can be obtained by fitting the term values of the rovibrational levels to the Dunham formula, which can be expressed in the form of a double power series

$$E_{v,J} = \sum_{jk} Y_{jk}(\mathrm{v}+1/2)^j\left[J(J+1) \;-\Lambda^2\right]^k \tag{2.17}$$

where v and J are the vibrational and rotational quantum numbers, respectively, and Λ is the projection of the electronic angular momentum **L** on the internuclear axis.

According to Dunham's formula, there is also a non-vanishing term Y_{00}, which modifies the energy of the vibrational level v = 0. It can be written in terms of the other Dunham's constants as:

$$Y_{00} = \frac{Y_{01}}{4} - \frac{Y_{11}Y_{10}}{12Y_{01}} + \frac{Y_{11}^2 Y_{10}^2}{144Y_{01}^3} + \frac{Y_{20}}{4} \tag{2.18}$$

The customary energy level expressions are:

$$G(\mathrm{v}) = \omega_e(\mathrm{v}+1/2) - \omega_e x_e(\mathrm{v}+1/2)^2 + \omega_e y_e(\mathrm{v}+1/2)^3 \tag{2.19}$$

for the vibrational term values, and

$$F_{\mathrm{v}}(J) = B_{\mathrm{v}}J(J+1) - D_{\mathrm{v}}[J(J+1)]^2 + \ldots \tag{2.20}$$

for the rotational terms in a given vibrational level. Here ω_e is the harmonic vibrational frequency, $\omega_e x_e$ is the vibrational anharmonicity constant, B_{v} is the rotational constant for a given vibrational level, and D_v is the centrifugal distortion constant. D_v is often very small compared to B_v, and as a result the second term can be neglected.

When we compare these two equations with the Dunham expansion, it is clear that Y_{10} is the harmonic oscillator frequency ω_e, Y_{00} is the electronic energy term, also denoted by T_e, and Y_{01} is the rotational constant B_e of a rigid rotator.

If we use Rb_2 as an example, the magnitudes for the electronic energy, vibrational energy and rotational energy are of the order of 10^4, 10^2 and 1 cm^{-1}, respectively. The electronic transitions of the alkali molecules fall into the visible and near – infrared spectral regions, which are within the range of the wavelengths of our tunable frequency stabilized narrow band laser systems.

2.2.5 The RKR Method

The Dunham formula works well in the lower part of the potential well where it is approximately parabolic. It is not accurate at large internuclear distance where the potential curve approaches the dissociation limit. The Rydberg-Klein-Rees (RKR) method [9-12] is widely used to determine diatomic molecular potential energy curves. The RKR method is based on two Klein integrals

$$R_{+}(\mathrm{v}) - R_{-}(\mathrm{v}) = 2\left(\frac{C}{u}\right)^{1/2} \int_{v_{\min}}^{v} \frac{dv'}{\sqrt{G_{\mathrm{v}} - G_{\mathrm{v}'}}} = 2f \tag{2.21}$$

$$\frac{1}{R_{-}(\mathrm{v})} - \frac{1}{R_{+}(\mathrm{v})} = 2\left(\frac{C}{u}\right)^{1/2} \int_{v_{\min}}^{\mathrm{v}} \frac{B_{\mathrm{v}'}dv'}{\sqrt{G_{\mathrm{v}} - G_{\mathrm{v}'}}} = 2g \tag{2.22}$$

where $R_{+}(\mathrm{v})$ and $R_{-}(\mathrm{v})$ are the outer and inner turning points of the potential for vibrational level v with energy term value G (v). B(v) is the inertial rotational constant

for a given vibrational level v, and v_{min} is the minimum vibrational number. Here C is a constant, and μ is the reduced mass.

Calculating the f and g intergrals based on experimental G(v) and B(v) functions, we can write for the inner and outer turning points of molecular vibration:

$$R_{-} = \left[f^2 + \frac{f}{g} \right]^{1/2} - f \tag{2.23}$$

$$R_{+} = \left[f^2 + \frac{f}{g} \right]^{1/2} + f \tag{2.24}$$

This can also be expressed as

$$f \equiv \frac{1}{2}(R_{+} - R_{-}) \qquad \text{and} \qquad g \equiv \frac{1}{2}\left(\frac{1}{R_{-}} - \frac{1}{R_{+}}\right) \tag{2.25}$$

With the RKR potential obtained from the experimental term values in this manner, the rovibrational eigenvalues and wavefunctions calculated numerically from the radial the Schrodinger equation for the diatomic molecule are more accurate than with the Morse potential.

2.3 Hund's Coupling Cases

In analyzing the coupling of the angular momenta of a diatomic molecule, Hund considered several cases, which cover the vast majority of molecules. Understanding these cases is very important for the analysis of experimental spectra.

Hund's case (a): Fig 2.3 (a) is the vector diagram for Hund's case (a). $\boldsymbol{L}$ is the electronic orbital angular momentum, and Λ represents the component of the electronic orbital momentum ($\boldsymbol{L}$) along the internuclear axis. In terms of the quantum value of the electronic orbital quantum number $\boldsymbol{L}$, the quantum number Λ can take the values:

$$\Lambda = 0, 1, 2, \ \dots , L \ . \tag{2.26}$$

When $\Lambda = 0, 1, 2, 3, \ \dots$, the molecular electronic state is denoted by Σ, Π, Δ, Φ, … state. The sum of the individual electron spin angular momenta is designated by $\boldsymbol{S}$. Hund's case (a) assumes that the electronic motion is coupled very strongly to the line joining the nuclei while the interaction of the nuclear rotation with the electronic motion (spin as well as orbital) is very weak. The electronic angular momentum and spin are coupled individually to the internuclear axis. The total electronic angular momentum about the internuclear axis $\boldsymbol{\Omega}$ and the angular momentum $\boldsymbol{R}$ of nuclear rotation form the total angular momentum $\boldsymbol{J}$, which is a constant in magnitude and direction. While $\boldsymbol{\Omega}$ and $\boldsymbol{R}$ rotate about $\boldsymbol{J}$, the $\boldsymbol{L}$ and $\boldsymbol{S}$ process about the internuclear axis has a much higher frequency.

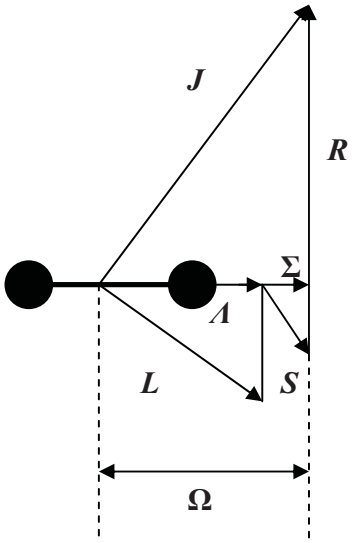

Hund's case (a)

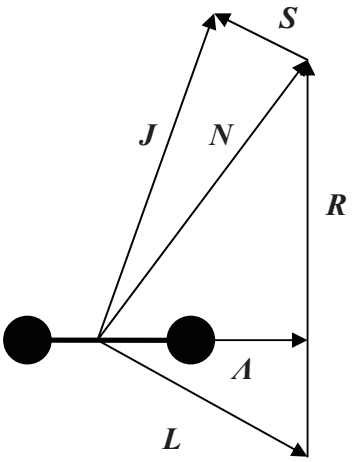

Hund's case (b)

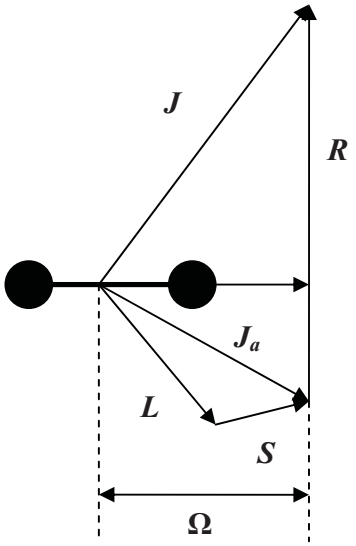

Hund's case (c)

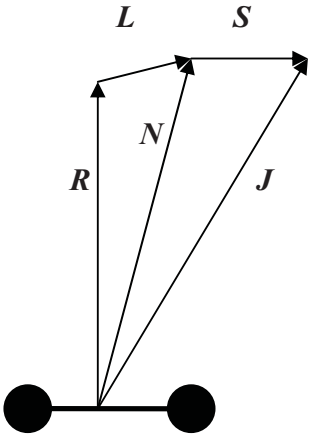

Hund's case (d)

Figure 2.3 Hund's coupling cases.

Hund's case (b): When $\Lambda = 0$ and $S \neq 0$, the spin vector $\boldsymbol{S}$ is not coupled to the internuclear axis at all, and we call this case Hund's case (b). The electronic angular momentum about the internuclear axis $\boldsymbol{\Omega}$ is not defined in Hund's case (b). Even if $\Lambda \neq 0$, unlike what happens in Hund's case (a), for some of the light molecules $\boldsymbol{S}$ may be only very weakly coupled to the internuclear axis. Hund's case (b) applies when the coupling of $\boldsymbol{S}$ to the internuclear axis is zero or weak.

Hund's case (c): In Hund's case (c), the interaction between $\boldsymbol{L}$ and $\boldsymbol{S}$ is stronger than the interaction with the internuclear axis. $\boldsymbol{L}$ and $\boldsymbol{S}$ are coupled together to form a resultant $\boldsymbol{J_a}$, which has component $\boldsymbol{\Omega}$ along the internuclear axis. As in Hund's case (a), $\boldsymbol{\Omega}$ and $\boldsymbol{R}$ form the resultant momentum $\boldsymbol{J}$.

Hund's case (d): Hund's case (d) applies if the coupling between $\boldsymbol{L}$ and the internuclear axis is very weak while that between $\boldsymbol{L}$ and the rotation axis is strong. The angular momentum of nuclear $\boldsymbol{R}$ and $\boldsymbol{L}$ are coupled to form $\boldsymbol{N}$, which is the total angular momentum apart from spin. $\boldsymbol{N}$ and $\boldsymbol{S}$ form the total angular momentum $\boldsymbol{J}$.

2.4 Selections Rules of Transitions between Different Molecular States

External electric or magnetic fields contribute additional terms to the molecular Hamiltonian. As a result of that, two different molecular states can be coupled, and this leads to transitions from one state to another. The transition probabilities and intensities

can be obtained from rovibrational wavefunctions and electronic transition dipole moment functions between different electronic states.

2.4.1 Selection Rules of Rotational Transitions

Let's first look at the selection rules for the rotational quantum number ***J***. Using M_x, M_y and M_z to denote the electric transition dipole moment in the x,y,z directions respectively and $R_x^{J'M'J"M"}$, $R_y^{J'M'J"M"}$ and $R_z^{J'M'J"M"}$ to denote the corresponding matrix elements of the electric transition dipole moment, we consider the matrix elements:

$$R_x^{J'M'J"M"} = \int \psi_r^{J'M'*} M_x \psi_r^{J"M"} d\tau$$

$$R_y^{J'M'J"M"} = \int \psi_r^{J'M'*} M_y \psi_r^{J"M"} d\tau$$

$$R_z^{J'M'J"M"} = \int \psi_r^{J'M'*} M_z \psi_r^{J"M"} d\tau \qquad (2.27)$$

Here $\psi_r^{J'M'}$ and $\psi_r^{J"M"}$ are the eigenfunctions of the higher state and the lower state, respectively. We only consider electric dipole transitions because they are much more probable than electric quadrupole or magnetic dipole transition.

If the matrix element $R^{J'M'J"M"}$ differs from zero, the transition is possible but not when $R^{J'M'J"M"}$ is zero. This leads to selection rules for the rotational transition:

$$\Delta J = J' - J" = \pm 1 \quad \text{for } \Omega = 0$$

$$\Delta J = J' - J" = 0, \pm 1 \quad \text{for } \Omega \neq 0 \qquad (2.28)$$

In a common spectroscopic notation, the molecular transitions with different ΔJ values are defined by:

$$P(J'') \quad \text{when} \quad \Delta J = -1$$
$$Q(J'') \quad \text{when} \quad \Delta J = 0$$
$$R(J'') \quad \text{when} \quad \Delta J = 1 \tag{2.29}$$

2.4.2 Selection Rules of the Vibrational Transitions; the Franck – Condon Principle

The vibrational transitions between different electronic states are governed by the Franck – Condon principle which states: *The electron jump in a molecule takes place so rapidly in comparison to the vibrational motion that immediately afterwards the nuclei still have very nearly the same relative position and velocity as before the jump.* This kind of transition is called a vertical transition.

The intensity of a vibrational transition is proportional to the square of the overlap integral between the vibrational wavefunctions of the two states involved. We call the degree of overlap of the wavefunctions for the initial vibrational state and the final vibrational state the Franck – Condon factors (FCF). The FCF of a rovibronic transition can be expressed as:

$$FCF = \left| \int \psi_{v'}^{J'M'} \psi_{v''}^{J''M''} d\tau \right|^2 \tag{2.30}$$

here $\psi_{v''}^{J''M''}$ and $\psi_{v'}^{J'M'}$ are the wave functions of the two electronic states coupled by the electric dipole transition. In our experiment, we calculated FCFs for the transitions of different vibrational levels by using the LEVEL program developed by LeRoy [13]. The LEVEL program takes the potential curves of the electronic states involved in the transition from the input file and solves the radial Schrodinger equation numerically. It then calculates the FCFs as output. If transition dipole moments are, either experimentally or theoretically, the FCF information can be augmented by calculating the corresponding transition dipole matrix elements.

In choosing the optimal pump laser transition for an experiment, the initial choice is made based on the FCF calculations and available laser wavelength. Knowing the FCFs is also important for predicting and interpreting the signal to noise ratios in the experiments. This is illustrated in this Thesis when we compare the strengths of the Cs_2 and Rb_2 polarization spectroscopy signals. More details about the calculations of the FCFs can be found in Ref. [14].

2.4.3 Electric Dipole Selection Rules of Electronic Transitions

Let's introduce the parity operator $\boldsymbol{E^*}$ which inverts all of the coordinates of the diatomic molecule in the laboratory frame:

$$\begin{aligned} \boldsymbol{E^*}\psi\ (X, Y, Z) &= \psi\ (-X, -Y, -Z) \\ &= \pm\ \psi\ (X, Y, Z) \end{aligned} \tag{2.30}$$

Here $\psi\ (X, Y, Z)$ is the total rovibronic wavefunction of the diatomic molecule. If an electronic state does not change sign under reflection, the electronic state has positive (+) total parity, and if it does change sign under reflection, the state has negative (-) total parity.

For electronic states with $\Lambda \geq 1$, a level that has positive (+) parity is labeled e if $(-1)^J = 1$ and f if $(-1)^J = -1$. For a level with negative (-) parity, the level has e parity if $(-)(-1)^J = -1$ and f parity if $(-1)(-1)^J = 1$. The operator $\hat{\imath}$ is a symmetry operation in which the electrons are inverted through the center of the molecule, meaning that:

$$\hat{\imath}\ \psi_{el}(x_i, y_i, z_i) = \psi_{el}(-x_i, -y_i, -z_i) = \pm\psi_{el}(x_i, y_i, z_i) \tag{2.31}$$

The + sign corresponds to g (gerade) parity and – sign corresponds to *u* (ungerade) parity.

The following selection rules hold for electronic transitions of diatomic molecules:

- $g \leftrightarrow u$ Transitions from g to g state and from u to u state are forbidden.

In our experiment, ungerade intermediate 'window' levels are needed if the purpose is to excite from the ground state (g parity) to higher states which have g parity.

- $e \leftrightarrow f$ when $\Delta J = 0$ and $e \leftrightarrow e,\ f \leftrightarrow f$ when $\Delta J = \pm 1$

- $s \leftrightarrow s,\ a \leftrightarrow a$ This means that symmetric rotational levels can only be coupled with symmetric levels and antisymmetric levels can only be coupled with antisymmetric levels.

- $\Delta\Lambda = 0, \pm 1$, which means that $\Sigma - \Sigma, \Sigma - \Pi, \Pi - \Delta, \ldots$ transitions are allowed while $\Sigma - \Delta$ transitions are forbidden. Only $\Sigma^+ - \Sigma^+$ and $\Sigma^- - \Sigma^-$ are allowed.

- $\Delta S = 0$, which means that transitions are allowed only between states with the same spin multiplicity. Singlet ↔ triplet transitions are forbidden.

2.5 Terms Neglected in the Born - Oppenheimer Approximation

2.5.1 The Spin – Orbit Operator

The interaction between the electron spin and the electron orbital momenta is called the spin – orbit interaction. The spin – orbit Hamiltonian H^{so} for a diatomic molecule can be expressed as:

$$H^{so} = \frac{gsu_B}{c} \sum_i \left[\frac{Z_A e}{r_{iA}^3} [(r_i - r_A) \times \frac{\mathbf{v}_i}{2}] \cdot s_i + \frac{Z_B e}{r_{iB}^3} [(r_i - r_B) \times \frac{\mathbf{v}_i}{2}] \cdot s_i \right]$$
$$- \frac{gsu_B}{c} \sum_{i \neq j} \frac{e}{r_{ij}^3} [(r_i - r_j) \times (\frac{1}{2}\mathbf{v}_i - \mathbf{v}_j)] \cdot \mathbf{s}_i \qquad (2.32)$$

where gs is the Lande electronic factor, u_B is the Bohr magneton which is $\frac{e\hbar}{2mc}$ and $\mathbf{v}_i$ is the velocity of the ith electron measured in the molecule fixed coordinate frame.

To simplify the equation, we can replace $\mathbf{v}_i$ by p_i/m. Here p_i is the momentum of the electron measured in the molecule fixed coordinate frame. The angular momentum operator l_i can be expressed in the form

$$l_{iA} = (1/\hbar)(r_{iA} \times p_i), \qquad l_{iB} = (1/\hbar)(r_{iB} \times p_i)$$

The expression for the spin – orbit Hamiltonian becomes [5] :

$$H^{so} = \frac{a^2}{2} \sum_i \left[\frac{Z_A}{r_{iA}^3} l_{iA} \bullet s_i + \frac{Z_B}{r_{iB}^3} l_{iB} \bullet s_i \right] - \frac{a^2}{2} \sum_{i,j,i \neq j} \frac{1}{r_{ij}^3} (r_{ij} \times p_i)(s_i + 2s_j) \qquad (2.33)$$

Here a is the fine structure constant, $a = \frac{e^2}{\hbar c} = \frac{1}{137.036}$.

This equation includes two parts. The first part is a single – electron operator and it represents the interaction between each of the electrons and the two nuclei Z_A and Z_B. The second part of the equation describes the spin-other-orbit interactions between electrons which can be included in the first term as a screening effect. The spin-orbit Hamiltonian can then be written as:

$$H = \sum_i a_i l_i \cdot s_i \quad \text{with} \quad a_i l_i = \sum_K \frac{a^2}{2} \frac{Z_{eff,K}}{r_{iK}^3} l_{iK} \qquad (2.34)$$

where $Z_{eff,K}$, the effective charge of the K'th nucleus, is less than Z_K and l_{iK} is the orbital angular momentum of the ith electron and the K'th nucleus.

2.5.2 Perturbation Selection Rules

Selection rules for perturbation [2,15] are determined by the quantum numbers and symmetry properties of the two states considered:

(1) $\Delta J = 0$, which means both of the states should have the same total angular momentum.

(2) The spin of the two states can be differ by 0 or ±1, which can be expressed as $\Delta S = 0, \pm 1$.

(3) In Hund's coupling case (a) and (b) where Λ is defined, $\Delta \Lambda = 0, \pm 1$. In Hund's coupling case (c), where Ω is defined instead of Λ, the rule becomes $\Delta \Omega = 0, \pm 1$.

(4) The two energy levels must be both positive or both negative, which means $+ \leftrightarrow +$, $- \leftrightarrow -$, but not $+ \leftrightarrow -$.

(5) Both energy levels must have the same symmetry in the nuclei, which means $s \leftrightarrow s$, $a \leftrightarrow a$, but $s \leftarrow / \rightarrow a$.

The $A^1\Sigma_u^+$ and $b^3\Pi_u$ states of alkali dimers are coupled by the spin – orbit interaction, and they have both singlet and triplet character. Due to the electric dipole selection rule $\Delta S = 0$, the higher lying triplet states of alkali dimers would not be accessible if there were no spin – orbit interaction.

References:

1. Born, M., and Oppenheimer, R., Ann. Phys. **84**, 4571(1927).
2. Herzberg, G., *Molecular Spectra and Molecular Structure*. 2nd ed. Vol. I. Van Nostrand, New York, 1950.
3. Bunker, P. R., and Jensen, P., *Molecular Symmetry and Spectroscopy*, 2nd ed. (NRC Research Press, Ottawa, 1998).
4. Brown, J., and Carrington, A., *Rotational Spectroscopy of Diatomic Molecules*. (Cambridge University Press, 2003).
5. Lefebvre - Brion, H., and Field, R. W., *The Spectra and Dynamics of Diatomic Molecules*, Revised and Enlarged edition ed. (Elsevier Academic Press, 2004).
6. Bernath, P., *Spectra of Atoms and Molecules*. (1995).
7. Hougen, J. T., *The Calculation of Rotational Energy Levels and Rotational Line Intensities In Diatomic Molecules*. (US government Printing Office, NBS Monograph, Washington, D.C., 1970).
8. Dunham, J. L., Phys. Rev. **41**, 721 (1932).
9. Rydberg, R., Physik. **73**, 376 (1931).
10. Rydberg, R., Z. Physik **80**, 514 (1933).
11. Klein, O., Z. Physik **76**, 226 (1932).
12. Rees, A. L. G., Proc. Phys. Soc (London) **59**, 998 (1947).
13. LeRoy, R. J., LEVEL 8.0: A computer program for solving the radial Schrodinger equation for bound and quasibound levels (University of Waterloo Physics Research Report 2007).

14. Joel Tellinghuisen, "The Franck-Condon Principle in Bound-Free Transitions", in in *Photodissociation and Photionization,* edited by Lawley, K. P., (John Wiley&Sons, NEW YORK, 1985), pp. 299-369.

15. Kayama, K., and Baird, J. C., J. Chem. Phys. **46**, 2604 (1967).

CHAPTER 3

THEORETICAL BACKGROUND OF POLARIZATION SPECTROSCOPY

3.1 Introduction to Doppler-free Polarization Spectroscopy

The laser is a powerful tool in molecular spectroscopy. The special characteristics of lasers such as high intensity and extremely small bandwidth have increased the spectral resolution and sensitivity by several orders of magnitude. Lasers have enabled scientists to study the energy level structure of molecules and atoms in much greater detail. In this chapter, we will highlight the use of lasers in polarization spectroscopy.

One of the advantages of single longitudinal mode lasers is that they can be used to overcome limitations caused by the Doppler broadening, since the narrow bandwidth of the tunable laser interacts with a chosen velocity group within the Doppler profile. Doppler broadening is caused by the thermal motion of the absorbing and emitting molecules, and it contributes to the spectral linewidth of gas phase molecules. Doppler broadening reduces the spectral resolution and makes it difficult to assign spectral lines. Reducing the Doppler- broadening increases the resolution so that isotope shifts, hyperfine splitting and Zeeman splitting can be studied.

The techniques of two-photon absorption spectroscopy, saturation spectroscopy, and polarization spectroscopy use single mode lasers and effectively reduce the Doppler broadening [1].

3.1.1 Two-Photon Absorption Spectroscopy

Two-photon absorption spectroscopy was first proposed by Vasilenko *et al*. in1970 [2]. A laser beam is divided into two counter-propagating beams. Assume that the gas phase molecule moves at velocity **v** in the laboratory frame. In the frame of this molecule, the frequencies of the two laser beams are shifted to $\omega_1 = \omega_0 - \mathbf{k}\cdot\mathbf{v}$ and $\omega_2 = \omega_0 + \mathbf{k}\cdot\mathbf{v}$, respectively. Here ω_0 is the frequency of the laser beams in the laboratory frame. When the molecule absorbs photons ω_1 and ω_2, the two photon transition is independent of Doppler broadening, because $\omega_1 + \omega_2 = (\omega_0 - \mathbf{k}\cdot\mathbf{v}) + (\omega_0 + \mathbf{k}\cdot\mathbf{v}) = 2\omega_0$.

3.1.2 Saturation Spectroscopy

Saturation spectroscopy is also called Lamb-dip spectroscopy. In this technique, a strong pump laser beam and a weak probe laser beam are arranged in a counter propagating geometry, and both of them pass through the gas phase sample. When the pump laser beam is strong enough and it is tuned to a transition of the gas phase sample, the transition will be saturated. The weak probe laser can not add more excitation of the $\mathbf{k}\cdot\mathbf{v}$=0 molecules, which makes the signal smaller than the other velocity groups [1]. Thus, a narrow Lamb dip can be observed at the center of the Doppler profile.

3.1.3 Polarization Spectroscopy

In laser spectroscopy spectra are recorded by either the absorption or emission of light. What makes the polarization spectroscopy technique unique is that there is a signal whenever the polarization direction of the probe laser changes. The change of the polarization of the probe laser beam is induced by a much stronger pump beam, which produces an anisotropic distribution of the magnetic sublevels and thus causes orientation of the molecular angular momentum.

3.2 Polarization Spectroscopy

3.2.1 Polarized Light

Light can be polarized if it interacts with matter with asymmetric optical properties in the transverse plane relative to the propagation direction. In our polarization spectroscopy experiments on the Rb_2 and Cs_2 dimers, the pump beam is circularly polarized, and the probe beam is linearly polarized.

3.2.1.1 How to Produce Linearly Polarized Light

There are four general ways that linearly polarized light can be produced: dichroism, birefringence, reflection and scattering.

Dichroism

When light passes through a dichroic polarizer, the component of the **E**-field which oscillates perpendicular to the direction of the transmission axis will be absorbed by the polarizer. The component that has the same vibration direction as the transmission axis is transmitted, so that the transmitted light is linearly polarized.

Birefringence

When light interacts with a birefringent material, there are two different refracted beams due to the two indices of refraction ($n_{\perp}$ and $n_{\parallel}$) of the birefringent material. If the light goes through a crystal which has thickness *d*, the optical path difference between the two refracted beams is:

$$\Delta = \left| n_{\perp} - n_{\parallel} \right| d \tag{3.1}$$

and the corresponding phase difference is:

$$\Delta\varphi = 2\pi\left(\frac{\Delta}{\lambda_0}\right) = \left(\frac{2\pi}{\lambda_0}\right) \left| n_{\perp} - n_{\parallel} \right| d \tag{3.2}$$

where λ_0 is the wavelength of the light in vacuum. From equation (3.2) we note that for a certain wavelength λ_0, $\Delta\varphi$ is proportional to the thickness *d* of the birefringent material. There are retardation plates in which the thickness d of the birefringent material can be adjusted continuously. This kind of device is called a compensator. We used a Babinet-Soleil compensator from Karl Lambrecht Inc., Chicago, in our polarization spectroscopy experiments to convert the linearly polarized pump laser beam into a circularly polarized beam.

Reflection

When light travels from one dielectric material (n_1) to another dielectric material (n_2) is incident at Brewster's angle

$$\theta = \tan^{-1}(\frac{n_2}{n_1}), \tag{3.3}$$

The reflected and refracted rays are perpendicular and the reflected ray is linearly polarized.

Scattering

When unpolarized light interacts with the molecules inside the scattering material, radiation will be re-emitted in all directions. When viewed from a direction perpendicular to the incoming light direction, the scattered light is partially polarized. An example of this is the partial polarization of scattered sunlight, which can be seen by looking at the sky through a polarizing filter while it is rotated. Because polarization by scattering is weak and far from perfect, we do not use this method to produce polarized light in our experiment.

3.2.1.2 How to Produce Circularly Polarized Light

Linear polarizers and a λ/4 circular polarizer were used in our polarization spectroscopy experiment. The linear polarizer is a Glan Thompson polarizer. The λ/4 circular polarizer is a Babinet-Soleil compensator from Karl Lambrecht, Inc.

Babinet-Soleil Compensator

As explained above, the Babinet Soleil compensator is an optical device made from a birefringent material with continuously adjustable thickness. One of the wedges is attached to the parallel plate while the other one is attached to a micrometer. The micrometer can be adjusted to vary the thickness of the wedges with a least count of 0.01mm. An optional rotatable mount (KLC Model DCGF) is used for easy and accurate adjustment of the compensator azimuth with an accuracy of less than one arc minute. A dovetail slide permits the compensator to be easily removed from the path of the light beam.

In our polarization spectroscopy experiment, we tuned the thickness of the Babinet-Soleil compensator so that $\Delta\varphi = \pi / 2$ for the pump beam. Thus we also call our Babinet-Soleil compensator the λ/4 plate. The circularly polarized pump beam is produced in two stages. First the laser beam passes through a linear polarizer in front of the Babinet - Soleil compensator to eliminate any ellipticity in its polarization. Second, the λ/4 plate is adjusted to form a 45 degree angle relative to the transmission axis of the linear polarizer, and circularly polarized light can be produced at any wavelength within the tuning range of the laser by adjusting the Babinet-Soleil compensator for the wavelength the laser.

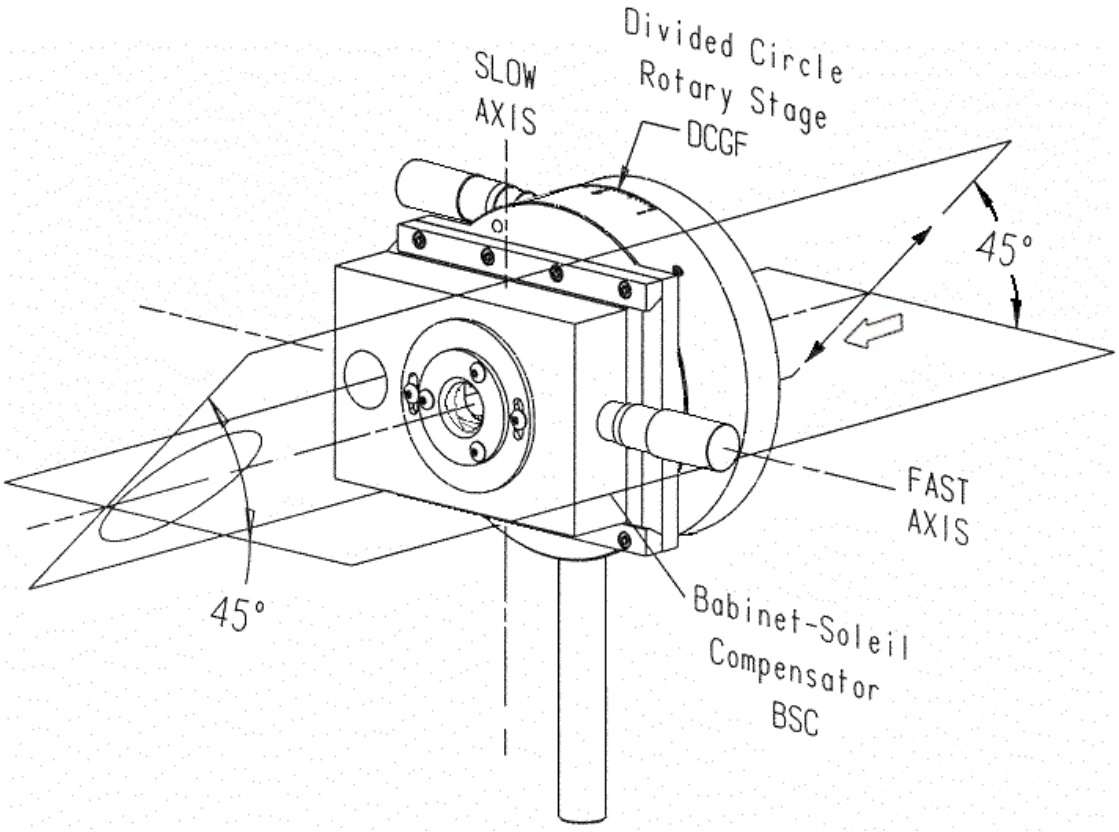

Figure 3.1 The Babinet-Soleil compensator that was used in our polarization experiments to produce circularly polarized laser beam.

To confirm that the pump beam is circularly polarized, we mounted a linear polarizer and a power meter after the λ/4 Babinet Soleil compensator. The power of the circularly polarized beam should be distributed equally in every direction that is perpendicular to its propagation axis. Thus the reading of the power meter should not change much during the rotation of the linear polarizer used as an analyzer.

3.2.2 Basic Principle of Polarization Spectroscopy

The basic principles of the polarization spectroscopy technique are discussed clearly in reference [1].

Laser polarization spectroscopy is based on the selection rule of the magnetic sublevel M which is the projection of the total angular momentum quantum number J onto the direction of the light propagation. M'' denotes the quantum number M of the ground state , and M' denotes the quantum number M of the upper state. If a transition is pumped by circularly polarized light, the change of M follows the selection rule $\Delta M = \pm 1$ (- for clockwise circularly polarized laser beam and + for counter clockwise circularly polarized laser beam)

When the pump laser beam is tuned to the $(J', M') \leftarrow (J'', M'')$ transition and the power is strong enough, the degenerate M sublevels of the rotational level J'' will be partially or completely depleted due to saturation. But when the pump beam is circularly polarized, some M sublevels will be unaffected. We can see this in Figure 3.2. The upper part of the

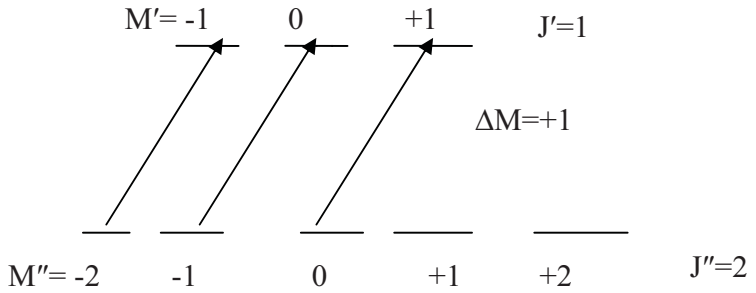

(a)

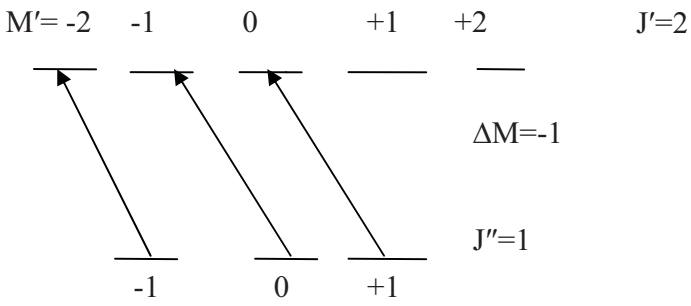

(b)

Figure 3.2 Polarization spectroscopy (a) level scheme for a P transition (b) level scheme for an R transition.

figure shows that for J''=2, when the transitions are P (ΔJ = -1) transitions, the total angular momentum quantum number of the upper level is J' = 1. The M sublevels M'' = 1 and M'' = 2 will remain unaffected when ΔM = 1. The lower portion of Figure 3.2 shows that for R (ΔJ = +1) transitions, the M sublevels M' = 1 and M' = 2 are not populated. Thus the population of the M sublevels is anisotropic.

In our polarization spectroscopy experiments, we install a linear polarizer before the heat pipe oven with its transmission axis in the same direction as the polarization direction of the linearly polarized probe laser beam. The counterpropagating linearly polarized probe laser beam can be considered to be made up of equal parts left- and right-circular polarization. When the probe frequency is tuned to a transition sharing either the upper or the lower level in the excitation, the orientation created by the pump causes the two circularly polarized probe components to experience different absorption coefficients (circular dichroism) and different indices of refraction (circular birefringence). Consequently, when the probe beam exits the oven, the two components no longer sum to the initial linear polarization. Instead the beam has a slight elliptical polarization and some fraction of it is transmitted through a final crossed linear polarizer before reaching the detector.

3.2.3 Different Types of Polarization Spectroscopy

There are three basic kinds of polarization spectroscopy:

1. When spectroscopic analysis and the assignment of vibrational and rotational quantum numbers is not expected to be too difficult, a single laser beam can be split into strong pump beam (75%) and weak probe beam (25%) with no labeling [3]. By labeling we mean that the quantum numbers of the terminal levels of a separate pump beam transition are well known and the probe laser excitations originate from one of these levels, leading to automatic assignment of the probe transitions. If a single laser, that is tuned, is split into two components, all transitions within the tuning range of the laser can be excited and will have to be separately assigned. The two beams are in a counterpropagating geometry and overlap at the center of the heat pipe oven in the region of the sample molecule vapor. The pump beam is circularly polarized and two crossed linear polarizers are installed in the path of the probe beam. The laser frequency is continuously scanned. The circularly polarized pump beam will generate an anisotropic magnetic sublevel distribution in the lower and upper rotational levels involved in the pump laser transitions. The linearly polarized probe laser beam becomes slightly elliptically polarized because the left and right circularly polarized components that the linear polarization consists of are absorbed by different amounts. Thus part of the probe beam passes through the second linear polarizer and is detected by the PMT detector. A simple sketch of this experimental set-up is shown in Fig. 3.3. The assignments of the polarization signals are based on relatively good initial molecular constants. In the particular case of reference [3] additional polarization spectroscopic signals were used in the global deperturbation analysis. The advantage of this type of polarization spectroscopy is that all possible rovibrational transitions are observed with high resolution, and the observed transitions are not limited by the labeling of the pump transition provided that we know the

vibrational and rotational constants well enough to identify the transitions. This technique was first applied to study the hyperfine structure in the hydrogen atom Balmer-β transition [4], and it has been widely used in molecular spectroscopy [5-8] .

2. Optical – optical double resonance polarization spectroscopy [9-11] is preferred when the spectral peaks are hard to assign. The difference between this technique and the one we discussed above is that two different laser beams are used. A strong circularly polarized pump laser pumps a certain well known transition from ground state X (v″, *J*″) to an excited state, while the much weaker probe laser is scanning. From the selection rules, the main lines that can be observed are the probe transitions with $J'=J''\pm 1$.

3. Satellite lines with weaker intensities than the main lines can sometimes be observed because the orientation of the anisotropic field can partially survive the collision – induced transfer [12-21]. The collision - induced lines enlarge the range of rotational lines that can be identified in the experiment. More details about this kind of polarization spectroscopy will be given in the later chapters.

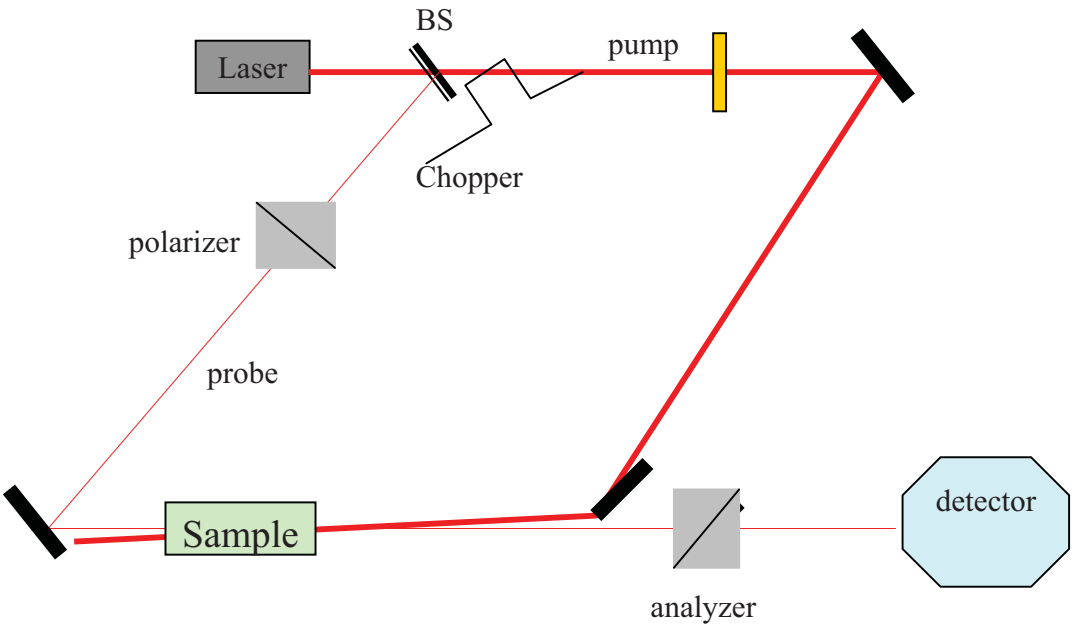

Figure 3.3 The scheme of one laser polarization spectroscopy setup.

3.2.4 Line Profiles of Polarization Signals

The linearly polarized probe wave can be expressed as [1], [22]:

$$\boldsymbol{E} = \boldsymbol{E}_0 e^{i(\omega t - kz)} \quad , \quad \boldsymbol{E}_0 = \{E_{0x}, 0, 0\},$$

Because the linearly polarized beam can be considered to be composed of two circularly polarized components, we can rewrite this electric field as:

$$E^{+} = \frac{1}{2} E_0 (\boldsymbol{x} + i\boldsymbol{y}) e^{-i\omega t}$$

$$E^{-} = \frac{1}{2} E_0 (\boldsymbol{x} - i\boldsymbol{y}) e^{-i\omega t} \tag{3.5}$$

The two components of the linearly polarized beam experience different refractive indices $n_v^{\pm} = \mathrm{Re}[n_v^{\pm}] + i\,\mathrm{Im}[n_v^{\pm}]$ when they propagate through the vapor with length *L* and $n_\omega^{\pm} = \mathrm{Re}[n_\omega^{\pm}] + i\,\mathrm{Im}[n_\omega^{\pm}]$ when they propagate through the two windows with thickness d. Here the real part of the index of refraction represents the dispersion and the imaginary part represents the absorption. After propagating through the vapor and the two windows, the

electric field of the laser can be expressed as:

$$E^{+} = \frac{1}{2} E_0 (\boldsymbol{x} + i\boldsymbol{y}) \exp\left\{ i\left(\frac{2d\omega}{c}\mathrm{Re}[n_\omega^{+}] + \frac{L\omega}{c}\mathrm{Re}[n_v^{+}] - \omega t\right)\right\} \exp\left\{ -\left(\frac{2d\omega}{c}\mathrm{Im}[n_\omega^{+}] + \frac{L\omega}{c}\mathrm{Im}[n_v^{+}]\right)\right\}$$

$$E^- = \frac{1}{2}E_0(\boldsymbol{x} - i\boldsymbol{y})\exp\left\{i(\frac{2d\omega}{c}\mathrm{Re}[n_\omega^-] + \frac{L\omega}{c}\mathrm{Re}[n_v^-] - \omega t)\right\}\exp\left\{-(\frac{2d\omega}{c}\mathrm{Im}[n_\omega^-] + \frac{L\omega}{c}\mathrm{Im}[n_v^-])\right\}$$

(3.6)

They can be simplified to

$$E^+ = \frac{1}{2}E_0(\boldsymbol{x} + i\boldsymbol{y})\exp\{i(b^+ + n^+ - \omega t)\}\exp\{-(\beta^+ + \alpha^+)\}$$

$$E^- = \frac{1}{2}E_0(\boldsymbol{x} - i\boldsymbol{y})\exp\{i(b^- + n^- - \omega t)\}\exp\{-(\beta^- + \alpha^-)\} \qquad (3.7)$$

if we use

$$b^\pm = \frac{2d\omega}{c}\mathrm{Re}[n_\omega^\pm] \qquad \beta^\pm = \frac{2d\omega}{c}\mathrm{Im}[n_\omega^\pm]$$

$$n^\pm = \frac{L\omega}{c}\mathrm{Re}[n_v^\pm] \qquad \alpha^\pm = \frac{L\omega}{c}\mathrm{Im}[n_v^\pm].$$

Let's define

$$b = \frac{b^+ + b^-}{2}, \qquad \Delta b = \frac{b^+ - b^-}{2}, \qquad b^+ = b + \Delta b, \quad b^- = b - \Delta b;$$

$$\alpha = \frac{\alpha^+ + \alpha^-}{2}, \qquad \Delta\alpha = \frac{\alpha^+ - \alpha^-}{2}, \quad \alpha^+ = \alpha + \Delta\alpha, \quad \alpha^- = \alpha - \Delta\alpha;$$

$$\beta = \frac{\beta^+ + \beta^-}{2}, \qquad \Delta\beta = \frac{\beta^+ - \beta^-}{2}, \quad \beta^+ = \beta + \Delta\beta, \quad \beta^- = \beta - \Delta\beta;$$

$$n = \frac{n^+ + n^-}{2}, \qquad \Delta n = \frac{n^+ - n^-}{2}, \quad n^+ = n + \Delta n, \quad n^- = n - \Delta n$$

and substituting them to (3.7), we can get:

$$E^+ = \frac{1}{2}E_0(\boldsymbol{x} + i\boldsymbol{y})\exp\{i(b + n - \omega t)\}\exp\{-(\beta + \alpha)\}\exp\{i(\Delta b + \Delta n)\}\exp\{-(\Delta\alpha + \Delta\beta)\}$$

$$E^{-} = \frac{1}{2} E_0 (x - iy) \exp\{i(b + n - \omega t)\} \exp\{-(\beta + \alpha)\} \exp\{-i(\Delta b + \Delta n)\} \exp\{(\Delta\alpha + \Delta\beta)\}$$

When the beam passes through the second polarizer oriented at an angle θ from the axis perpendicular to the direction of the original polarization, the transmitted electric field can be written as:

$$E_t = \frac{E_0}{2} e^{i(b+n+\omega t)} e^{-(\beta+\alpha)} \{\sin\theta e^{i(\Delta b+\Delta n)} e^{-(\Delta\beta+\Delta\alpha)} + \sin\theta e^{-i(\Delta b+\Delta n)} e^{(\Delta\beta+\Delta\alpha)} + i\cos\theta e^{i(\Delta b+\Delta n)} e^{-(\Delta\beta+\Delta\alpha)} - i\cos\theta e^{-i(\Delta b+\Delta n)} e^{(\Delta\beta+\Delta\alpha)}\}$$

$$= \frac{E_0}{2} e^{i(b+n+\omega t)} e^{-(\beta+\alpha)} \{ie^{-i(\Delta b+\Delta n-\theta)} e^{(\Delta\beta+\Delta\alpha)} - ie^{i(\Delta b+\Delta n-\theta)} e^{-(\Delta\beta+\Delta\alpha)}\} \quad (3.8)$$

The transmitted intensity $I_t(\omega) = c\varepsilon_0 E_t E_t^*$ can be written as:

$$I_t(\omega) = c\varepsilon_0 E_t E_t^*$$

$$= c\varepsilon_0 \frac{E_0^{\,2}}{4} e^{-2(\beta+\alpha)} \{e^{2(\Delta\beta+\Delta\alpha)} + e^{-2(\Delta\beta+\Delta\alpha)} - e^{2i(\Delta b+\Delta n-\theta)} - e^{-2i(\Delta b+\Delta n-\theta)}\} \quad (3.9)$$

$$= c\varepsilon_0 \frac{E_0^{\,2}}{4} e^{-2(\beta+\alpha)} \{\cosh(2\Delta\beta + 2\Delta\alpha) - \cos(2\Delta n + 2b - 2\theta)\}$$

We can define $\theta' = \Delta b - \theta$, $I_0 = c\varepsilon_0 E_0^{\,2}$, the equation will become:

$$I = \frac{I_0}{2} e^{-2(\beta+\alpha)} \{\cosh(2\Delta\beta)\cosh(2\Delta\alpha) + \sinh(2\Delta\beta)\sinh(2\Delta\alpha) - \cos(2\Delta n)\cos(2\theta') + \sin(2\Delta n)\sin(2\theta')\} \quad (3.10)$$

Because the crossing angle, the amount of absorption and the birefringence is small, we can assume that:

$$\sin x \approx x, \sinh x \approx x, \cos x \approx 1 - \frac{x^2}{2} \text{ and } \cosh x \approx 1 + \frac{x^2}{2}$$

Using these expansions and neglect terms in fourth order of small quantities, we can get

$$I = I_0 e^{-2(\beta+\alpha)} \{\Delta\beta^2 + \Delta\alpha^2 + 2\Delta\beta\Delta\alpha + \Delta n^2 + (\theta')^2 + 2\Delta n\theta'\} \tag{3.11}$$

We define $\frac{I}{I_0} = \xi$ as the transmission rate when the two linear polarizers are polarized:

$$I = I_0 e^{-2(\beta+\alpha)} \{\xi + \Delta\beta^2 + \Delta\alpha^2 + 2\Delta\beta\Delta\alpha + \Delta n^2 + (\theta')^2 + 2\Delta n\theta'\} \tag{3.12}$$

Because the absorption coefficient $a(\omega)$ and the refractive index $n(\omega)$ are related by the Kramers – Kronig dispersion relation, we can write $n(\omega)$ in terms of the line-center dichroism Δa_0:

$$\Delta a(\omega) = \frac{\Delta a_0}{1+x^2} \ , \ x = \frac{\omega_0 - \omega}{\gamma_s / 2} \ , \quad \Delta n(\omega) = \frac{\Delta a_0 x}{1+x^2} \tag{3.13}$$

Using equation (3.12) and (3.13), the line profile of the polarization signal can be written as:

$$\begin{aligned} I \ &= I_0 e^{-2(\beta+\alpha)} [\xi + \theta'^2 + (\Delta\beta)^2 + 2\Delta\beta \frac{\Delta\alpha_0}{1+x^2} \\ &+ 2\theta' \frac{\Delta\alpha_0 x}{1+x^2} + (\frac{\Delta\alpha_0}{1+x^2})^2 + (\frac{\Delta a_0 x}{1+x^2})^2] \end{aligned} \tag{3.14}$$

The first three terms are the constant background which is independent of the laser frequency. The fourth term is the Lorentzian part and the fifth term describes the dispersion. The last two terms are squares of small values and they can be neglected.

From this equation we can see that if $\theta' = 0$, the dispersion term will vanish and only the background terms and the Lorentzian terms will be left. In our experiment, we use a power meter (Coherent LabMax TO) with a sensitive detector (LM-2) after the second polarizer, when the heatpipe is cold, and the pump laser is off, to make fine adjustments of the orientation of the second polarizer. At this time, θ' will be decreased to zero if we minimize the reading of the power meter by adjusting the second polarizer. Another way to cancel the dispersion term is to scan the polarization signal directly. By looking at the shape of the polarization signal we can tell if the dispersion term is canceled. Here it should be noted that the PMT can be damaged if too much of the probe laser beam is transmitted through second polarizer during the adjustment.

3.2.5 Conclusion: Advantages of Polarization Spectroscopy

For heavier molecules like Rb_2 and Cs_2, the density of rovibronic energy levels is very high in any electronic state leading to spectra that are hard to identify. With the tunable narrow bandwidth single longitudinal mode lasers, these advantages of the polarization spectroscopic technique are widely recognized. They are summarized below:

1. We achieve high spectroscopic resolution by using the polarization spectroscopic technique. Doppler broadening is one of the main factors that limit the resolution of spectra. The spectra generated by the polarization spectroscopic technique are Doppler free because only the molecules with zero velocity in the laser propagation direction can absorb photons from counter-propagating pump and probe laser beams. With the removal of Doppler broadening, the resolution of the spectra is increased. The linewidth of the polarization signal we obtained in our experiments is from 150 MHz to 250 MHz instead of around 1 GHz. The Doppler broadening varies with temperature, scanning range, buffer gas pressure and the type of sample molecule. Low argon gas pressure also contributes to the high resolution of our spectra. In our experiments the argon pressure was 1 to 3 Torr for Rb_2 and Cs_2.

2. The signal to noise ratio is high which leads to high sensitivity since the probe laser transmission signal is observed with nearly zero background. The polarization characteristics of the probe laser change when the linear polarized probe laser excites a transition that shares the same ground state as the pump transition. The small amount of resulting elliptic polarization of the probe laser is transmitted through the crossed polarizer and detected by a PMT against nearly zero background. Thus the spectral resolution is very high.

3. The high resolution and high sensitivity polarization of spectroscopic technique make the accurate assignment of the spectra possible. The spectra of Rb_2 and Cs_2 dimers are complicated because many energy levels of the Rb_2 and Cs_2 are highly perturbed and the density of rovibrational levels is high. However, the survival of molecular orientation in

collisions can be used to extend the automatic parent (*R,P*) line assignments to the collisional components, which mitigates the assignment problems to a large degree and enhances the yield of the experiment a great deal. More than 2000 distinct spectral lines were resolved in our Rb_2 polarization experiment and 881 of them were identified [21]. More than 300 spectral lines were identified in our Cs_2 polarization experiment. Additional identificatons are in progress using fluorescence decay to the ground state, leading to additional probe signal assignments [20].

References:

1. Demtroder, W., *Laser Spectroscopy, Basic Concepts and Instrumentation*, Second Enlarged ed. (Springer-Verlag, Berlin, 1996).
2. Vasilenko, L. S., Chebotayev, V. P., and Shishaev, A. V., JEPT Lett. **12** (1970).
3. Qi, P., Bai, J., Ahmed, E. H., Lyyra, A. M., Kotochigova, S., Ross, A. J., Effantin, C., Zalicki, P., Vigue, J., Chawla, G., Field, R. W., Whang, T. J., Stwalley, W. C., Knockel, H., Tiemann, E., Shang, J., Li, L., and Bergeman, T., J. Chem. Phys. **127**, 044301 (2007).
4. Wieman, C. and Hansch, T. W., Phys. Rev. Lett. **36**, 1170 (1976).
5. Stert, V. and Fischer, R., Appl. Phys. **17**, 151 (1978).
6. Wang, X., Magnes, J., Lyyra, A. M., Ross, A. J., Martin, F., Dove, P. M., and Roy, R. J. L., J. Chem. Phys. **117**, 9339 (2002).
7. Nishimiya, N., Yasuda, Y., Yukiya, T., and Suzuki, M., J. Mol. Spectrosc. **255**, 194 (2009).
8. Raab, M., Honing, G., Demtroder, W., and Vidal, C. R., J. Chem. Phys. **76**, 4370 (1982).
9. Wickenmeier, W., Diemer, U., Wahl, M., Raab, M., Demtroder, W., and Muller, W., J. Chem. Phys. **82**, 5354 (1985).
10. Lyyra, A. M., Luh, W. T., Li, L., Wang, H., and Stwalley, W. C., J. Chem. Phys. **92**, 43 (1990).
11. Kasahara, S., Hasui, Y., Otsuka, K., Baba, M., Demtroder, W., and Kato, H., J. Chem. Phys. **106**, 4869 (1997).
12. Teets, R., Feinberg, R., Hansch, T. W., and Schawlow, A. L., Phys. Rev. Lett. **37** (11), 683 (1976).

13. Ottinger, C. and Schroder, M., J.Phys.B **13**, 4163 (1980).

14. Diemer, U., Duchowicz, R., Ertel, M., Mehdizadeh, E., and Demtroder, W., Chem. Phys. Lett. **164**, 419 (1989).

15. Kasahara, S., Baba, M., and Kato, H., J. Chem. Phys. **94**, 7713 (1991).

16. Kato, H., Kobayashi, T., Chosa, M., Nakahori, T., Lida, T., Kasahara, S., and Baba, M., J. Chem. Phys. **94**, 2600 (1991).

17. Kasahara, S., Fujifara, C., Okada, N., Kato, H., and Baba, M., J. Chem. Phys. **111**, 8857 (1999).

18. Antonova, S., Urbanski, K., Lyyra, A. M., Spano, F. C., and Li, L., Chem. Phys. Lett. **267**, 158 (1997).

19. Bai, J., Ahmed, E. H., Beser, B., Guan, Y., Kotochigova, S., Lyyra, A. M., Ashman, S., Wolfe, C. M., Huennekens, J., Xie, F., Li, D., Li, L., Tamanis, M., Ferber, R., Drozdova, A., Pazyuk, E. A., Stolyarov, A. V., Danzl, J. G., Nagerl, H. C., Bouloufa, N., Duleiu, O., Amiot, C., Salami, H., and Bergeman, T., Phys. Rev. A **83**, 032514 (2011).

20. Okada, N., Kasahara, S., Ebi, T., Baba, M., and Kato, H., J. Chem. Phys. **105**, 3458 (1996).

21. Salami, H., Bergeman, T., Beser, B., Bai, J., Ahmed, E. H., Kotochigova, S., Lyyra, A. M., Huennekens, J., Lisdat, C., Stolyarov, A. V., Dulieu, O., Crozet, P., and Ross, A. J., Phys. Rev. A **80**, 022515 (2009).

22. Wolfe, C., Ph.D. Thesis, Lehigh University, 2010.

CHAPTER 4

EXPERIMENT

4.1 Introduction

It is well known that an alkali atom with Z electrons can be treated theoretically as a core consisting of the nucleus and Z-1 electrons, with one valence electron moving around them. Therefore, each alkali dimer molecule has only two valence electrons. The simplicity of the electronic structure is one of the reasons that alkali molecules have been studied extensively during the last century. With the recent development of ultra – cold atomic trapping techniques and the progress on Bose Einstein condensates [1,3,5], the interest in the study of diatomic alkali dimer molecules has increased again.

4.2 The Description of the Equipment Used in the Experiments

4.2.1 Lasers

A laser is an optical oscillator that emits light in a narrow, intense, low divergence monochromatic beam with a well defined wavelength. The laser was first invented in the

1960s and it has been used widely in scientific research, in medical applications, industry and military since then. The word *laser* stands for Light Amplification by the Stimulated Emission of Radiation.

There are three essential elements for each laser: the pump, the laser medium and the resonator. There are many kinds of lasers, including gas lasers, dye lasers, metal vapor lasers, solid state lasers and semiconductor lasers.

Dye Laser and TiSapphire Laser

In our the polarization spectroscopy set-up, a tunable single longitudinal mode (Coherent model 699 -29) ring dye laser was used as a pump laser, and a tunable single mode (Coherent model 899 – 29) TiSapphire laser served as the probe laser in both the Rb_2 and Cs_2 experiments. Each of them is equipped with an internal Coherent Autoscan wavemeter, which is used to measure the frequency of the output laser beam with the same computer control used to scan the laser. Each of the two lasers were pumped by a Coherent Verdi V10 solid state laser, which produces a laser beam at 532 nm wavelength with 10W maximum output power.

An infrared sensor card (Model F- IRC1) from Newport helped to trace the invisible infrared TiSapphire laser beam. More details of the dye laser and TiSapphire laser can be found in their laser manuals.

In order to create an optimal overlap region for the pump and probe lasers in the polarization experiment, we attached a razor blade to a translation stage and used this home made assembly to measure the beam waist w of the laser beams. We recorded the readings d_{75} and d_{25} of the micrometer screws when 75 percent and 25 percent of the laser beam passed through the razor blade. The beam waist w was calculated using the equation

$$w = 1.49(d_{75}-d_{25})$$

This method works if the laser beam has a Gaussian TEM0,0 profile, which can be verified using the method by Skinner and Whitcher [17].

4.2.2 Heatpipe Oven

The Rb and Cs metals were loaded at the center of a five-arm heatpipe oven in our polarization spectroscopy experiments. The heatpipe oven technique was first introduced by Vidal and Cooper [18] in 1969.

The pressure of the argon buffer gas inside the heatpipe oven was 1 to 3 Torr and at the end of each heatpipe oven arm there is a glass window which is sealed by a rubber O-ring. The Cs or Rb metal inside the heatpipe oven formed a vapor when the arms and the center of the heatpipe oven were heated by the Lindberg Model 50101 heaters. The region close to the heatpipe windows was cooled by water running through cooling coils on the outside of the heatpipe. The metal vapor diffused from the center of the heatpipe

oven and condensed in the cooler region. The condensed vapor then returned to the center of the heatpipe oven through capillary action created by several layers of stainless steel mesh loaded in each arm. Besides protecting the windows from being coated with metal, this design of the heatpipe oven makes the continuous evaporation and condensation of the metal vapor possible.

The heatpipe oven can operate in either the "heatpipe" mode or the "oven" mode. The argon gas is excluded from the center part of the heatpipe oven when the metal vapor pressure is equal to the argon vapor pressure. This condition is called the "heatpipe" mode. In the "oven" mode, the pressure of the metal vapor is less than the pressure of the argon gas, and the two kinds of vapors mix with each other at the center of the heatpipe oven.

We used a thermal probe to estimate the temperature of the metal vapor inside the heatpipe oven. More precise temperature can be obtained by measuring the full width at half maximum (FWHM) of the Doppler broadened pump laser induced fluorescence profile of the alkali metal dimer molecule. The expression for the temperature is

$$T = \frac{(\frac{\Delta\omega c}{2\omega_0})^2 m_0}{2(\ln 2)k} \qquad (4.1)$$

where $\Delta\omega$ is the FWHM value of the pump laser LIF profile in GHz, ω_0 is the laser frequency at the peak of this profile in the unit of GHz, c is the speed of light, m_0 is the mass of the dimer molecule in kg, and k=1.38*10^{-23} J/k is the Boltzmann constant. It is

important that the laser power has to be kept low enough in the Doppler profile scan to avoid saturation broadening, which would lead to an erroneous temperature reading.

4.2.3 Photomultiplier Tube Detector (PMT)

Photomultipliers (PMT) were used in our lab for detecting fluorescence or polarization signals. The wavelength response of the PMT depends on the model. The PMT is based on the photoelectric effect. We apply a high voltage to the PMT cathode usually from -300V to -800V according to the intensity of the signal we were detecting. The anode was kept at ground voltage. The photoelectrons emitted from the cathode were accelerated towards the anode through a dynode chain, each releasing additional electrons resulting in a current at the anode. The number of photoelectrons is multiplied at each subsequent dynode. We used a Hamamatsu a R928 in the Rb_2 experiment. Its operational range is from 185 nm to 900 nm, with peak sensitivity at 400 nm. To reduce thermal noise, the photomultiplier tube used for detecting resolved fluorescence was the SPEX 1404, which was cooled by a Products for Research (model number TE177RF005) cooling system. This was important for detecting weak signals in the photon counting mode.

4.2.4 BOMEM DA8 FTIR

FTIR stands for Fourier transform Infrared spectroscopy. Before introducing the Bomem DA8 FTIR interferometer, let us consider the concept of the Fourier transform. The Fourier transform of a function *f (x)* can be defined by:

$$F(\sigma) = \int_{-\infty}^{\infty} f(x) e^{-i2\pi\sigma x} dx \tag{4.2}$$

the inverse transformation *f(x)* can be reconstructed by:

$$f(x) = \int_{-\infty}^{\infty} F(\sigma) e^{i2\pi\sigma x} d\sigma \tag{4.3}$$

Using the Euler formula $e^{ix} = cos\, x + i\, sin\, x$, the Fourier transform can be separated into real and imaginary components:

$$\begin{aligned} \mathrm{Re}[F(\sigma)] &= \int_{-\infty}^{\infty} f(x) \cos(2\pi\sigma x) dx \\ \mathrm{Im}[F(\sigma)] &= \int_{-\infty}^{\infty} f(x) \sin(2\pi\sigma x) dx \end{aligned} \tag{4.4}$$

In spectroscopy the Fourier transform relates the time domain and the frequency domain.

The Bomem DA8 FTIR is basically a Michelson interferometer. Michelson first used such a device with Morley to demonstrate that the ether did not exist **[12].** Figure 4.1 is a simple sketch of the Michelson interferometer. It is composed of a beam splitter, a compensator, a fixed mirror and a moving mirror. The input beam is directed onto a beam splitter. One beam travels to a fixed mirror and the other beam travels to a moving mirror which is driven by a motor. The two reflected beams recombine at the beam splitter. The path difference of the two beams varies as the movable mirror moves continuously and the two beams interfere with each other constructively and destructively. A compensator is placed in one arm to make sure that the initial path difference is zero.

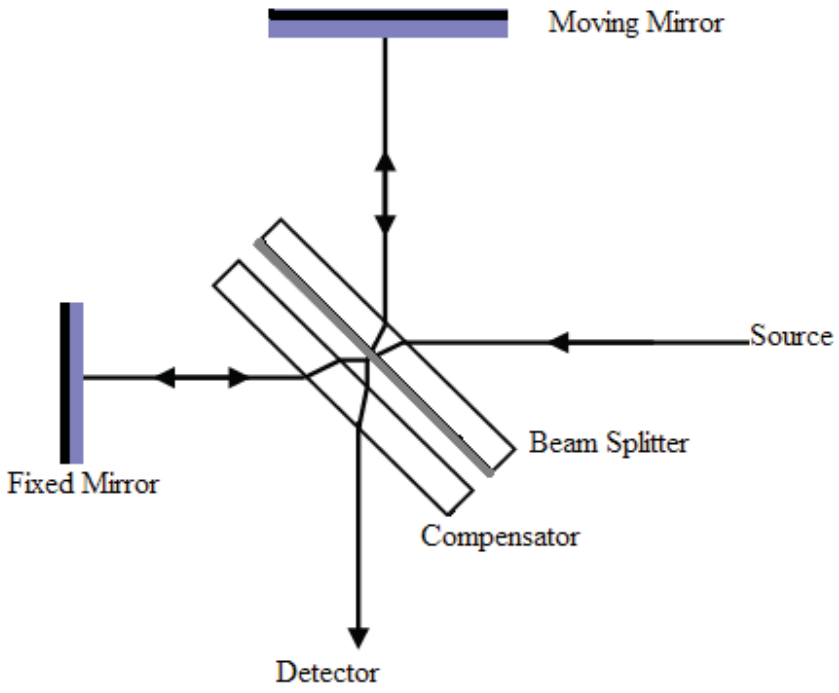

Figure 4.1 Michelson interferometer applied in the Bomem FTIR spectrometer. The incoming beam is split into two beams with equal intensity by the beam splitter. One beam is reflected by a moving mirror, and the other is reflected by a fixed mirror. The two reflected beams interfere at the beam splitter, and the interference pattern is detected. The compensator ensures that the two beams are in phase when the moving mirror is at the starting position.

The recombined signal is detected inside the Bomem interferometer, digitized and sent to the computer, which performs a Fourier analysis of the data. The light absorption/fluorescence intensity for each mirror position is function $f(x)$ and its Fourier transform $F(\sigma)$ represents the amplitude of each constituent sinusoid of wavenumber σ.

Figure 4.2 shows the optical configuration of our Bomem interferometer. From the discussion above, we see that the acquisition of the Bomem FTIR spectrum involves three steps:

First, the fluorescence beam generated from the heatpipe needs to enter the Bomem interferometer. To achieve this, the fluorescence is focused onto an optical fiber which transmits the light to the entrance port of the Bomem. The location of the fiber is carefully adjusted by a translation stage using an optical alignment procedure that involves sending a parallel beam of light through the interferometer in the reverse direction. The incoming beam is split by the beam splitter inside the Bomem, and the moving mirror creates the changing beam path difference. The interference pattern of the two beams is called the interferogram.

Second, the interferogram is detected by the detector inside the Bomem. After this, the measured interferogram signal is digitized and sent to the computer. The computer performs a Fourier analysis to transfer the interferogram into the spectrum. The longer the path that the moving mirror scans, the better the resolution. In the DA8 Bomem design the moving mirror can travel 2 meters, and the highest resolution that can be achieved is 0.016 cm^{-1}.

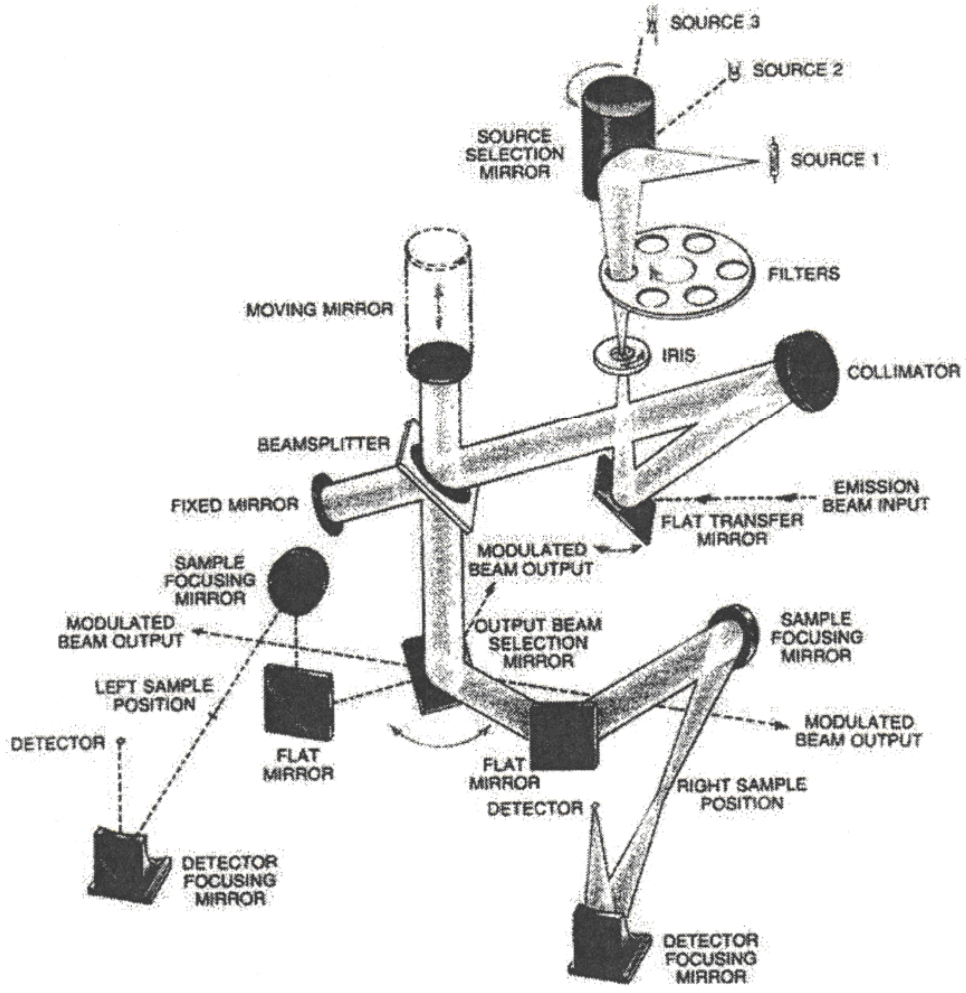

Figure 4.2 The Bomem DA8 series optical configuration.

The Bomem FTIR interferometer has some obvious advantages:

1. The built-in HeNe laser has a stable and accurate frequency. It acts as a calibration standard, which makes the Bomem interferometer internally self calibrated.

2. Because the Bomem FTIR interferometer obtains the light with all wavelengths simultaneously instead of individually, the time needed for it to finish a scan is much shorter, and the experimental conditions are much less likely to change during the scan.

3. The random noise can be significantly reduced by taking multiple scans which increases the signal to noise ratio.

The Bomem FTIR interferometer is a practical and accurate instrument to calibrate the frequency of laser beams and to acquire resolved fluorescence scans with very high resolution in the infrared spectral region.

4.2.5 Dual – Grating Monochromator (Spex 1404)

Another spectrometer used in our experiments to collect resolved fluorescence scans was the SPEX 1404, 0.85m dual-grating monochromator. The maximum spectral resolution of the Spex 1404 is 0.045A, which corresponds to $0.129cm^{-1}$ at $\lambda = 590nm$. Its absolute accuracy is $0.2cm^{-1}$ due to the stepping motor based grating angle control. The dispersion equation for the diffraction grating is:

$$d(\sin\theta_i + \sin\theta_r) = m\lambda \tag{4.5}$$

where d is the space between each groove, θ_i is the incident angle, θ_r is the diffraction angle, m is the diffraction order, λ is the wavelength. From this equation we see that the diffraction angle is wavelength dependent. When the servomotor controlled by the computer adjusts the position of the gratings with a chosen step size, the intensities of the various wavelength components in the incident beam at each wavelength are detected by the PMT which is attached to the exit slit assembly of the instrument.

Hongmin Chen and colleagues analyzed the $^7Li_2$ OODR resolved fluorescence spectra with a Spex 1404 double grating monochromator to study the polarization dependence and wavelength response of the monochromator. They detected fluorescence from the back, side and top of the heatpipe oven windows which contained $^7Li_2$ vapor. The reflection efficiency curves of the *P, Q* and *R* fluorescence lines were obtained. Details of this work can be found in reference [4].

Figure 4.3 shows an example of a scan obtained with the SPEX 1404 spectrometer. It shows the fluorescence from a $C^1\Pi_u \leftarrow X^1\Sigma_g^+$ pump transition. We can confirm the rotational quantum numbers of the terminal levels of the pump transition (J'' and J') by comparing the resolved fluorescence pattern to the known rotational energy level spacing from the ground state.

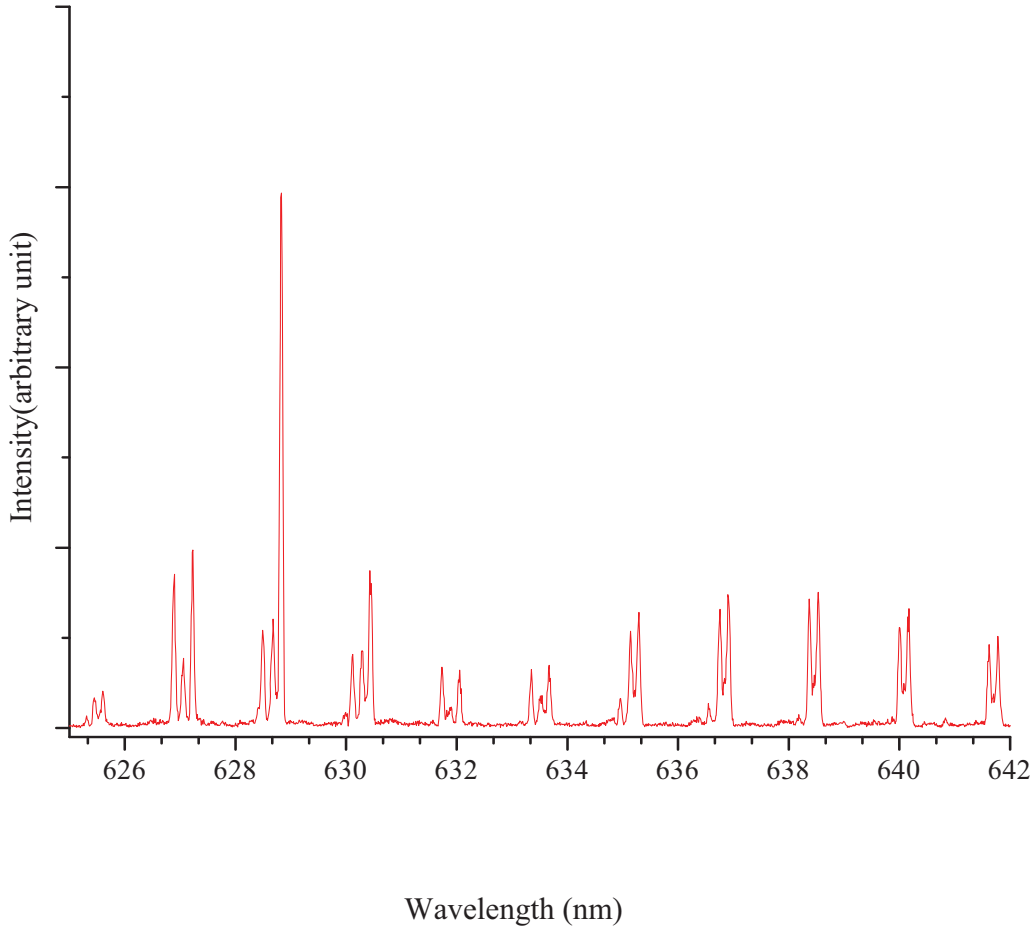

Figure 4.3 An example of the resolved fluorescence scan by SPEX 1404 spectrometer, which was used to confirm the pump transition in the Cs_2 polarization spectroscopic experiment.

4.2.6 Burleigh WA-1600 Wavemeter

A Burleigh 1600 wavemeter was used in our polarization experiments to measure the frequency of the TiSapphire laser when the frequency of the laser beam was outside the range of the Uranium lamp [14] used to calibrate the wavelength using optogalvanic spectroscopy. The absolute accuracy of this Burleigh 1600 wavemeter is 0.04 cm^{-1}. We used a single mode fiber to transmit the laser beam into the wavemeter. Figure 4.4 is a simple schematic of the Burleigh wavemeter. The wavemeter has two important components: a Michelson interferometer and a built-in He-Ne laser. The Michelson interferometer splits the input beam and generates interference fringes. The He-Ne laser with accurate well known frequency is the reference beam.

When the moving mirror of the Michelson interferometer moves a distance d, the number of fringes produced is given by:

$$m\lambda = 4n_{\lambda}d \tag{4.6}$$

where *m* is the number of fringes produced, λ is the wavelength of the input beam and n_{λ} is the refractive index of air for wavelength λ. A built-in He-Ne laser is used as the reference beam to accurately measure the distance d. For the reference beam, we can write:

$$m_0\lambda_0 = 4n_0d \tag{4.7}$$

Combining the two equations, we get:

$$\lambda = \left[\frac{m_o}{m}\right]\left[\frac{n_{\lambda}}{n_o}\right]\lambda_o \tag{4.8}$$

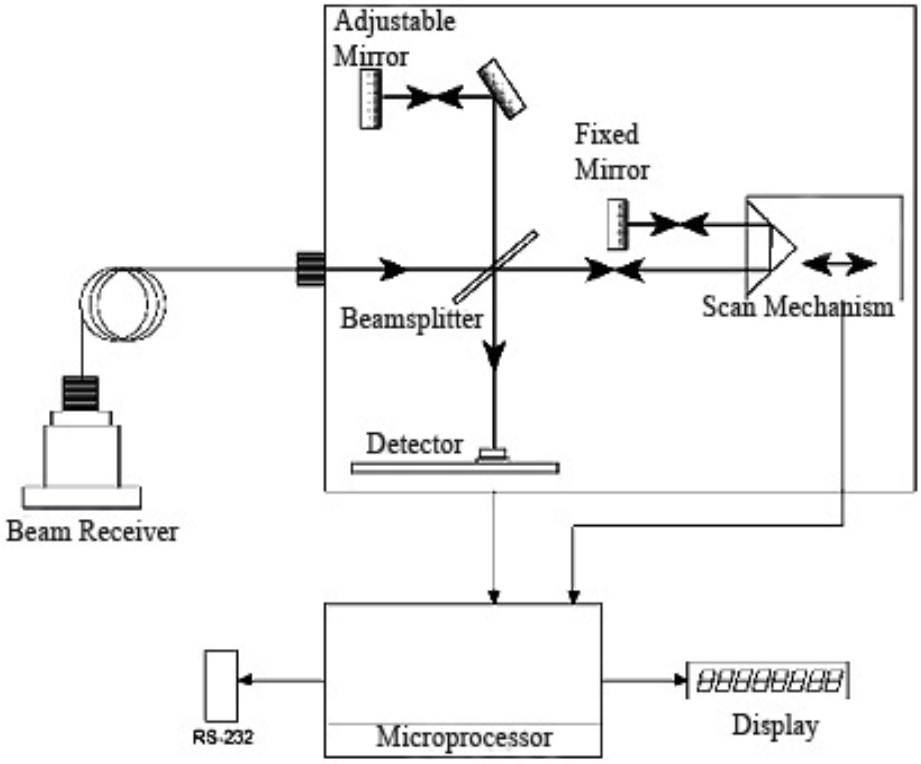

Figure 4.4 A simple schematic of the Burleigh wavemeter. The design is basically a Michelson interferometer. The interference pattern is detected and transferred to the microprocessor where it is analyzed to obtain the wavenumber. A stabilized single frequency He-Ne laser was used as reference The wavenumber is displayed digitally.

From this equation we see that the accuracy of the Burleigh wavemeter depends on the ratio of the number of fringes of the He-Ne reference laser beam and the input laser $\left[\frac{m_o}{m}\right]$, the ratio of the refractive indexes $\left[\frac{n_\lambda}{n_o}\right]$ and the wavelength of the reference beam λ_0.

In order to determine systematic measurement errors, we measured the reading errors of the Bomem and the Burleigh WA-1600 wavemeter at different spectral ranges based on an optogalvanic calibration spectrum using the Uranium lamp and its Atlas of a calibrated Uranium spectrum [14]. Table 4.1 lists the reading errors of the Bomem and the Burleigh WA-1600 wavemeter.

Table 4.1 Reading errors of the Bomem and the Burleigh WA-1600 wavemeter. The average magnitude of the Burleigh wavemeter system error is 0.0217 cm^{-1} and the root mean square (rms) is 0.0247 cm^{-1}. The average magnitude of the Bomem system error is 0.0268 cm^{-1} and the rms error is 0.027 cm^{-1}.

Uranium Atlas (cm^{-1})	Burleigh (cm^{-1})	Bomem (cm^{-1})	Burleigh Error (cm^{-1})	Bomem Error (cm^{-1})
11041.3737	11041.334	11041.3438	0.0397	0.0299
11010.0931	11010.087	11010.0747	0.0061	0.0184
11046.0148	11045.978	11045.9868	0.0368	0.028
11082.1804	11082.173	N/A	0.0074	N/A
11093.1953	11093.17	11093.17	0.0253	0.0253
11112.8638	11112.831	11112.8414	0.0328	0.0224
11120.5186	11120.508	11120.4873	0.0106	0.0313
11167.6798	11167.643	11167.6525	0.0368	0.0273
11193.6145	11193.602	11193.5879	0.0125	0.0266
11247.4602	11247.447	11247.434	0.0132	0.0262
11248.3361	11248.322	11248.3069	0.0141	0.0292

4.3 Rubidium and Cesium Density

The densities of the Rubidium and Cesium dimer molecules can be estimated in general as a percentage of atomic density (4 to 5%). Nesmeyanov introduced a formula to calculate the vapor pressure of different chemical elements [13]:

$$\lg p_{mm} = A - \frac{B}{T} + CT + D\lg T \qquad (4.9)$$

Here p_{mm} is the pressure of the atoms or molecules in Torr, T is the temperature inside the heat-pipe oven in K, and A,B,C,D are constants . Table 4.2 gives the values of the constants for Rb, Rb_2, Cs, and Cs_2.

Table 4.2 The constants in Nesmeyanov's formula for different species.

Species	A	B	C	D
Rb	15.88253	4529.635	0.00058663	-2.99138
Rb_2	41.2753	7226.316	0.00333213	-11.8551
Cs	8.22127	4006.048	0.00060194	-0.19623
Cs_2	18.22054	6064.472	0.00009016	-3.45395

After measuring the pressure of the atomic species or the molecule of interest, its density can be obtained from the ideal gas law:

$$n = \frac{P}{kT} \tag{4.10}$$

Here n is the density of the atom or molecule interested, k=1.386504E-23 J/K.

Table 4.3 Temperature, pressure and densities of the Rb_2 and Cs_2 dimers.

Dimer	T(K)	P(Torr)	n(cm^{-3})
Rb_2	480	8.112E-5	1.62E12
Cs_2	550	5.94E-3	1.03E14

4.4 The Experiment

4.4.1 Summary of the Experiment

We applied collisional orientation transfer facilitated V-type optical-optical double-resonance (OODR) polarization spectroscopy technique to study the A/b complex states of Rb_2 and Cs_2. This technique is well suited to observe selected transitions in the congested spectra of Rb_2 and Cs_2. Due to collisional transfer of orientation, a series of well-separated spectral lines associated with nearby levels that were oriented and polarized were generated. A circularly polarized pump laser beam, tuned to a chosen transition, creates an anisotropic distribution of magnetic sublevel populations (net orientation) in ground state rovibrational levels. The counter-propagating probe laser

beam is linearly polarized, which can be considered to be made up of equal left and right components of circular polarization. When the probe frequency is tuned to a transition sharing either level with the pump transition, the orientation created by the pump causes the two components different absorption coefficients (circular dichroism) and different indices of refraction (circular birefringence). As a result, the two components no longer sum to the initial linear polarization when the probe beam exits the heat pipe oven. Instead, the beam has a slight elliptical polarization and some fraction of it is transmitted through a final crossed linear polarizer before reaching the detector.

4.4.2 Details of the Experiments

The experimental setups for the Rb_2 and Cs_2 polarization experiments were similar. As shown in Figure 4.5, the Rb_2 or Cs_2 metal was loaded at the center of a five-arm heat-pipe oven, which was kept at a temperature of 480 K for the Rb_2 experiment and 550 K for the Cs_2 experiment, with 1 to 3 Torr of argon buffer gas pressure. A CR-699-29 tunable single mode laser from Coherent with DCM dye was used as the circularly polarized pump laser in the Rb_2 polarization experiment, tuned to known $B'^1\Pi_u(2,\ 70) \leftarrow X^1\Sigma_g^+(0,\ 71)$ transition. In the Cs_2 polarization experiment, a Kiton red 620 dye laser served as pump laser. Multiple $C^1\Pi_u(v',\ J') \leftarrow X^1\Sigma_g^+(v'',\ J'')$ pump transitions were used during the experiment to get a wider range rotational levels with different J values per vibrational level. A linearly polarized CR-899-29 Ti-Sapphire laser served as the probe laser for both of the experiments. The pump and probe lasers were counterpropagating and overlapped at the center of the heatpipe oven with a crossing

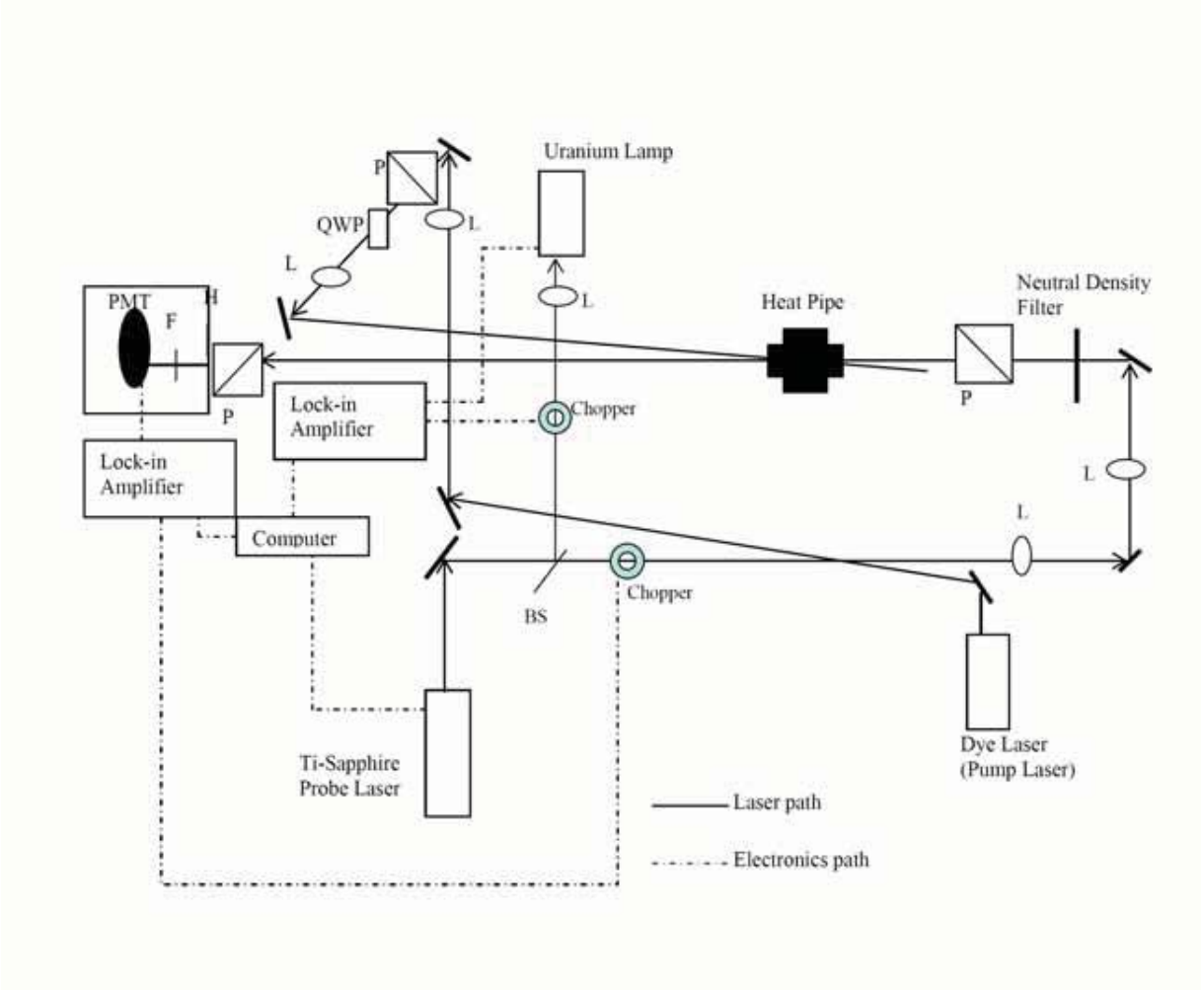

Figure 4.5 Schematic diagram of the Rb_2 and Cs_2 polarization spectroscopy experimental setup. BS, beam splitter; L, lens; PMT, photomultiplier tube; P, linear polarizer; QWP, Babinet-Soleil compensator; H, pin hole; F, filter.

angle that was minimized so as to maximize the overlap area. The spot sizes (defined as the radius at $1/e^2$ intensity) of the pump (1.2 mm) and probe (0.9mm) laser beams in the interaction region were measured with a razor blade technique [17]. Two lenses were placed in the path of each laser beam for collimation inside the heat pipe oven.

A Glan Thompson linear polarizer and a $\lambda/4$ Babinet-Soleil compensator from Karl Lambrecht Inc, Chicago were used to circularly polarize the pump beam. Two linear polarizers in the probe laser beam path (one before and one after the heat pipe oven) were oriented with their transmission axes at a 90 degree angle for maximum extinction of the probe laser when it was off resonance. A power meter (Coherent LabMax TO) with a sensitive detector (LM-2) placed after the second polarizer was used to make fine adjustments of the orientation of the second polarizer to create an optimal extinction ratio of 10^{-6} (and then removed for data acquisition). The observed ratio includes effects of window birefringence and circular dichroism.

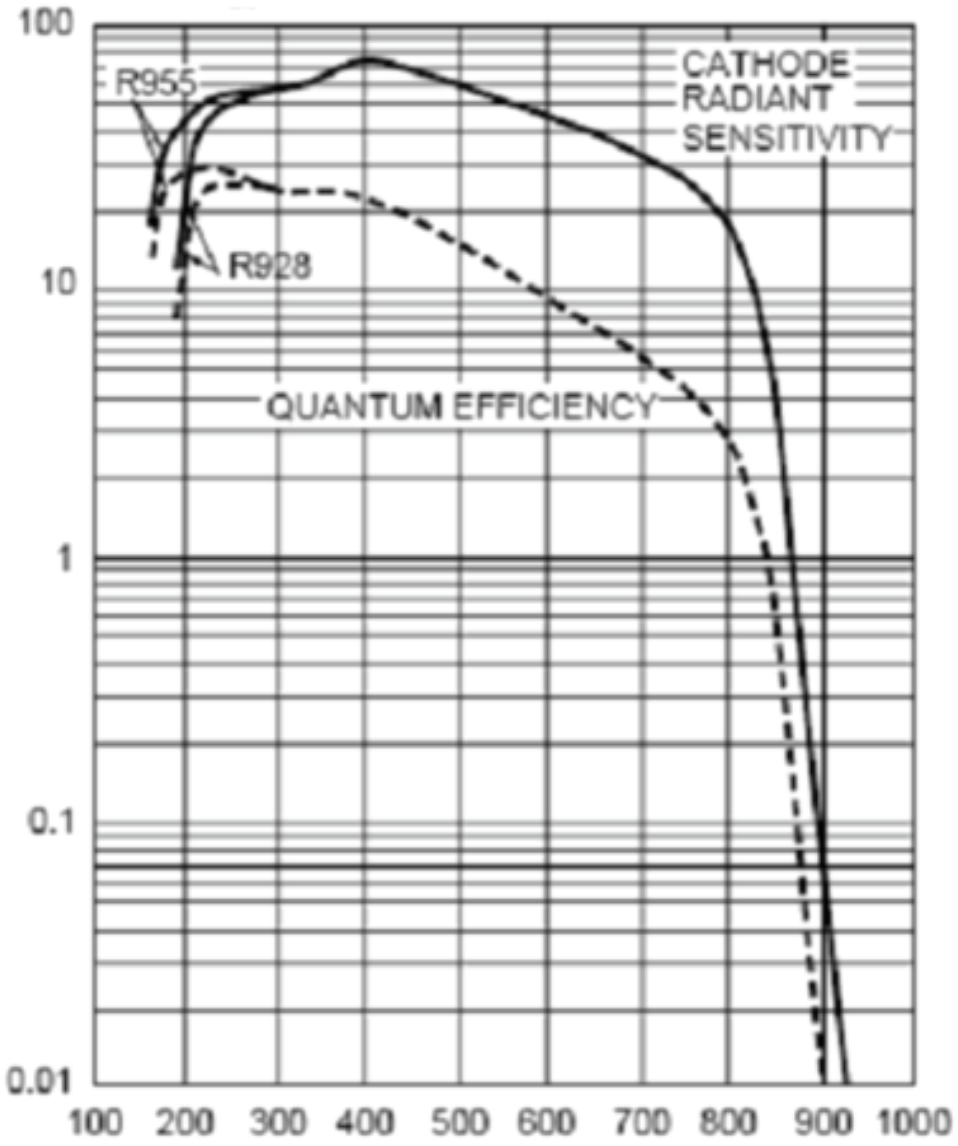

Figure 4.6 Spectral response curve of the R928 photomultiplier tube used in the Rb_2 polarization experiment.

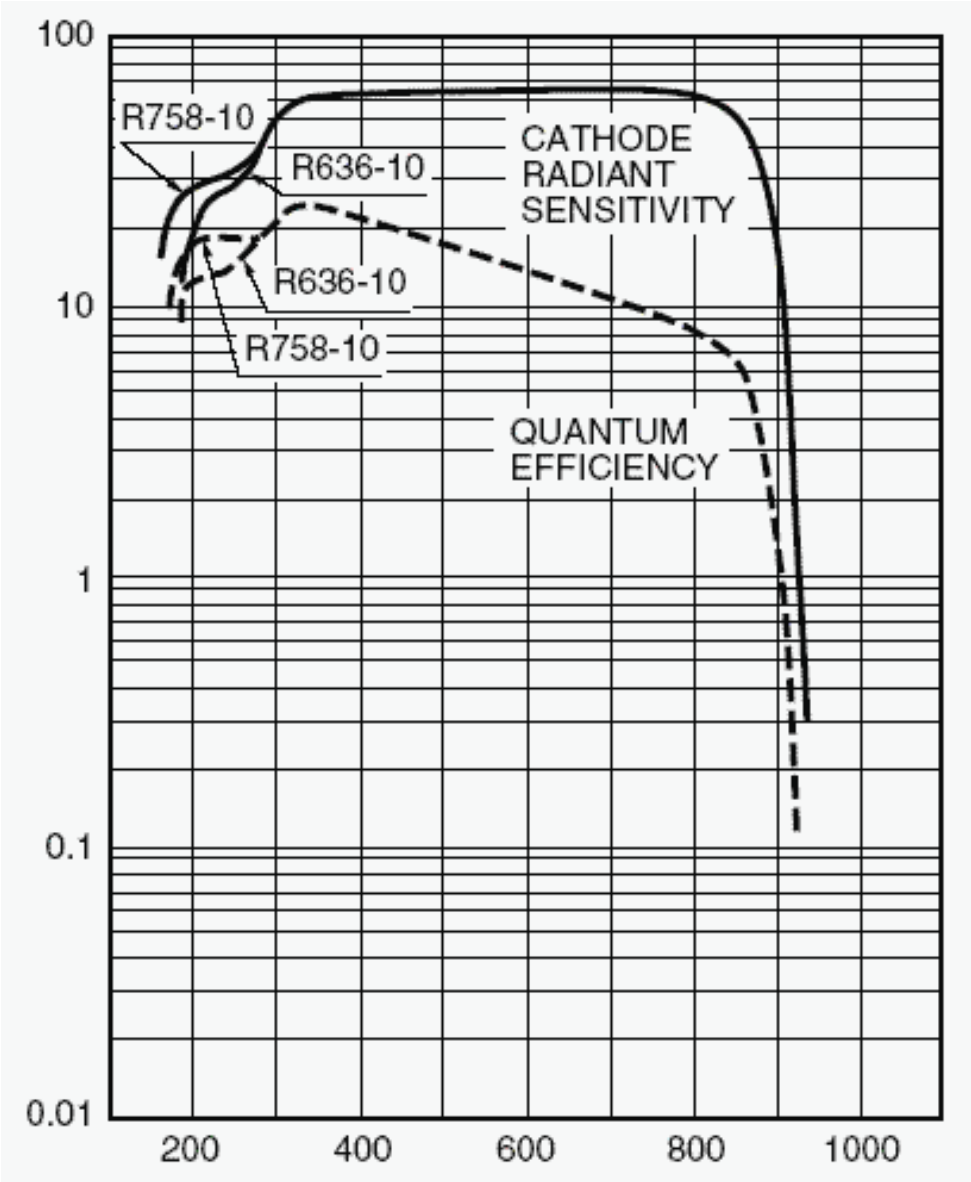

Figure 4.7 Spectral response curve of the R636-10 photomultiplier tube used in the Cs_2 polarization experiment.

A photomultiplier tube (Hamamatsu R928) which is sensitive to light in the range of 200nm to 850nm was used to detect the polarization signal in the Rb_2 experiment. Figure 4.6 gives the spectral response curve of the R928 tube. In the Cs_2 experiment, the TiSapphire scanned at a longer wavelength range than that in the Rb_2 experiment, so we chose the Hamamatsu R636-10 photomultiplier tube to detect the polarization signal. Its spectral response range is from 200 nm to 930 nm. Figure 4.7 shows the spectral response curves presented by Hamamatsu Photonics. To reduce the possibility that scattered light from the pump beam detected by the PMT detector, we placed 780 nm and 800 nm long pass filters before the PMT detector to block the scattered light.

The output from the PMT was amplified using a lock-in amplifier (Stanford Research Systems SR 850) for phase sensitive detection. The pump laser was modulated at a frequency of 980 Hz using a mechanical chopper (Stanford Research Systems SR 540). The pump laser was calibrated using an Iodine Atlas [8], with corrections from [9]. The estimated accuracy was 0.004 cm^{-1}. The Ti:Sapphire laser was calibrated by comparing optogalvanic spectroscopy signals from a Uranium lamp to line positions in the Uranium Atlas [14] when it scanned above 11000 cm^{-1}. The listed wavenumbers in the Uranium Atlas are accurate to ±0.003 cm^{-1}. At least one Uranium spectral line was included in each of the spectral scans for calibration purpose. A Burleigh 1600 wavemeter and BOMEM DA8 FTIR were used to calibrate the Ti:Sapphire frequency when it scanned below 11000 cm^{-1}.

Because the Franck-Condon factors for the Cs_2 pump transitions were weaker by a factor of 100 than for the Rb_2 polarization spectrum, the signal-to-noise ratio was smaller,

and fewer collisional satellites were observed in the Cs_2 polarization spectroscopy than with Rb_2 ($\Delta J \leq 12$ rather than ≤ 58). Also, due to spectral congestion, the C- X pump transitions were difficult to isolate. Collisional lines helped us to expand the data field but can only be observed if orientation is transferred from the ground state level labeled by the pump laser to a neighboring level. A quantitative study of the transfer of population and orientation in collisions of NaK molecules with argon and potassium atoms has been carried out and reported in [19] and [20]. These references discuss the transfer of orientation following the discussion of Ref. [7] and also present a complete analysis of polarization spectroscopy line shapes, extending the textbook presentation in [6].

4.5 The Pump Transitions

4.5.1 Franck-Condon factors (FCF) of the Pump Transitions

In a transition, the vibrational overlap of the wavefunction between the the initial and excited state rovibrational levels is called the Franck-Condon factor (FCF). The FCF or the transition dipole moment matrix element can be used to predict the strength of a rovibronic transition. To select pump transitions with reasonable intensity for our polarization experiments, it is necessary to know the FCF's.

The FCF's can be calculated by solving the radial Schrodinger equation of the involved states if the potential curves of both of the states are known. We used the LEVEL program written by Dr. Le Roy [11] from University of Waterloo for the B-X system of the Rb_2 dimer [16] and the C-X system of the Cs_2 dimer [2].

4.5.2 Pump Transition for the Rb_2 Polarization Spectroscopy Experiment

For the pump laser transition in the Rb_2 A~b global deperturbation study a DCM dye laser was chosen based on a good FCF within the B-X system. The laser frequency 14736.184 cm^{-1} used for the main pump transition $B^1\Pi_u(2,70) \leftarrow X^1\Sigma_g^+(0,71)$ also overlapped accidentally with the $B^1\Pi_u(2,85) \leftarrow X^1\Sigma_g^+(0,84)$ transition. The Franck-Condon factors of these transitions were 0.2139 and 0.2126, respectively.

4.5.3 Pump Transitions for the Cs_2 Polarization Spectroscopy Experiment

The tunable single mode Coherent CR-699 ring dye laser with Kiton Red 620 dye was used as pump laser in the Cs_2 polarization spectroscopy experiment. We chose $C^1\Pi_u \leftarrow X^1\Sigma_g^+$ transitions as our pump transitions because the wavelengths of the transitions between these two electronic states fall into the lasing range of the Kiton Red 629 dye laser.

Several techniques of high resolution spectroscopy have been applied to the study of the $C^1\Pi_u \leftarrow X^1\Sigma_g^+$ transition. Kasahara *et al*. [10] determined the molecular constants of $C^1\Pi_u$ (v = 7 – 18) rovibrational levels from their high resolution spectra by the Doppler - free Optical - Optical Double Resonance (OODR) polarization technique.

Table 4.4 FCF table of the Cs_2 C-X states. The numbers listed in the table are the FCFs $\times 10000$.

	V'										
V"	0	1	2	3	4	5	6	7	8	9	10
0	6978	2906	54	56	4	3	0	0	0	0	0
1	1746	3249	4637	186	155	17	8	1	1	0	0
2	855	1528	1453	5465	301	335	37	23	1	2	0
3	284	1281	853	678	5798	385	599	58	57	2	6
4	92	593	1375	301	338	5743	416	936	72	118	2
5	29	273	789	1244	31	198	5414	374	1337	68	215
6	10	105	464	821	1019	29	151	4903	279	1771	45
7	4	41	212	618	732	802	234	141	4246	160	2188
8	1	16	95	326	716	568	623	575	152	3496	54
9	0	6	41	168	421	754	380	498	988	168	2703
10	0	2	17	78	247	484	749	209	420	1418	174
11	0	1	7	36	126	325	506	716	80	381	1815
12	0	0	2	15	62	178	392	491	673	10	373
13	0	0	1	6	28	96	230	444	444	635	7
14	0	0	0	2	12	47	133	274	481	374	609
15	0	0	0	1	5	21	69	173	308	507	291

They also found that a number of $C^1\Pi_u$ (v>12, *J*) levels were highly mixed with the $(2)^3\Pi_u$ levels. The mixed levels are not purely singlet or triplet. Due to spin – orbit perturbation, each perturbed level has a mixture of the singlet character and triplet character.

Raab *et al.* [15] used the Doppler- free polarization spectroscopy and Optical - Optical Double Resonance (OODR) to study the Cs_2 band system around λ=625 nm and recorded more than 2000 completely resolved rotational lines in the $C^1\Pi_u \leftarrow X^1\Sigma_g^+$ band system. Twenty six different $C \leftarrow X$ transitions (ground state $3 \leq v'' \leq 8$ and $52 \leq J'' \leq 121$) were confirmed for the Cs_2 polarization spectroscopy experiment, and 20 of them served as pump transitions in the experiment. Table 4.4 gives the FCFs of the $C \leftarrow X$ transitions. These results guided us in choosing the right pump transitions. Table 4.5 is a list of the pump transitions we used in the Cs_2 polarization experiment.

Table 4.5 A list of the pump transitions that were used in the Cs_2 polarization spectroscopic experiment. Due to weak Franck-Condon factors from the ground state to the A/b perturbed state, we could only observe angular momentum changes up to ΔJ_{max} = 12 compared to ΔJ_{max} = 58 in the Rb_2 experiment. Multiple pump transitions were needed to increase the number of rotational satellite lines that could be observed.

calibrated wavenumber(cm^{-1})	C state		X state	
	v'	J'	v''	J''
15898.830	7	91	6	92
15886.266	8	63	7	64
15886.296	8	69	7	70
15898.554	7	73	6	74
15886.341	8	75	7	76
15898.606	7	77	6	78
15886.388	8	81	7	82
15927.417	5	85	4	84
15898.726	7	85	6	86
15898.748	7	86	6	87
15886.446	8	87	7	88
15886.470	8	89	7	90
15890.915	8	95	7	94
15891.143	8	99	7	98
15928.508	5	99	4	98
15923.905	5	99	4	100
15891.361	8	103	7	102
15899.073	7	105	6	106
15899.361	7	120	6	121
15924.670	5	121	4	122
15898.369	7	51	6	52

References:

1. Anderson, M. H., Ensher, J. R., Matthews, M. R., E.Wieman, C., and Cornell, E. A., Science **269**, 198 (1995).
2. Bai, J., Ahmed, E. H., Beser, B., Guan, Y., Kotochigova, S., Lyyra, A. M., Ashman, S., Wolfe, C. M., Huennekens, J., Xie, F., Li, D., Li, L., Tamanis, M., Ferber, R., Drozdova, A., Pazyuk, E. A., Stolyarov, A. V., Danzl, J. G., Nagerl, H. C., Bouloufa, N., Duleiu, O., Amiot, C., Salami, H., and Bergeman, T., Phys. Rev. A **83**, 032514 (2011).
3. Bradley, C. C., Sackett, C. A., Tollet, J. J., and Hulet, R. G., Phys.Rev.Lett. **75**, 1687 (1995).
4. Chen, H., Li, L., Lazarov, G., Wang, X., Lyyra, A. M., Huennekens, J., and Field, R. W., J. of Mol. Spec. **196**, 197 (1999).
5. Davis, K. B., Mewes, M.-O., Andrews, M. R., Druten, N. J. V., Drufree, D. S., Kum, D. M., and Ketterle, W., Phys.Rev.Lett. **75**, 3969 (1995).
6. Demtroder, W., *Laser Spectroscopy, Basic Concepts and Instrumentation*, Second Enlarged ed. (Springer-Verlag, Berlin, 1996).
7. Derouard, J., Chem. Phys. **84**, 181 (1984).
8. Gerstenkorn, S. and Luc, P., *The Aim´e Cotton Iodine Atlas*, Editions du CNRS ed. (Paris, 1978).
9. Gerstenkorn, S. and Luc, P., Rev. Phys. Appl. **14**, 791 (1979).
10. Kasahara, S., Hasui, Y., Otsuka, K., Baba, M., Demtroder, W., and Kato, H., J. Chem. Phys. **106**, 4869 (1997).

11. LeRoy, R. J., LEVEL 8.0: A computer program for solving the radial Schrodinger equation for bound and quasibound levels (University of Waterloo Physics Research Report 2007).

12. Michelson, A. and Morley, E., American Journal of Science **34** (203), 333 (1887).

13. Nesmeyanov, A. N., *Vapor Pressure of the Chemical Elements*. (1963).

14. Palmer, B. A., Keller, R. A., and Engleman, R., Jr., LASL Report No. LA-8251-MS (Los Alamos Scientific Laboratory, Los Alamos, NM, 1980).

15. Raab, M., Honing, G., Demtroder, W., and Vidal, C. R., J. Chem. Phys. **76**, 4370 (1982).

16. Salami, H., Bergeman, T., Beser, B., Bai, J., Ahmed, E. H., Kotochigova, S., Lyyra, A. M., Huennekens, J., Lisdat, C., Stolyarov, A. V., Dulieu, O., Crozet, P., and Ross, A. J., Phys. Rev. A **80**, 022515 (2009).

17. Skinner, D. R. and Whitcher, R. E., J. Phys. E. **5**, 237 (1972).

18. Vidal, C. R. and Cooper, J., J. Appl. Phys. **40**, 3370 (1969).

19. Wolfe, C., Ph. D. Thesis, Lehigh University, 2010.

20. Wolfe, C., Ashman, S., Bai, J., Beser, B., Ahmed, E. H., Lyyra, A. M., and Huennekens, J., J. Chem. Phys. **134**, 174301 (2011).

CHAPTER 5

EXPERIMENTAL RESULTS

We have observed a large number of rovibrational levels of the A/b complex (consisting of the $A^1\Sigma_u^+$ and $b^3\Pi_u$ electronic states) in $^{85}Rb_2$ and Cs_2 using V-type optical-optical double resonance polarization spectroscopy. A circularly polarized laser was used as the pump laser and a linearly polarized laser was used as the probe laser.

5.1 Collision Induced Orientation Transfer

The main electric dipole rovibrational transitions from pump laser lower level with vibrational and rotational quantum number v", J" the transitions to the excited state rovibrational levels v', J' = J"-1 (P line) and v', J' = J"+1 (R line) for vibrational levels v' with good Franck-Condon factors. In addition to the *R, P* doublets, expected from a single pump laser, we have observed molecular orientation transfer based probe laser signals from a large number of collisionally populated rotational levels. For a homonuclear molecule these collisional satellite lines occur in steps of $\Delta J = \pm 2$ [1-5]. From Figures 1 and 3, it is obvious that collisional lines only appear when the difference of the rotational quantum numbers between the directly pumped 'parent' line and the collisionally induced lines is an even number $\Delta J = \pm 2, \pm 4, \ldots \pm 2k$ lines. This is

because in homonuclear molecules like $^{85}Rb_2$ and Cs_2, only transitions that can preserve the symmetry with respect to an interchange of the nuclei are allowed which is consistent with the selection rules

$$a \leftrightarrow a$$

$$s \leftrightarrow s$$

This rule breaks down for heteronuclear molecules because the interchange of the nuclei breaks the symmetry of the wavefunction. S. Antonova *et al.* [6] observed $\Delta J = \pm 1, \pm 3, \ldots$ collisional satellite lines in their $^6Li^7Li$ spectra. But the intensity of these extra lines was weak, indicating a breakdown of the symmetric–symmetric (s-s) and antisymmetric - antisymmetric (a-a) selection rule in the $^6Li^7Li$ spectra. Thus, in the context of collisional energy transfer the $^6Li^7Li$ appears to be heteronuclear.

The satellite lines observed in our polarization spectra are due to collision induced transfer of population with anomalous magnetic sublevel distribution from the pump laser terminal levels to nearby energy levels. In these collisions the anisotropic distribution of population as a function of the magnetic quantum number M_J created by the circularly polarized pump laser survives in the collisional energy transfer. It is this additional portion of the population with angular momentum orientation in thermally populated rovibrational levels in the ground state that leads to probe laser signals. The rovibrational level populations generated in this manner by collisional energy transfer then served as additional ground state levels with molecular angular momentum orientation for new $A^1\Sigma_u^+ \leftarrow X^1\Sigma_g^+$ probe laser transitions. In Fig. 5.1 there are collisional satellite lines up to ΔJ = -58 (from J"=71 to J"=13) and ΔJ = +18 up to J"= 89 in steps of $\Delta J = \pm 2$, in $^{85}Rb_2$ [1-4]. The intensity of the collisional satellite lines becomes weaker the higher the

angular momentum change. Observation of such a large number of collisional satellite lines, that could be easily identified, with such a large change in the angular momentum ΔJ in steps of $\Delta J = \pm 2, \pm 4$ etc. in our polarization spectra was possible because of a high signal to noise ratio in our experiment. As a result, the collisional energy transfer signals revealed a lot of additional energy level information about the A/b perturbed state of Rb_2 beyond the expected parent R,P lines (see Fig. 5.2).

Collision induced energy transfer in polarization spectra has been observed previously. Teets *et al.* [7] obtained polarization spectra of Na_2 showing inelastic collisional transfer in 1976 by combining the methods of polarization spectroscopy and labeling of the pump laser lower level by using a circularly polarized pump laser. In this early work the inert gas pressure in the sample was a few hundred Torr, leading to collisional broadening of the polarization spectra and subsequent loss of resolution.

M.D. Rowe and A.J. McCaffery [8] observed inelastic collision- induced rotational transfer lines of the Li_2 $A^1\Sigma_u^+$ state with ΔJ values up to 18. C. Ottinger and M. Schroder [9] monitored collision – induced rotational transitions of the labeled $A^1\Sigma_u^+ \leftarrow X^1\Sigma_g^+$ transitions of Li_2. They applied semiclassical time–dependent perturbation theory to analyze their experimental data and were able to reproduce the relative magnitude of the measured cross sections, including the $+\Delta J/-\Delta J$ asymmetry, which matched well with the experiment. A theoretical analysis of this problem was presented by J. Derouard [10] for the experimental data obtained by references [11], [8]

and [9]. McCaffery and coworkers [12-15] demonstrated that the line-shapes of the collisional lines can be used to determine differential cross sections.

Collision induced energy transfer in the of the B state of Cs_2 was observed by U. Diemer *et al*. [16] in their polarization spectroscopy experiment. In the high resolution polarization spectroscopy study of the $B^1\Pi \leftarrow X^1\Sigma^+$ transition of $^{39}K^{85}Rb$ molecule, N. Okada et al. [17] observed six types of probe signals occurring in optical-optical double resonance spectroscopy, including the collision-induced transfer signals. More information about collision-induced orientation transfer can be found also in the work of S. Kasahara and coworkers [18-20].

More recently, C.M. Wolfe and coworkers [21] studied quantitatively the transfer of population and orientation in an inelastic collision study of NaK molecules with argon and potassium gas as perturbers. This heteronuclear diatomic system is more suitable for such a study than the homonuclear Rb_2 and Cs_2 dimer molecules since there are fewer electric dipole selection rules for the transitions between electronic states, such as the limiting 'gerade-ungerade' rule. A rate equation model was created to study the intensities of the collisional lines as a function of argon pressure and heatpipe oven temperature.

A common feature in all of the experiments mentioned above is that satellite lines due to collision – induced transfer of molecular orientation significantly expand the spectral range available experimentally.

5.2 The Experimental Spectra

5.2.1 The $^{85}Rb_2$ Polarization Spectra

Figure 5.1 illustrates part of the spectra we obtained from our Rb_2 polarization experiment and shows Rb_2 $\Delta J_{\max}$ up to 58. The circularly polarized pump laser was tuned to the $B^1\Pi_u(2,70) \leftarrow X^1\Sigma_g^+(0,71)$ transition, and the probe laser was scanned over the various $A^1\Sigma_u^+(v',J') \leftarrow X^1\Sigma_g^+(0,J'')$ transitions from 11380 cm^{-1} to 12580 cm^{-1}. In order to also record the weaker signals, the lock-in amplifier sensitivity was adjusted for the strong parent lines $\Delta J = \pm 1$ to a less sensitive scale. The P (71) line and the R (71) line are the direct signals from the $B^1\Pi_u(2,70) \leftarrow X^1\Sigma_g^+(0,71)$ transition and the weaker lines are the satellite lines due to collision-induced orientation transfer. Figure 5.2 shows the observed data from our Rb_2 polarization experiment. The solid circles are the signals corresponding to the direct parent lines and the blank circles are signals due to collision-induced energy transfer.

In a global deperturbation analysis for the spin – orbit interaction performed by Dr. Tom Bergeman at Stony Brook, our polarization data was merged with data from several other sources. For the $A^1\Sigma_u^+$ and $b^3\Pi_u$ states, an analytic potential (Hannover form) was incorporated in a discrete variable representation of the Hamiltonian matrix for numerical energy-level calculations [22].

Rb_2 $A^1\Sigma_u^+ \leftarrow X^1\Sigma_g^+$ Polarization Spectrum

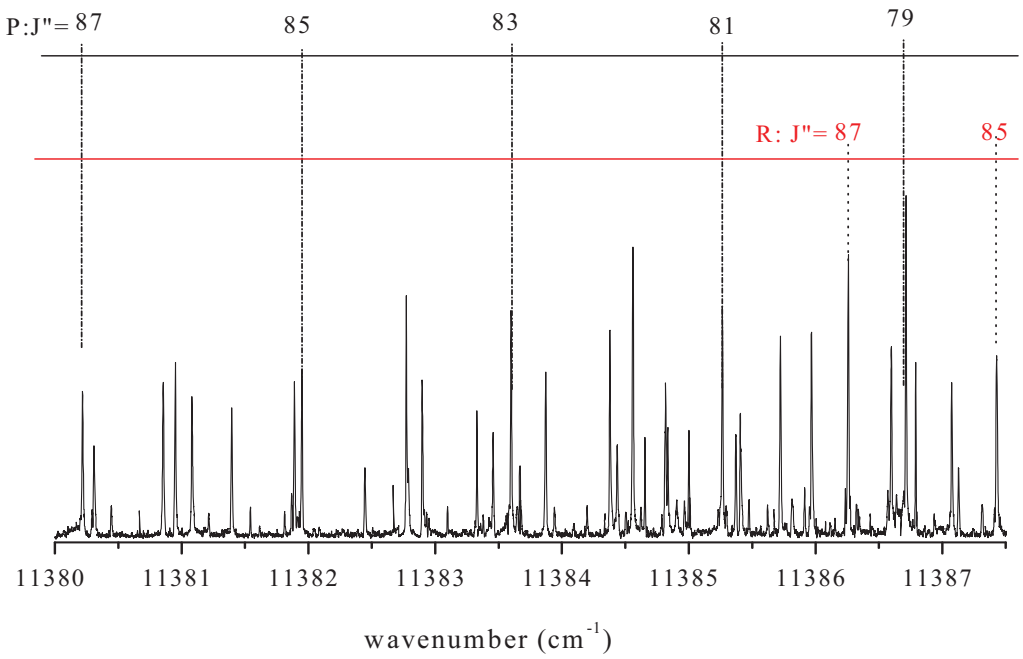

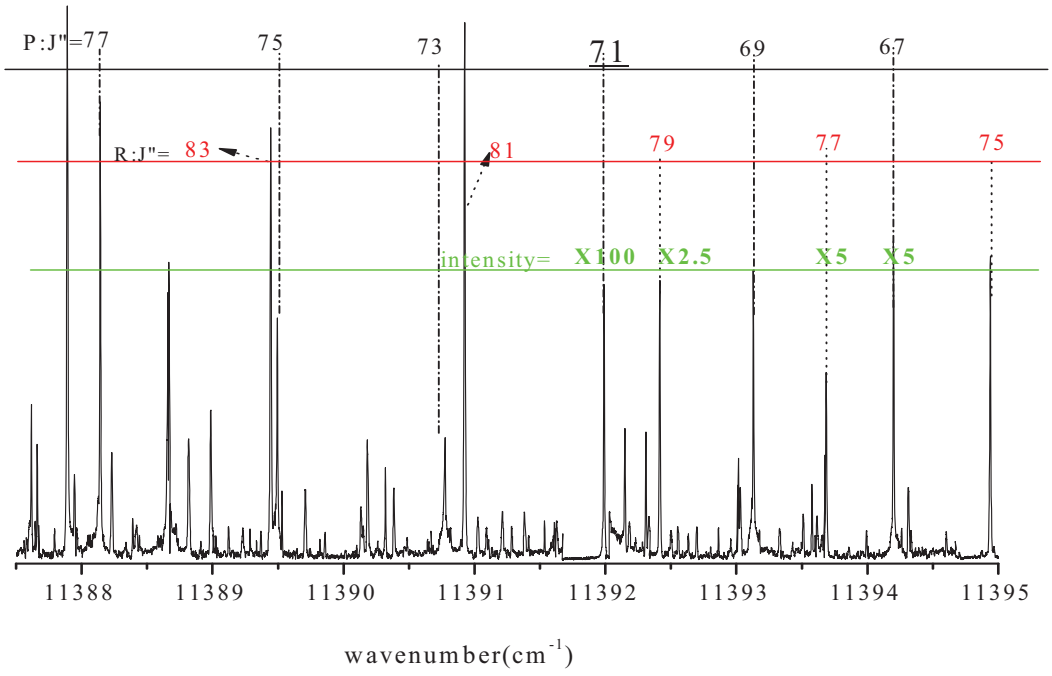

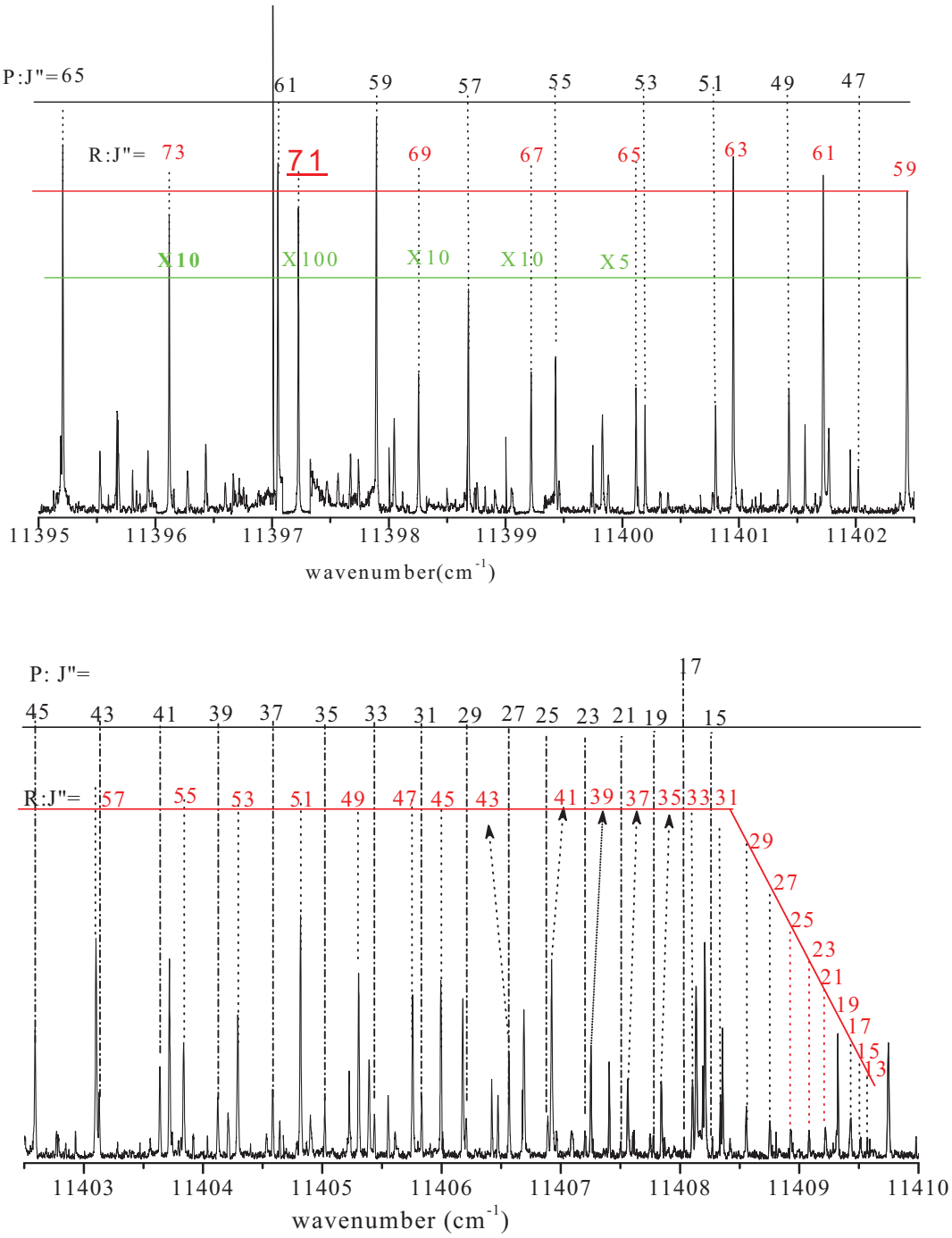

Figure 5.1 Rb_2 polarization spectrum with ΔJ_{max} up to 58. The pump laser was tuned to the $B^1\Pi_u(v'=2, J'=70) \leftarrow X^1\Sigma_g^+(v''=0, J''=71)$ transition and the probe laser was scanned over the various $A^1\Sigma_u^+(v', J') \leftarrow X^1\Sigma_g^+(v''=0, J'')$ transitions from 11380 cm^{-1} to 12580 cm^{-1}.

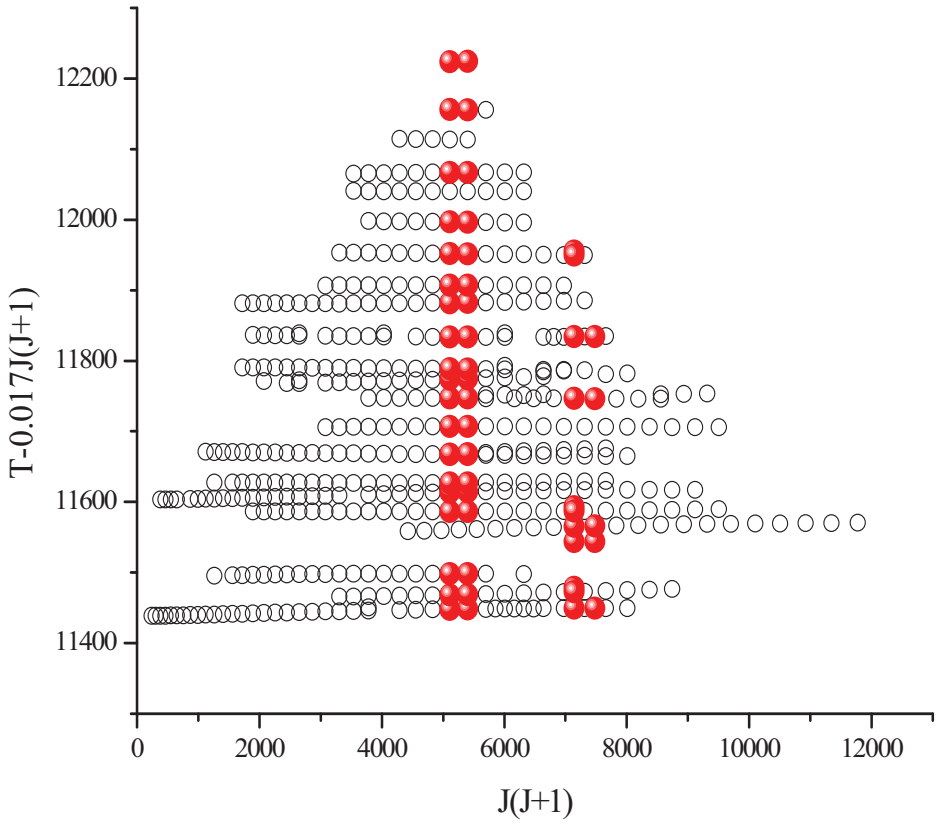

Figure 5.2 Observed energies of the Rb_2 A/b states. The rotational energy 0.017J(J+1) cm^{-1} has been subtracted from the energies. Here the rotational constant, which varies with the vibration quantum number, has been approximated by a constant value 0.017 cm^{-1}. The solid circles are the signals which do not involve collision-induced energy transfer. The blank circles are signals due to collision-induced energy transfer.

From our Rb_2 polarization spectra, 881 of the experimental peaks, including the direct *P, R* pairs and the collision induced satellite lines were identified. For the same vibrational level, the *P* (*J*″ +1) line and *R* (*J*″ -1) lines of a certain upper state rotational quantum number *J'*=*J*″ should have the same term values even though they appear as distinct lines in the spectra due to different ground state term values. A total of 453 different term values were obtained from our identified (in terms of their rotational and vibrational quantum numbers) experimental probe laser scan peaks that originated from the pump laser lower level v″ = 0. The identified peaks of the Rb_2 polarization spectra are listed in the Appendix. Because the $A^1\Sigma_u^+$ and $b^3\Pi_u$ electronic states of Rb_2 are highly perturbed, many rovibrational levels are of mixed singlet-triplet character. The quantum number '*n*' is applied to denote different vibrational levels in the combined $A^1\Sigma_u^+$ and $b^3\Pi_u$ complex of states instead of the traditional vibration quantum number 'v' in each state traditionally denoted by v_A and v_b.

More than 1000 experimental spectral lines from the Rb_2 polarization spectra are still unidentified. Further analysis of the rest of the Rb_2 polarization is in progress. These transitions are likely to originate from higher lying ground state vibrational levels populated by fluorescence decay from the pump laser upper level (see Fig 5.3). In such levels the probe laser signals in the polarization spectroscopy originate from that the portion of the population added to the original thermal population that is both modulated by the pump laser mechanical modulation frequency and that has angular momentum orientation affected by the circularly polarized pump laser. The additional spectral line assignment analysis will yield information on the upper states both in the $A^1\Sigma_u^+ \sim b^3\Pi_u$

complex and also in excited states by vertical cascade type polarization double resonance at around 26,000cm^{-1}.

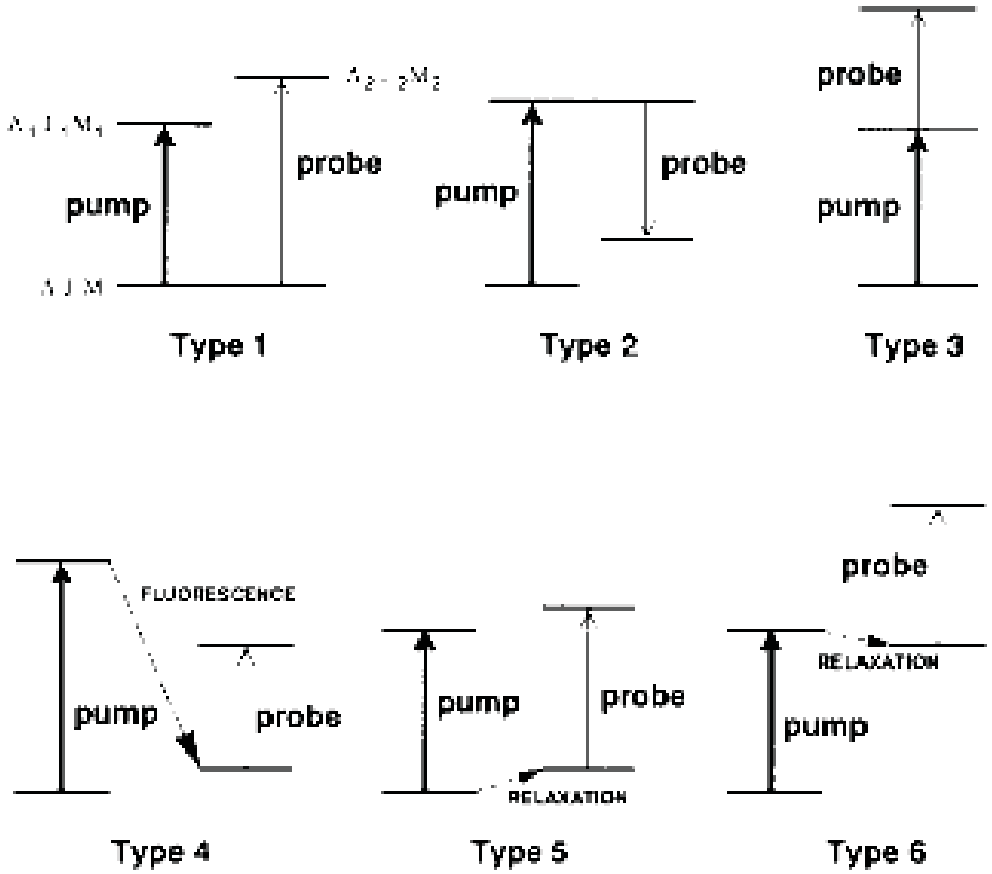

Figure 5.3 The six types of probe signals in OODR polarization spectroscopy[17].

5.2.2 The Cs_2 Polarization Spectra

Due to much weaker Franck – Condon Factors between the ground state $X^1\Sigma_g^+$ and the $A^1\Sigma_u^+ \sim b^3\Pi_u$ perturbed complex of states, fewer collisional satellite lines were observed in our Cs_2 experiment. The difference of the rotational quantum number of the collisional satellite lines from that of the main R,P lines in the Cs_2 spectra is much smaller than for the Rb_2 spectra. Figure 5.4 shows part of the Cs_2 polarization spectra. In this scan, the $C^1\Pi_u(7,73) \leftarrow X^1\Sigma_g^+(6,74)$ transition and the $C^1\Pi_u(7,72) \leftarrow X^1\Sigma_g^+(6,73)$ transition were pumped simultaneously because the $C^1\Pi_u$ rotational energy level structure of Cs_2 is very dense. This made it very difficult to isolate pump laser frequencies that would excite only one rovibronic transition. However, since the polarization spectra were about hundred times weaker than in the $^{85}Rb_2$ case, it was necessary to isolate multiple pump transitions to get a broader range of rotational level data for the region that had never been observed previously, leading to a gap in the global deperturbation analysis of the spin-orbit interaction of the Cs_2 A~B complex of states.

The term values of the Cs_2 polarization data run from 11118 cm^{-1} to 11549 cm^{-1}. Figure 5.5 shows the observed data from our Cs_2 polarization experiment (see also Fig. 6.1). The data partially fill in the energy gap of the $A^1\Sigma_u^+ \sim b^3\Pi_u$ complex of states of Cs_2 that had been inaccessible to other research groups because of very poor Franck-condon factors between the rovibrational levels within the ground state thermal population and this energy region in the $A^1\Sigma_u^+ \sim b^3\Pi_u$ complex of states. The very high signal to noise ratio of polarization spectroscopy made it possible to observe energy levels in this gap region.

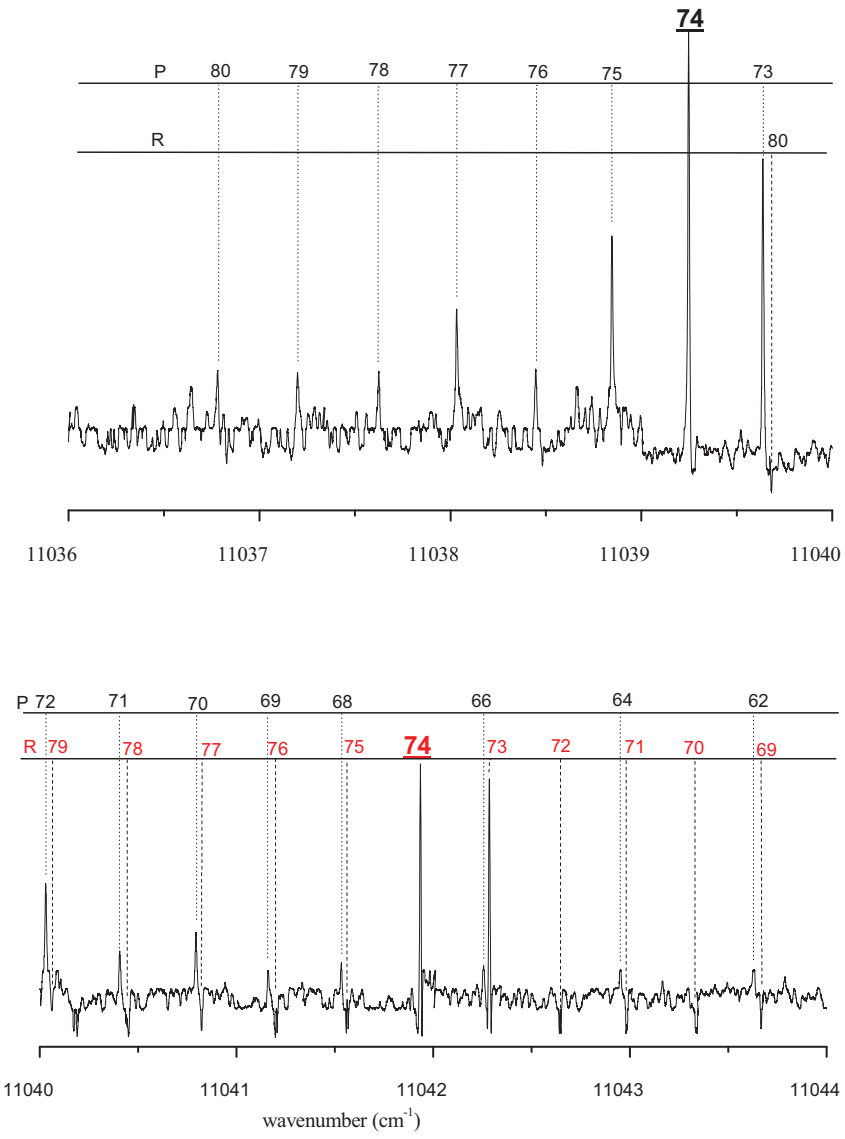

Figure 5.4 Cs_2 polarization spectroscopy signals. For this scan, both the $C^1\Pi_u(7,73) \leftarrow X^1\Sigma_g^+(6,74)$ transition and the $C^1\Pi_u(7,72) \leftarrow X^1\Sigma_g^+(6,73)$ transition are pumped simultaneously.

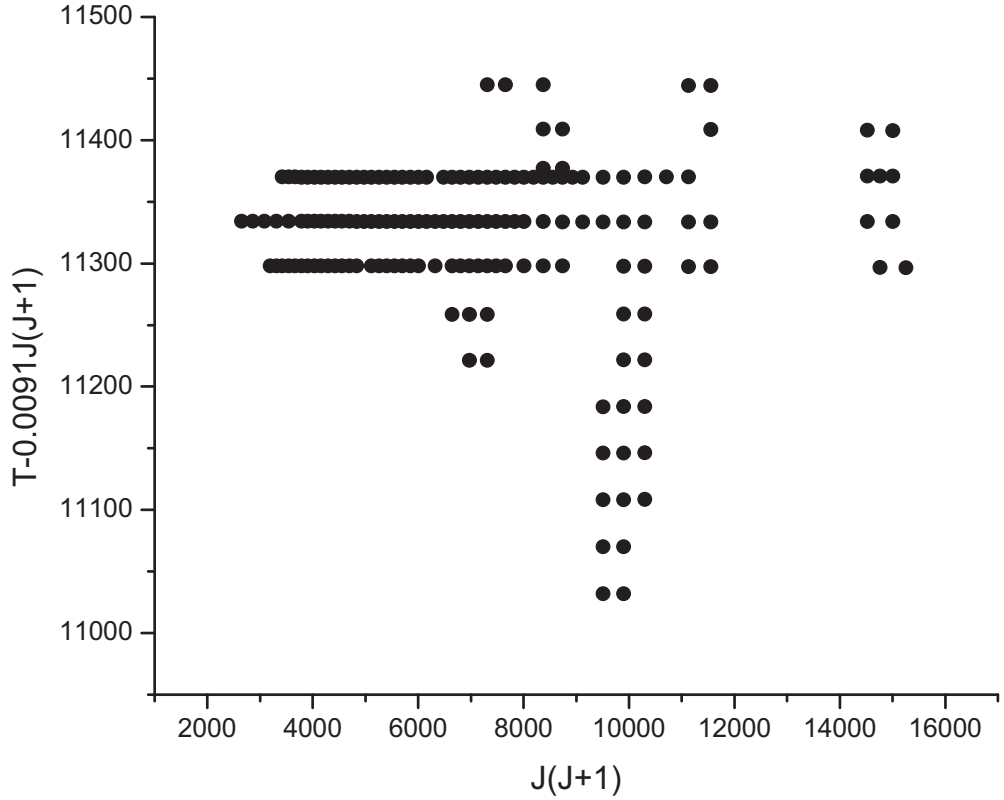

Figure 5.5 Observed energies of the Cs_2 A/b states. The rotational energy 0.0091*J(J+1)* cm^{-1} has been subtracted from the energies so as to approximately remove the rotational energy. The data partially fill the energy gap that was inaccessible to other groups.

5.2.3 Difference in the Collisional Satellite Spectra of Rb_2 and Cs_2

While collisional lines with significant difference in the rotational quantum number from the main lines up to ΔJ = -58 (and up to ΔJ = +16 for higher lying rotational levels) were identified in our Rb_2 polarization experiment. In our Cs_2 polarization experiment, the maximum number of collisional satellite lines corresponded to ΔJ = -12 (and up to ΔJ = 6 for higher lying rotational levels) and the signal to noise ratio was significantly lower than in the Rb_2 spectra despite all of our efforts to optimize it for the Cs_2 experiment. As can be seen from the comparison of the Franck – Condon factors for transitions of interest in Rb_2 and Cs_2, they play an important role in determining the intensities of the transitions. Figure 5.6 (a) shows the logarithm of the Franck- Condon factors for transitions between the v" =4 and v" = 5 ground states to A states of Cs_2, and Figure 5.6 (b) shows the logarithm of the Franck- Condon factors for transitions between the v" = 0 ground state to A states of Rb_2 calculated by Dr. T. Bergeman. The Franck- Condon factors for the Rb_2 are 100 times larger than for Cs_2.

Thermal Distribution

Another reason for the significant ΔJ difference between the Rb_2 polarization spectra and the Cs_2 polarization spectra is the thermal distribution of the ground state molecules. According to the Maxwell – Boltzmann distribution law, the number of molecules in each vibrational energy level is proportional to

$$e^{-E/kT} = e^{-G_0(v)/0.6952T} \tag{5.1}$$

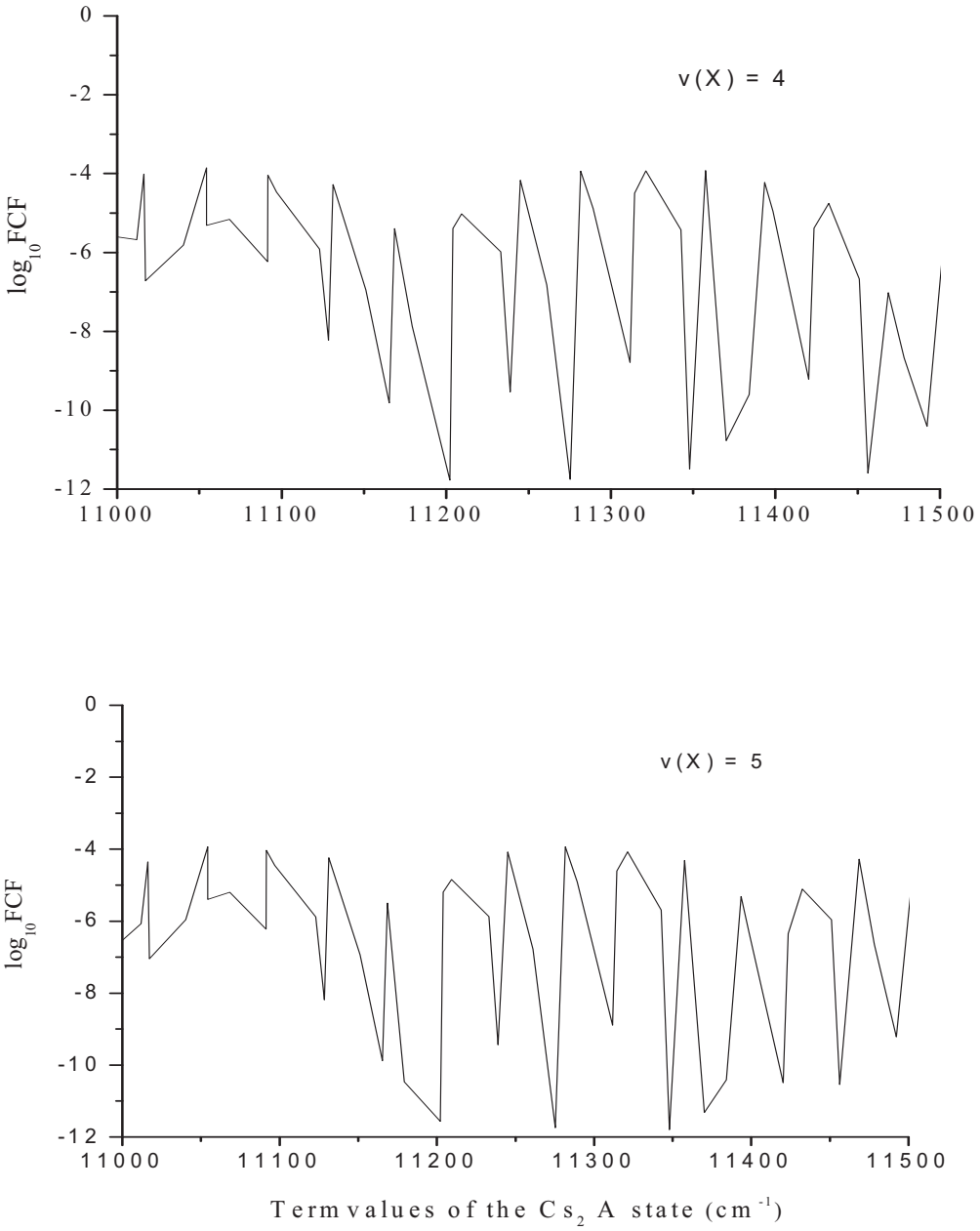
v(X) = 4
v(X) = 5
log10 FCF
0
-2
-4
-6
-8
-10
-12
11000
11100
11200
11300
11400
11500
Term values of the Cs2 A state (cm-1)

(a)

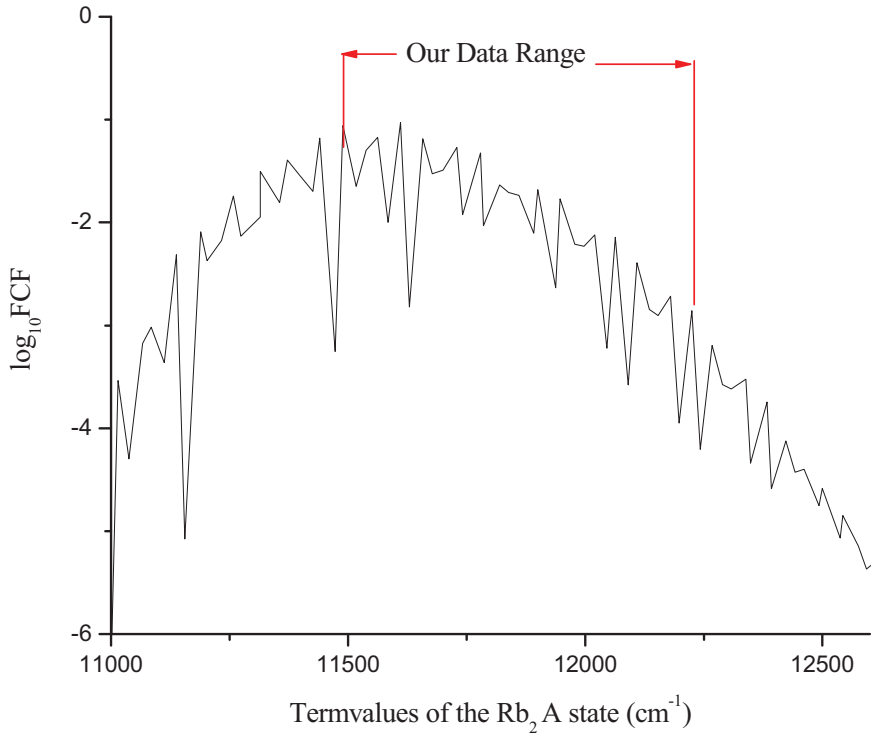

(b)

Figure 5.6 (a) Logarithm of the Franck- Condon factors for transitions between v" =4 and v" = 5 ground states to A states of Cs_2. (b) Logarithm of the Franck- Condon factors for transitions between v" = 0 ground state to A states of Rb_2.

where k is Boltzmann's constant and T is the sample temperature of 550K for our Cs_2 polarization experiment. Figure 5.6 shows the thermal population distribution of the vibrational levels of Cs_2 ground states. From this figure we see that the higher the vibrational level of the ground state, the lower population of the molecules.

5.3 Identifaction of the Rotational Quantum Numbers in the Polarization Spectra

5.3.1 Application of the Collision - Induced Lines to Mitigate the Difficulty in Identifying Isolated Pump Laser Transitions

As can be seen from Figure 5.3, we detected much weaker satellite lines due to collision-induced orientation transfer with ΔJ up to 12 in our Cs_2 polarization experiment. Due to the density of rovibrational lines in the electronic states of Cs_2 it was difficult to separate pump laser transitions from unrelated pump transitions. To mitigate this difficulty the wavelength of the probe laser was tuned to a satellite line and after that the pump laser was scanned around the original pump transition. A strong Doppler-free signal could be detected when the two lasers shared the same ground state. Then the pump laser was tuned to this newly labeled pump transition and the probe laser was scanned to get the strong P, R lines as well as new satellite lines.

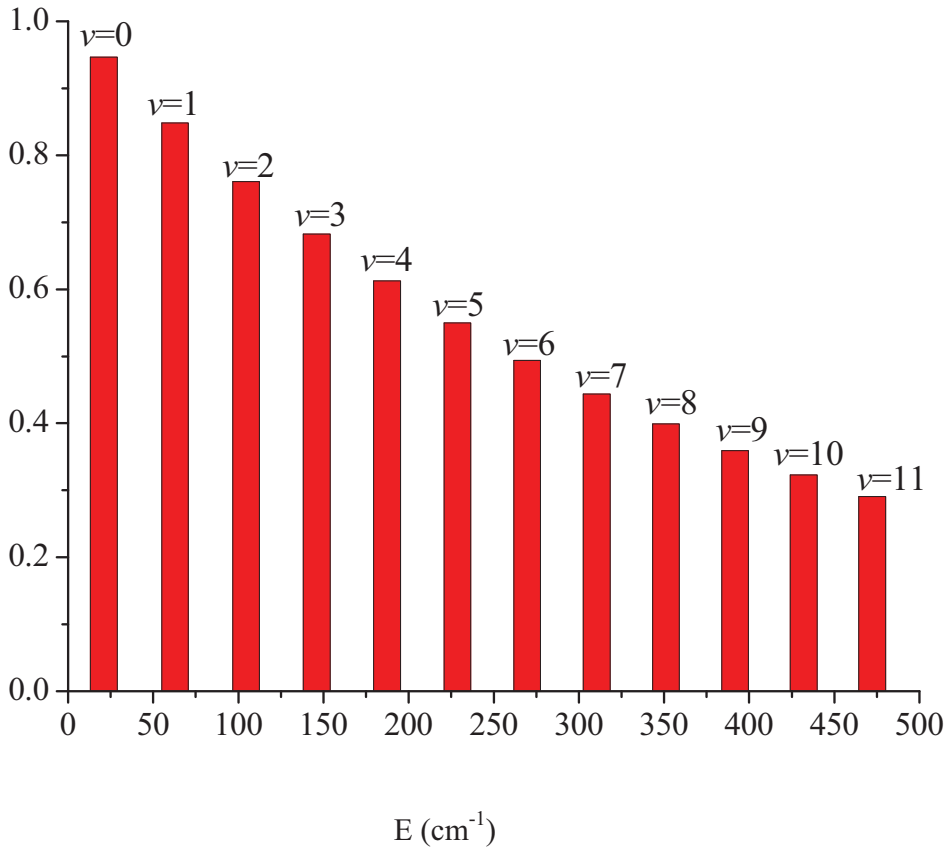

Figure 5.7 Thermal population distribution of the vibrational levels of Cs_2 $X^1\Sigma_g^+$ ground state, given by $e^{-E/kT}$ for different v with T = 550K.

5.3.2 Advantages of This Technique

Compared to using a monochromator and resolved fluorescence spectroscopy to identify the pump laser transition quantum numbers, using the collisional satellite lines to isolate pump laser frequencies was much less time consuming. Since the rovibronic energy level structure of Cs_2 electronic states is very dense, it is difficult to resolve the $C^1\Pi_u \rightarrow X^1\Sigma_g^+$ fluorescence. Small scan steps and long integration time were necessary to obtain reliable fluorescence data scan using the SPEX 1404 double monochromator to confirm the pump transition rotational quantum number for the ground state, up to hours of time per scan. Ordinarily the fluorescence based assignment of the upper level rotational quantum number relies on accurate knowledge of the ground state rovibrational energy levels and their energy separations. The experimentally observed R, P pair separation is simply compared with the second combination differences $\Delta_2F(J'')= F(J''+1) - F(J''-1)$ where F stands for the termvalue. Using this new technique, we could find a new pump transition in a few minutes.

This method is also more accurate than the monochromator scan, which has lower resolution. Another advantage of this method is that it greatly extended the range of the rotational quantum numbers that we could obtain from the experiment.

5.4 Conclusion

We obtained high resolution spectra of the $A^1\Sigma_u^+ / b^3\Pi_u \leftarrow X^1\Sigma_g^+$ transitions of the Rb_2 and Cs_2 molecules by the technique of Doppler-free optical–optical double resonance polarization spectroscopy. The accurate wavenumbers of the direct lines and the satellite

lines due to collisional orientation transfer were recorded. The spin-orbit perturbations between the $A^1\Sigma_u^+$ and $b^3\Pi_u$ states complicated the spectra. The theoretical analysis of the experimental data will be discussed in the next chapter.

References:

1. Bergmann, K. and Demtroder, W., J. Phys. B **5**, 1386 (1972).
2. Bergmann, K. and Demtroder, W., J. Phys. B **5**, 2098 (1972).
3. Bergmann, K. and Dermtroder, W., Z. Phys. **243**, 1 (1971).
4. Ottinger, C., Velasco, R., and Zare, R. N., J. Chem. Phys. **52**, 1636 (1970).
5. Ottinger, C. and Poppe, D., Chem. Phys.Lett. **8**, 513 (1971).
6. Antonova, S., Urbanski, K., Lyyra, A. M., Spano, F. C., and Li, L., Chem. Phys. Lett. **267**, 158 (1997).
7. Teets, R., Feinberg, R., Hansch, T. W., and Schawlow, A. L., Phys. Rev. Lett. **37** (11), 683 (1976).
8. Rowe, M. D., and McCaffery, A. J.,Chem. Phys. **43**, 35 (1979).
9. Ottinger, C. and Schroder, M., J.Phys.B **13**, 4163 (1980).
10. Derouard, J., Chem. Phys. **84**, 181 (1984).
11. Smith, T. A. B. N., Karp, A. W., and Pritchard, D. E., J. Appl. Phys. **74**, 3324 (1981).
12. McCaffery, A. J., Reid, K. L., and Whitaker, B. J., Phys. Rev. Lett. **61**, 2085 (1988).
13. McCaffery, A. J., Richardson, J. P., Wilson, R. J., and Wynn, M. J., J.Phys.B **26**, 705 (1993).
14. Reid, K. L. and McCaffery, A. J., J.Chem.Phys. **96**, 5789 (1993).
15. Collins, T. L. D., McCaffery, A. J., Richardson, J. P., and Wynn, M. J., J.Chem.Phys. **102**, 4419 (1995).

16. Diemer, U., Duchowicz, R., Ertel, M., Mehdizadeh, E., and Demtroder, W., Chem. Phys. Lett. **164**, 419 (1989).

17. Okada, N., Kasahara, S., Ebi, T., Baba, M., and Kato, H., J. Chem. Phys. **105**, 3458 (1996).

18. Kato, H., Kobayashi, T., Chosa, M., Nakahori, T., Lida, T., Kasahara, S., and Baba, M., J. Chem. Phys. **94**, 2600 (1991).

19. Kasahara, S., Baba, M., and Kato, H., J. Chem. Phys. **94**, 7713 (1991).

20. Kasahara, S., Fujifara, C., Okada, N., Kato, H., and Baba, M., J. Chem. Phys. **111**, 8857 (1999).

21. Wolfe, C., Ashman, S., Bai, J., Beser, B., Ahmed, E. H., Lyyra, A. M., and Huennekens, J., J. Chem. Phys. **134**, 174301 (2011).

22. Salami, H., Bergeman, T., Beser, B., Bai, J., Ahmed, E. H., Kotochigova, S., Lyyra, A. M., Huennekens, J., Lisdat, C., Stolyarov, A. V., Dulieu, O., Crozet, P., and Ross, A. J., Phys. Rev. A **80**, 022515 (2009).

CHAPTER 6

THEORETICAL ANALYSIS OF THE $A^1\Sigma_u^+$ AND $b^3\Pi_u$ PERTURBED STATES

6.1 $A^1\Sigma_u^+ / b^3\Pi_u$ States of Rb_2 and Cs_2 mixed by the Spin-Orbit Interaction

The spin-orbit interaction couples the spin and orbital angular momenta of the electrons [1]. Spin-orbit splitting and coupling terms have been studied experimentally and theoretically for many years [2-4]. The atomic spin-orbit coupling strength (the fine structure splitting) of the first excited p state ($^2P_{3/2}$ -$^2P_{1/2}$) of the alkali atoms is 0.34cm^{-1} for Li (2p) , 17.2cm^{-1} for Na (3p), 57.7cm^{-1} for K(4p), 237.6cm^{-1} for Rb(5p), and 554.0cm^{-1} for Cs(6p). The first excited molecular electronic states in the $A^1\Sigma_u^+ \sim b^3\Pi_u$ complex of states of Rb_2 and Cs_2 are highly perturbed because of the strong spin – orbit interaction for heavier atoms and molecules.

There has been many global deperturbation studies of the spin-orbit interaction of the $A^1\Sigma_u^+ / b^3\Pi_u$ electronic states of the alkali diatomic molecules Li_2 [5-8], Na_2 [9-13], K_2 [14-18] and Rb_2 [19,20]. The goal of this research was to determine the singlet~triplet character of each rovibrational level and their energies to identify gateway levels for Perturbation-Faciliatated Optical Resonance (PFOODR) excitation to the higher lying

excited electronic states, which could not be reached from the singlet ground state $X^1\Sigma_g^+$ [21]. Traditionally band-by-band methods [13] were applied to analyze the $A^1\Sigma_u^+ / b^3\Pi_u$ electronic states of the lighter alkali molecules. The spin-orbit coupling matrix elements for many vibrational levels could be generated. However, for the heavier alkali dimers a more systematic global deperturbation process is necessary since the spin-orbit interaction is much stronger and perturbations are no longer local. The spin-orbit coupling matrix elements are even larger than the vibrational energy intervals in the heavier alkali dimers.

Such global deperturbation analyses, resulting in complete characterization of the rovibrational level structure, including the singlet~triplet character of the $A^1\Sigma_u^+ \sim b^3\Pi_u$ states and the internuclear distance dependent spin-orbit functions, have been reported for Na_2 [9,13], K_2 [15], Rb_2 [20] and Cs_2 [22-24]. The spin-orbit splitting for the NaK $A^1\Sigma_u^+ / b^3\Pi_u$ state has been studied by Ross *et al.* [25] and Sun *et al*. [26]. These experimental observations were later followed by *ab initio* calculations [27,28] of the potential energy functions and spin-orbit functions for the Cs_2 $A^1\Sigma_u^+ / b^3\Pi_u$ electronic states, performed at Moscow state University and Temple University. This Thesis deals with the acquisition and analysis of the data for the global deperturbation of the spin-orbit interaction for the Rb_2 and Cs_2 A~b complexes. We now describe the theoretical analysis used in the global deperturbation process.

6.2 Discrete Variable Representation (DVR) Method

6.2.1 Introduction to DVR Method

Laser spectroscopic techniques and traditional methods of analysis have been applied to analyze the spectra of the $A^1\Sigma_u^+$ and $b^3\Pi_u$ states of Li_2, Na_2, K_2 and NaK. Traditionally the transition frequencies obtained from the experiment are fitted to an analytical expression such as the Dunham expansion [29]. The local perturbations can be isolated in such an analysis, since they appear with larger residuals in the fit. The unperturbed levels can then be used in a new Dunham fit to produce new molecular constants, and from those by using the semi- classical Rydberg – Klein – Rees (RKR) [30] method, an RKR potential energy curve can be calculated.

The traditional methods cannot, however, be used to analyze the strong spin – orbit coupling between the two A~b complex of states of the heavier alkali – metal dimers. The discrete variable representation (DVR), a numerical method (also known as the Fourier Grid Hamiltonian (FGH) method), was applied to study the lowest excited states, the $A^1\Sigma$ state and the $b^3\Pi$ state, of the heavier alkali – metal dimers such as Na_2, Rb_2 and RbCs.

The DVR method has proved to be a useful tool for solving problems in quantum mechanics numerically [31,32]. J. C. Light and coworkers have compared the DVR method and other representations [33]. The DVR method has been applied to a number of systems. M. R. Manaa *et. Al* [15] extracted accurate Dunham coefficients and potential curves for the perturbed A/b states of K_2 by using the DVR method together with the *ab initio* diagonal and off-diagonal spin-orbit functions. The Fourier grid representation is

the simplest DVR. Based on the eigenfunctions of a particle in a box, it can be used to study nonadiabatic effects in the dynamics of alkali-metal dimers [34].

6.2.2 Theory of DVR method

In the DVR method the internuclear distance R of the diatomic molecule in interval (R_0, R_N) is restricted to the uniformly spaced N-1 grid points:

$$R_i = R_0 + (R_N - R_0)i / N, i = 1,\ldots, N-1 \tag{6.1}$$

The matrix element for the potential operators is [35]:

$$V_{ij} = V(R_i)\delta_{ij}, \tag{6.2}$$

The DVR kinetic energy is written as:

$$H_{ij}^{k} = -\frac{\hbar^2}{2m}\Delta x\sum_{n=1}^{N-1}\phi_n(x_i)\phi_n^{''}(x_j) \tag{6.3}$$

where $\Delta x = (R_N - R_0)/N$ is the spacing of the grid and ϕ_n is the wavefunction, which has the form:

$$\phi_n(x) = \left(\frac{2}{R_N - R_0}\right)^{1/2} \sin\left[\frac{n\pi(x - R_0)}{R_N - R_0}\right], n = 1, \ldots, N-1 \tag{6.4}$$

Since $\phi_n(x_0 = R_0) = \phi_n(x_N = R_N) = 0$ for particle-in-a-box eigenfunctions, only N-1 functions and N-1 points are considered. The matrix elements for the kinetic energy operator $H^k = -\frac{\hbar^2}{2\mu}\frac{d^2}{dR^2}$ can be written as:

$$H_{ij}^k = -\frac{\hbar^2}{4\mu}\frac{\pi^2(-1)^{i-j}}{(R_0 - R_N)^2}\left\{\frac{1}{\sin^2[\pi(i-j)/2N]} - \frac{1}{\sin^2[\pi(i+j)/2N]}\right\} \tag{6.5}$$

when $i \neq j$ and

$$H_{ij}^k = -\frac{\hbar^2}{4\mu}\frac{\pi^2}{(R_0 - R_N)^2}\left\{\frac{2N^2+1}{3} - \frac{1}{\sin^2(\pi i/N)}\right\} \tag{6.6}$$

when $i = j$ .The eigenfunction and eigenvalue of each electronic state can be obtained by diagonalizing the total DVR Hamiltonian matrix. Spin – orbit coupling is important to the study of the $A^1\Sigma_\mu$ and $b^3\Pi_\mu$ perturbed states of alkali dimers because it leads to the singlet – triplet mixing and thus the fine structure splitting.

6.3 Analysis of the Experimental Data

6.3.1 Molecular Hamiltonian

The molecular Hamiltonian which includes the Born – Oppenheim potentials H_{BO}, radial kinetic energy H_K, nuclear rotation H_{rot}, and spin – orbit interaction H_{SO}, can be expressed as [1]:

$$H = H_{BO} + H_K + H_{SO} + H_{rot} \tag{6.7}$$

Here $H_K = -\left(\frac{\hbar^2}{2u}\right)\frac{d^2}{dR^2}$ is the kinetic energy operator, where u is the reduced mass of the system and R is the distance between the two nuclei.

In Cs_2 second – order spin – orbit (SO2) effects are significant because Cs_2 is a relatively heavy diatomic molecule. From [1], we see that the matrix elements of $H_{BO} + H_{SO} + H_{rot} + H_{SO2}$ are:

$$\left\langle {}^1\Sigma_u^+ \middle| H \middle| {}^1\Sigma_u^+ \right\rangle = U_A + (x+2)B + U_A^{so2}$$

$$\left\langle {}^3\Pi_{0u}^+ \middle| H \middle| {}^3\Pi_{0u}^+ \right\rangle = U_{b0}^+ + (x+2)B + U_{b0e}^{so2}$$

$$\left\langle {}^3\Pi_{0u}^- \middle| H \middle| {}^3\Pi_{0u}^- \right\rangle = U_{b0}^- + (x+2)B + U_{b0f}^{so2}$$

$$\left\langle {}^3\Pi_{1u} \middle| H \middle| {}^3\Pi_{1u} \right\rangle = U_{b0}^+ + (x+2)B + \xi_{b10}^{so}$$

$$\left\langle {}^3\Pi_{2u} \middle| H \middle| {}^3\Pi_{2u} \right\rangle = U_{b0}^+ + (x-2)B + \xi_{b10}^{so} + \xi_{b21}^{so}$$

$$\left\langle {}^1\Sigma_u^+ \middle| H \middle| {}^3\Pi_{0u}^+ \right\rangle = -\sqrt{2}\xi_{Ab0}^{so}$$

$$\left\langle {}^3\Pi_{0u} \middle| H \middle| {}^3\Pi_{1u} \right\rangle = -\sqrt{2x}B$$

$$\left\langle {}^3\Pi_{1u}\middle|H\middle|{}^3\Pi_{2u}\right\rangle = -\sqrt{2(x-2)}B$$

$$\left\langle {}^1\Sigma_u^+\middle|H\middle|{}^3\Pi_{1u}\right\rangle = -\sqrt{2x}B\eta \tag{6.8}$$

where u is the reduced mass, $x = J(J+1)$, $B \equiv \frac{\hbar^2}{2uR^2}$ and $H^T = H$. Here H^T is the transpose of H. The potentials U_A and $U_{b0}^{\pm}$, $B \equiv \frac{\hbar^2}{2uR^2}$, as well the off diagonal spin-orbit function ξ_{Ab0}^{SO} and diagonal spin-obit function ξ_{b10}^{SO} , are functions of the internuclear distance R. ξ_{b10}^{SO} is the $\Omega = 1 - 0^+$ interval of the b state and ξ_{b21}^{SO} is the $\Omega = 2 - 1$ interval. Both of the two functions include the SO2 effect implicitly. As discussed in [36], the parameter η arises from second-order spin-orbit and electronic-rotational effects.

The SO2 functions can be expressed as [24]:

$$U_A^{SO2}(R) = \frac{2\left|\xi_{A-j}^{SO}\right|^2}{U_A - U_j};\ j \in (2)^3\Pi_u,$$

$$U_{b0e}^{SO2}(R) = \frac{2\left|\xi_{b0-j}^{SO}\right|^2}{U_{b0}^+ - U_j};\ j \in (2)^1\Sigma_u^+,$$

$$U_{b0f}^{SO2}(R) = \sum_j \frac{2\left|\xi_{b0-j}^{SO}\right|^2}{U_{b0}^- - U_j};\ j \in (1-3)^1\Sigma_u^+,$$

$$U_{b1e}^{SO2}(R) = \sum_j \frac{\left|\xi_{b1-j}^{SO}\right|^2}{U_{b1}^+ - U_j};\ j \in (1-3)^3\Sigma_u^+, (1-2)^1\Pi_u. \tag{6.9}$$

U_{b0f}^{SO2} is large and positive for small R and becomes negative for large R. That the $a^3\Sigma_u^+$ potential lies below the $b^3\Pi_{0u}^-$ potential shifts the $b^3\Pi_{0u}^-$ energy upward. The SO2 shift

is negative for large R because the $b^3\Pi_{0u}^-$ potential approaches various ungerade potentials from below in this region.

The difference between the eigenvalues calculated from the fitted potentials with and without the off-diagonal ξ_{Abo}^{SO} coupling function is the theoretical value of the SO contribution. It comes from the strong spin-orbit coupling between the triplet $b^3\Pi_{0u}$ state and the nearby singlet $A^1\Sigma_u^+$ state.

The step size $\Delta R_{\min} = (a-b)/N$ should be smaller than the local de Broglie wavelength, which is small near the deepest part of the potential curve and becomes much larger for larger internuclear separations. The dimension of the matrix is unmanageable if we use the same $\Delta R_{\min}$ in the numerical calculations for small and large R. Transformation is performed to reduce the matrix dimensions. [35].

The nonlinear coordinate transformation which leads to the smallest matrix dimension has the form:

$$y = u(R) = \int_R^\infty \frac{dx}{R_0}\sqrt{\left(\frac{R_0}{x+R_s}\right)^n} = -\frac{1}{(n/2)-1}\left(\frac{R_0}{R+R_s}\right)^{n/2-1} \tag{6.10}$$

where n characterizes the long range tail of the potentials. R_0 and R_s are free parameters. The transformation ensures that, as the local de Broglie wavelength increases at large

internuclear separations, the step size also increases. The kinetic energy operator is transformed into the form:

$$H^K = -\frac{\hbar^2}{2u}\frac{d^2}{dR^2} = -\frac{\hbar^2}{2u}\left\{ p(y)\frac{d^2}{dy^2} + q(y)\frac{d}{dy} \right\} \tag{6.11}$$

with

$$p(y) = \frac{1}{[U'(y)]^2} \quad \text{and} \qquad q(y) = -\frac{U''(y)}{[U'(y)]^3} \tag{6.12}$$

where U(y) is the inverse transformation of $y = u(R)$. The transformed wavefunction $\Phi(y)$ is defined by:

$$\Psi(R) = \frac{\Phi(y)}{\sqrt{U'(y)}} \tag{6.13}$$

The new Schrodinger equation has the form:

$$\left[\frac{\hbar^2}{2u}\left\{ -\frac{1}{U'(y)}\frac{d^2}{dy^2}\frac{1}{U'(y)} - \frac{1}{2}\frac{U^{(3)}(y)}{[U'(y)]^3} + \frac{3}{4}\frac{[U''(y)]^2}{[U'(y)]^4} \right\} + V(U(y)) \right]\Phi(y) = E\Phi(y) \tag{6.14}$$

From this equation we see that the first term on the left hand side of the equation serves as kinetic energy operator and the remaining terms on the left hand side corresponded to

spin-independent potentials. The eigenvalues and eigenfunctions can be obtained by the diagonalization of the DVR matrix for each *J*.

6.3.2 Analytic Potential Functions

An Expanded Morse Oscillator (EMO) function [37-39] can be used to analytically represent the empirical potential energy curves (PECs) of the perturbed $A^1\Sigma_u^+ \sim b^3\Pi_u$ electronic states converging to the appropriate dissociation limit:

$$U(R) = T_e + D_e\left[1 - e^{-a(R-R_e)}\right]^2$$

$$\alpha(R) = \sum_{i=0}^{N} a_i \left(\frac{R^p - R_{ref}^P}{R^p + R_{ref}^P}\right)^i \tag{6.15}$$

where R is in Å, $P=3$, R_{ref} =5.0 Å, T_e and D_e are in cm^{-1}, and the other parameters are dimensionless.

The matrix elements of the spin-orbit operator are given by:

$$H_{SO} = \frac{\alpha^2}{2}\sum_N \sum_i \frac{Z_N}{R_{iN}^3} \boldsymbol{l}_i \cdot \boldsymbol{s}_i - \frac{\alpha^2}{2}\sum_{i\neq j}\frac{1}{r_{ij}^3}\left[R_{ij}\times \boldsymbol{p}_i\right]\cdot\left(\boldsymbol{s}_i + 2\boldsymbol{s}_j\right), \tag{6.16}$$

where α is the fine structure constant , $\boldsymbol{s}_i$ is the spin of electron i, R_{iN} is the separation between the ith electron and charge Z_N, $\boldsymbol{l}_i$ is the electron orbital angular momentum relative to the nucleus, $\boldsymbol{R}_{ij}$ is the separation between electron i and j, and p_i is the

momentum of electron *i*. The first term of this equation is a one electron operator that describes spin-orbit interactions between one nucleus and one electron. The second term is a two-electron operator that describes the spin-orbit interactions between electrons.

6.4 Fit of the Experimental Data

6.4.1 Fitting Procedures

The dimension of the DVR Hamiltonian for a single electronic state equals the square of the number of *R* mesh points *N*. For coupled states with *p* different electronic states, the dimension becomes $pN \times pN$. Two channel calculations include only the $^1\Sigma_u^+$ and $^3\Pi_{0u}^+$ electronic states. $^3\Pi_{1u}$ levels are added for the three channel calculations. No spectral lines from the $^3\Pi_{2u}$ levels were observed in the experiments, but the $^3\Pi_{2u}$ components are coupled with the $^3\Pi_{1u}$ levels and thus indirectly affect the $^3\Pi_{0u}^+$ levels.

The components of the $^3\Pi_{2u}$ are also included in the four channel calculations.

6.4.2 Fitting Results

Our Rb_2 experimental data, together with data from Laboratoire Aime Cotton and Lyon University, were used in the global analysis of data on $A^1\Sigma_u^+$ and $b^3\Pi_u$ states of Rb_2 [20]. Parameters of the $A^1\Sigma_u^+$ and $b^3\Pi_u$ states of Rb_2 were generated by applying the DVR method.

Our Cs_2 experimental data, together with the laser-induced fluorescence Fourier transform spectroscopy (LIF FTS) data from Laboratoire Aime Cotton and University of Latvia, Cs_2 cold molecules data from Innsbruck University, and experimental data from Tsinghua University were used in the global analysis of data on $A^1\Sigma_u^+$ and $b^3\Pi_u$ states of Cs_2 by applying the DVR program created by Dr. T. Bergeman from SUNY, Stony Brook. All the data used in this global fit are shown in Figure 6.1. Potential curves and the parameters for the $A^1\Sigma_u^+$ and $b^3\Pi_u$ states were derived from the experimental data. Details of the fit can be found in reference [24].

The term values calculated from the DVR program and the term values obtained from our Cs_2 polarization spectroscopy experimental data are shown in Figure 6.2. For illustration purposes the rotational energy $B_v(J(J+1))= 0.0091*J(J+1)$ has been subtracted from the term values. Here J is the rotational quantum number, and B_v is the rotational constant. Theoretically, the lines with the least slope are from the $A^1\Sigma_u^+$ states because the rotational constant of the A state is smaller. The lines with the steeper slope are from the $b^3\Pi_{1u}$ states. The lines with a slope that is between the $A^1\Sigma_u^+$ states and the $b^3\Pi_{1u}$ are the $b^3\Pi_{0u}$ states**.** From Figure 6.2 it is evident that most of the data we obtained from the Cs_2 polarization spectroscopy experiment belong to the $A^1\Sigma_u^+$ state. The singlet states and the triplet states are highly mixed, and that is why it is impossible to assign vibrational levels to the data.

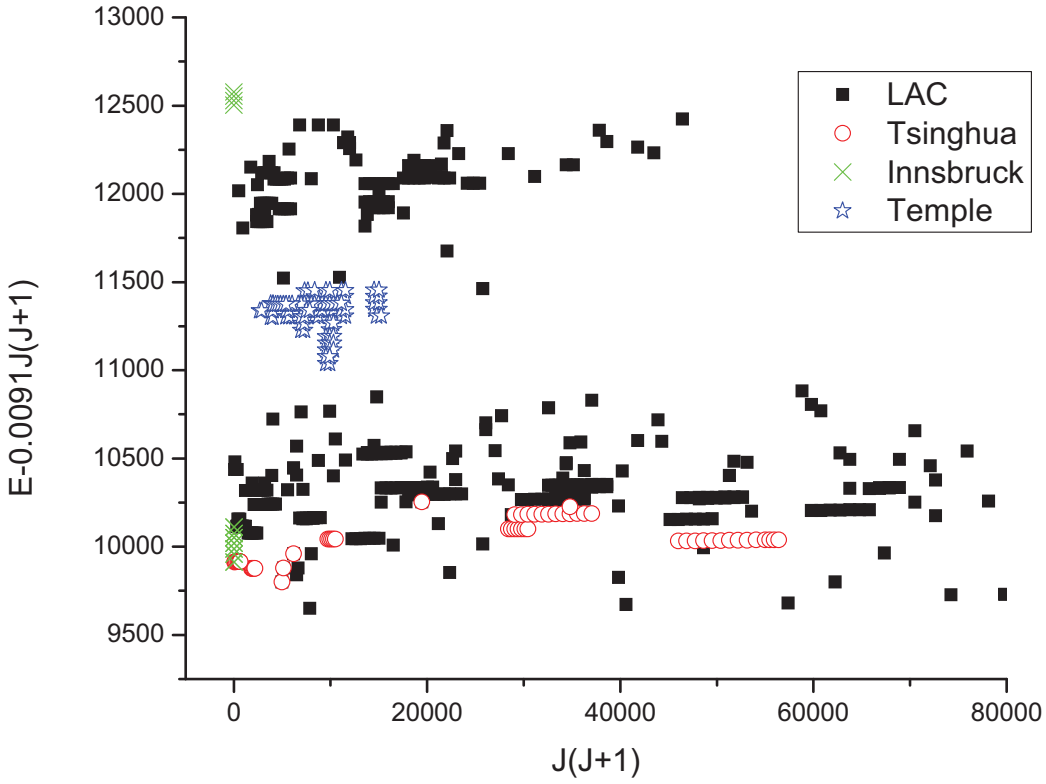

Figure 6.1 Experimental data used in the global analysis of the $A^1\Sigma_u^+$ and $b^3\Pi_u$ perturbed states of Cs_2.

The identified transitions and their rotational and vibrational quantum numbers from our Rb_2 and Cs_2 polarization spectroscopy experiments are listed in the Appendix.

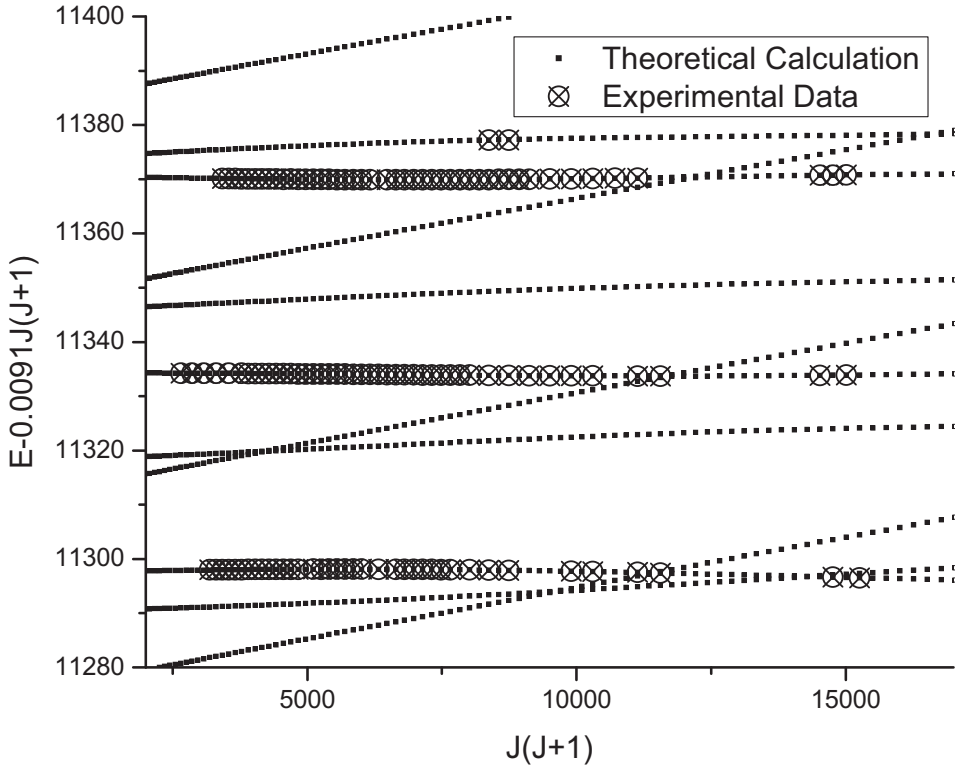

Figure 6. 2 Some of the term values obtained from the Cs_2 polarization spectroscopy experiment. Smaller filled circles are theoretically calculated term values. The circles with crosses in the middle are experimental data.

References:

1. Lefebvre - Brion, H. and Field, R. W., *The Spectra and Dynamics of Diatomic Molecules*, Revised and Enlarged edition ed. (Elsevier Academic Press, 2004).
2. Langhoff, S. R., Sink, M. L., Pritchard, R. H., and Kern, C. W., J. Mol. Spectrosc. **96**, 200 (1982).
3. Richards, W. G., Trivedi, H. P., and Cooper, D. L., *Spin-orbit coupling in molecules*. (Clarendon Press, Oxford, 1981).
4. Hess, B. A., Marian, C. M., and Peyerimhoff, S. D., *Modern Electronic Structure Theory*. (Yarkony, Singapore, 1995).
5. Xie, X. and Field, R. W., Chem. Phys. **99**, 337 (1983).
6. Xie, X. and Field, R. W., J.Mol.Spectrosc. **117**, 228 (1986).
7. Linton, C., Martin, F., Russier, I., Ross, A. J., Crozet, P., Churassy, S., Bacis, R., and J.Mol.Spectrosc. **175**, 340 (1996).
8. Urbanski, K., Antonova, S., Lyyra, A. M., Yiannopoulou, A., and Stwalley, W. C., J.Chem.Phys. **104**, 2813 (1996).
9. Qi, P., Bai, J., Ahmed, E. H., Lyyra, A. M., Kotochigova, S., Ross, A. J., Effantin, C., Zalicki, P., Vigue, J., Chawla, G., Field, R. W., Whang, T. J., Stwalley, W. C., Knockel, H., Tiemann, E., Shang, J., Li, L., and Bergeman, T., J. Chem. Phys. **127**, 044301 (2007).
10. Atkinson, J. B., Becker, J., and Demtroder, W., Chem. Phys. Lett. **87**, 92 (1982).
11. Kato, H., Otani, M., and Baba, M., J. Chem. Phys. **89**, 653 (1988).
12. Lyyra, A. M., Wang, H., Whang, T.-J., Stwalley, W. C., and L.Li, Phys. Rev. Lett. **66**, 2724 (1991).

13. Whang, T.-J., Stwalley, W. C., Li, L., Lyyra, A. M., and J. Chem. Phys. **97**, 7211 (1992).

14. Lisdat, C., Duleiu, O., Knockel, H., and Tiemann, E., Eur. Phys. J. D 17, **319** (2001).

15. Manaa, M. R., Ross, A. J., Martin, F., Crozet, P., Lyyra, A. M., Li, L., Amiot, C., and Bergeman, T., **117**, 11208 (2002).

16. Ross, A. J., Crozet, P., Effantin, C., d'Incan, J., and Barrow, R. F., J. Phys. B **20**, 6225 (1987).

17. Jong, G., Li, L., Whang, T.-J., Lyyra, A. M., Stwalley, W. C., Li, M., and Coxon, J., J. Mol. Spectrosc. **155**, 115 (1992).

18. Kim, J. T., Wang, H., Tsai, C. C., Bahns, J. T., Stwalley, W. C., Jong, G., and Lyyra, A. M., J. Chem. Phys **102**, 6646 (1995).

19. Amiot, C., Dulieu, O., and Verges, J., Phys. Rev. Lett. **83**, 2316 (1999).

20. Salami, H., Bergeman, T., Beser, B., Bai, J., Ahmed, E. H., Kotochigova, S., Lyyra, A. M., Huennekens, J., Lisdat, C., Stolyarov, A. V., Dulieu, O., Crozet, P., and Ross, A. J., Phys. Rev. A **80**, 022515 (2009).

21. Li, L. and Lyyra, A. M., Spectrochimica Acta Part A **55**, 2147 (1999).

22. Kokoouline, V., Dulieu, O., Kosloff, R., and Masnou-Seeuws, F., Phys. Rev. A **62**, 032716 (2000).

23. Kokoouline, V., Dulieu, O., and Masnou-Seeuws, F., Phys. Rev. A (2000).

24. Bai, J., Ahmed, E. H., Beser, B., Guan, Y., Kotochigova, S., Lyyra, A. M., Ashman, S., Wolfe, C. M., Huennekens, J., Xie, F., Li, D., Li, L., Tamanis, M., Ferber, R., Drozdova, A., Pazyuk, E. A., Stolyarov, A. V., Danzl, J. G., Nagerl, H.

C., Bouloufa, N., Duleiu, O., Amiot, C., Salami, H., and Bergeman, T., Phys. Rev. A **83**, 032514 (2011).

25. Ross, A. J., Effantin, C., Incan, J. d., and Barrow, R. F., J. Phys. B. **19**, 1449 (1986).
26. Sun, H. and Huennekens, J., J. Chem. Phys. **97**, 4714 (1992).
27. Manaa, M. R., J. Quant. Chem. **75**, 693 (1999).
28. Ferber, R., Pazyuk, E. A., Stolyarov, A. V., Zaitsevskii, A., Kowalczyk, P., Chen, H., Wang, H., and Stwalley, W. C., J. Chem. Phys. **112**, 5740 (2000).
29. Dunham, J. L., Phys.Rev. **41**, 721 (1932).
30. Rees, A. L. G., Proc.Phys.Soc(London) **59**, 998 (1947).
31. Lill, J. V., Parker, G. A., and Light, J. C., Chem. Phys. Lett. **89**, 483 (1982).
32. Heather, R. W. and Light, J. C., J. Chem. Phys **79**, 147 (1983).
33. Light, J. C., Hamilton, I. P., and Lill, J. V., J. Chem. Phys **82**, 1400 (1985).
34. Dulieu, O. and Julienne, P., J. Chem. Phys. **103**, 60 (1995).
35. Tiesinga, E., Williams, C. J., and Julienne, P. S., Phys. Rev. A **57**, 4257 (1998).
36. Zaharova, J., Taminis, M., Ferber, R., Drozdova, A. N., E.A.Pazyuk, and Stolyarov, A. V., Phys. Rev. A **79**, 012508 (2009).
37. Lee, E. G., Seto, J. Y., Hirao, T., Bernath, P. F., and Roy, R. J. L., J. Mol. Spectrosc. **194**, 197 (1999).
38. LeRoy, R., Huang, Y., and Jary, C., J. Chem. Phys. **125**, 164310 (2006).
39. LeRoy, R. and Henderson, R., Mol. Phys. **105**, 663 (2007).

BIBLIOGRAPHY

Amiot, C., Dulieu, O., and Verges, J., Phys. Rev. Lett. **83**, 2316 (1999).

Anderson, M. H., Ensher, J. R., Matthews, M. R., E.Wieman, C., and Cornell, E. A., Science **269**, 198 (1995).

Antonova, S., Urbanski, K., Lyyra, A. M., Spano, F. C., and Li, L., Chem. Phys. Lett. **267**, 158 (1997).

Atkinson, J. B., Becker, J., and Demtroder, W., Chem. Phys. Lett. **87**, 92 (1982).

Bai, J., Ahmed, E. H., Beser, B., Guan, Y., Kotochigova, S., Lyyra, A. M., Ashman, S., Wolfe, C. M., Huennekens, J., Xie, F., Li, D., Li, L., Tamanis, M., Ferber, R., Drozdova, A., Pazyuk, E. A., Stolyarov, A. V., Danzl, J. G., Nagerl, H. C., Bouloufa, N., Duleiu, O., Amiot, C., Salami, H., and Bergeman, T., Phys. Rev. A **83**, 032514 (2011).

Bergmann, K. and Dermtroder, W., Z. Phys. **243**, 1 (1971).

Bergmann, K. and Demtroder, W., J. Phys. B **5**, 1386 (1972).

Bergmann, K. and Demtroder, W., J. Phys. B **5**, 2098 (1972).

Bernath, P., *Spectra of Atoms and Molecules*. (1995).

Born, M. and Oppenheimer, R., Ann.Phys. **84**, 4571 (1927).

Bradley, C. C., Sackett, C. A., Tollet, J. J., and Hulet, R. G., Phys.Rev.Lett. **75**, 1687 (1995).

Brown, J. and Carrington, A., *Rotational Spectroscopy of Diatomic Molecules*. (Cambridge University Press, 2003).

Bunker, P. R. and Jensen, P., *Molecular Symmetry and Spectroscopy*, 2nd ed. (NRC Research Press, Ottawa, 1998).

Chen, H., Li, L., Lazarov, G., Wang, X., Lyyra, A. M., Huennekens, J., and Field, R. W., J. of Mol. Spec. **196**, 197 (1999).

Collins, T. L. D., McCaffery, A. J., Richardson, J. P., and Wynn, M. J., J.Chem.Phys. **102**, 4419 (1995).

Davis, K. B., Mewes, M.-O., Andrews, M. R., Druten, N. J. V., Drufree, D. S., Kum, D. M., and Ketterle, W., Phys.Rev.Lett. **75**, 3969 (1995).

Demtroder, W., *Laser Spectroscopy, Basic Concepts and Instrumentation*, Second Enlarged ed. (Springer-Verlag, Berlin, 1996).

Derouard, J., Chem. Phys. **84**, 181 (1984).

Diemer, U., Duchowicz, R., Ertel, M., Mehdizadeh, E., and Demtroder, W., Chem. Phys. Lett. **164**, 419 (1989).

Dulieu, O. and Julienne, P., J. Chem. Phys. **103**, 60 (1995).

Dunham, J. L., Phys.Rev. **41**, 721 (1932).

Ferber, R., Pazyuk, E. A., Stolyarov, A. V., Zaitsevskii, A., Kowalczyk, P., Chen, H., Wang, H., and Stwalley, W. C., J. Chem. Phys. **112**, 5740 (2000).

Gerstenkorn, S. and Luc, P., *The Aim´e Cotton Iodine Atlas*, Editions du CNRS ed. (Paris, 1978).

Gerstenkorn, S. and Luc, P., Rev. Phys. Appl. **14**, 791 (1979).

Heather, R. W. and Light, J. C., J. Chem. Phys **79**, 147 (1983).

Herzberg, G., *Molecular Spectra and Molecular Structure*. (1950).

Hess, B. A., Marian, C. M., and Peyerimhoff, S. D., *Modern Electronic Structure Theory*. (Yarkony, Singapore, 1995).

Hougen, J. T., *The Calculation of Rotational Energy Levels and Rotational Line Intensities In Diatomic Molecules*. (US government Printing Office, NBS Monograph, Washington, D.C., 1970).

Jong, G., Li, L., Whang, T.-J., Lyyra, A. M., Stwalley, W. C., Li, M., and Coxon, J., J. Mol. Spectrosc. **155**, 115 (1992).

Kasahara, S., Baba, M., and Kato, H., J. Chem. Phys. **94**, 7713 (1991).

Kasahara, S., Hasui, Y., Otsuka, K., Baba, M., Demtroder, W., and Kato, H., J. Chem. Phys. **106**, 4869 (1997).

Kasahara, S., Fujifara, C., Okada, N., Kato, H., and Baba, M., J. Chem. Phys. **111**, 8857 (1999).

Kato, H., Otani, M., and Baba, M., J. Chem. Phys. **89**, 653 (1988).

Kato, H., Kobayashi, T., Chosa, M., Nakahori, T., Lida, T., Kasahara, S., and Baba, M., J. Chem. Phys. **94**, 2600 (1991).

Kayama, K. and Baird, J. C., J.Chem.Phys. **46**, 2604 (1967).

Kim, J. T., Wang, H., Tsai, C. C., Bahns, J. T., Stwalley, W. C., Jong, G., and Lyyra, A. M., J. Chem. Phys **102**, 6646 (1995).

Klein, O., Z. Physik **76**, 226 (1932).

Kokoouline, V., Dulieu, O., Kosloff, R., and Masnou-Seeuws, F., Phys. Rev. A **62**, 032716 (2000).

Kokoouline, V., Dulieu, O., and Masnou-Seeuws, F., Phys. Rev. A (2000).

Langhoff, S. R., Sink, M. L., Pritchard, R. H., and Kern, C. W., J. Mol. Spec. **96**, 200 (1982).

Lawley, K. P., *Photodissociation and Photionization*. (John Wiley&Sons, NEW YORK, 1985).

Lee, E. G., Seto, J. Y., Hirao, T., Bernath, P. F., and LeRoy, R. J., J. Mol. Spectrosc. **194**, 197 (1999).

Lefebvre - Brion, H. and Field, R. W., *The Spectra and Dynamics of Diatomic Molecules*, Revised and Enlarged edition ed. (Elsevier Academic Press, 2004).

LeRoy, R. J., Huang, Y., and Jary, C., J. Chem. Phys. **125**, 164310 (2006).

LeRoy, R. J., LEVEL 8.0: A computer program for solving the radial Schrodinger equation for bound and quasibound levels (University of Waterloo Physics Research Report 2007).

LeRoy, R. J. and Henderson, R., Mol. Phys. **105**, 663 (2007).

Li, L. and Lyyra, A. M., Spectrochimica Acta Part A **55**, 2147 (1999).

Light, J. C., Hamilton, I. P., and Lill, J. V., J. Chem. Phys **82**, 1400 (1985).

Lill, J. V., Parker, G. A., and Light, J. C., Chem. Phys. Lett. **89**, 483 (1982).

Linton, C., Martin, F., Russier, I., Ross, A. J., Crozet, P., Churassy, S., Bacis, R., and J.Mol.Spectrosc. **175**, 340 (1996).

Lisdat, C., Duleiu, O., Knockel, H., and Tiemann, E., Eur. Phys. J. D **17**, 319 (2001).

Lyyra, A. M., Luh, W. T., Li, L., Wang, H., and Stwalley, W. C., J. Chem. Phys. **92**, 43 (1990).

Lyyra, A. M., Wang, H., Whang, T.-J., Stwalley, W. C., and L.Li, Phys. Rev. Lett. **66**, 2724 (1991).

Magnier, S., private communication.

Manaa, M. R., J. Quant. Chem. **75**, 693 (1999).

Manaa, M. R., Ross, A. J., Martin, F., Crozet, P., Lyyra, A. M., Li, L., Amiot, C., and Bergeman, T., **117**, 11208 (2002).

McCaffery, A. J., Reid, K. L., and Whitaker, B. J., Phys. Rev. Lett. **61**, 2085 (1988).

McCaffery, A. J., Richardson, J. P., Wilson, R. J., and Wynn, M. J., J.Phys.B **26**, 705 (1993).

Michelson, A. and Morley, E., American Journal of Science **34** (203), 333 (1887).

Nesmeyanov, A. N., *Vapor Pressure of the Chemical Elements*. (1963).

Nishimiya, N., Yasuda, Y., Yukiya, T., and Suzuki, M., J. Mol. Spectrosc. **255**, 194 (2009).

Okada, N., Kasahara, S., Ebi, T., Baba, M., and Kato, H., J. Chem. Phys. **105**, 3458 (1996).

Ottinger, C., Velasco, R., and Zare, R. N., J. Chem. Phys. **52**, 1636 (1970).

Ottinger, C. and Poppe, D., Chem. Phys.Lett. **8**, 513 (1971).

Ottinger, C. and Schroder, M., J.Phys.B **13**, 4163 (1980).

Palmer, B. A., Keller, R. A., and Engleman, R., Jr., LASL Report No. LA-8251-MS (Los Alamos Scientific Laboratory, Los Alamos, NM, 1980).

Qi, P., Bai, J., Ahmed, E. H., Lyyra, A. M., Kotochigova, S., Ross, A. J., Effantin, C., Zalicki, P., Vigue, J., Chawla, G., Field, R. W., Whang, T. J., Stwalley, W. C., Knockel, H., Tiemann, E., Shang, J., Li, L., and Bergeman, T., J. Chem. Phys. **127**, 044301 (2007).

Raab, M., Honing, G., Demtroder, W., and Vidal, C. R., J. Chem. Phys. **76**, 4370 (1982).

Rees, A. L. G., Proc.Phys.Soc(London) **59**, 998 (1947).

Reid, K. L. and McCaffery, A. J., J.Chem.Phys. **96**, 5789 (1993).

Richards, W. G., Trivedi, H. P., and Cooper, D. L., *Spin-orbit coupling in molecules*. (Clarendon Press, Oxford, 1981).

Ross, A. J., Effantin, C., Incan, J. d., and Barrow, R. F., J. Phys. B. **19**, 1449 (1986).

Ross, A. J., Crozet, P., Effantin, C., d'Incan, J., and Barrow, R. F., J. Phys. B **20**, 6225 (1987).

Rowe, M. D. and McCaffery, A. J., Chem. Phys. **43**, 35 (1979).

Rydberg, R., Physik. **73**, 376 (1931).

Rydberg, R., Z. Physik **80**, 514 (1933).

Salami, H., Bergeman, T., Beser, B., Bai, J., Ahmed, E. H., Kotochigova, S., Lyyra, A. M., Huennekens, J., Lisdat, C., Stolyarov, A. V., Dulieu, O., Crozet, P., and Ross, A. J., Phys. Rev. A **80**, 022515 (2009).

Skinner, D. R. and Whitcher, R. E., J. Phys. E. **5**, 237 (1972).

Smith, T. A. B. N., Karp, A. W., and Pritchard, D. E., J. Appl. Phys. **74**, 3324 (1981).

Stert, V. and Fischer, R., Appl. Phys. **17**, 151 (1978).

Sun, H. and Huennekens, J., J. Chem. Phys. **97**, 4714 (1992).

Teets, R., Feinberg, R., Hansch, T. W., and Schawlow, A. L., Phys. Rev. Lett. **37** (11), 683 (1976).

Tiesinga, E., Williams, C. J., and Julienne, P. S., Phys. Rev. A **57**, 4257 (1998).

Urbanski, K., Antonova, S., Lyyra, A. M., Yiannopoulou, A., and Stwalley, W. C., J.Chem.Phys. **104**, 2813 (1996).

Vasilenko, L. S., Chebotayev, V. P., and Shishaev, A. V., JEPT Lett. **12** (1970).

Vidal, C. R. and Cooper, J., J. Appl. Phys. **40**, 3370 (1969).

Wang, X., Magnes, J., Lyyra, A. M., Ross, A. J., Martin, F., Dove, P. M., and Roy, R. J. L., J. Chem. Phys. **117**, 9339 (2002).

Whang, T.-J., Stwalley, W. C., Li, L., Lyyra, A. M., and J. Chem. Phys. **97**, 7211 (1992).

Wickenmeier, W., Diemer, U., Wahl, M., Raab, M., Demtroder, W., and Muller, W., J. Chem. Phys. **82**, 5354 (1985).

Wieman, C. and Hansch, T. W., Phys. Rev. Lett. **36**, 1170 (1976).

Wolfe, C., Ph. D. Thesis, Lehigh University, 2010.

Wolfe, C., Ashman, S., Bai, J., Beser, B., Ahmed, E. H., Lyyra, A. M., and Huennekens, J., J. Chem. Phys. **134**, 174301 (2011).

Xie, X. and Field, R. W., Chem. Phys. **99**, 337 (1983).

Xie, X. and Field, R. W., J.Mol.Spectrosc. **117**, 228 (1986).

Zaharova, J., Taminis, M., Ferber, R., Drozdova, A. N., E.A.Pazyuk, and Stolyarov, A. V., Phys. Rev. A **79**, 012508 (2009).

APPENDIX

Identified fluorescence spectral lines for the Rb_2 polarization experiment. The unit for the fluorescence lines is cm^{-1}. The n' values give the energy eigenvalue number calculated for the upper $A^1\Sigma_u^+ \sim b^3\Pi_u$ state.

v"=0	J"=71	n'=50	
P	Fluorescence	R	Fluorescence
89	11378.469	87	11386.315
87	11380.276	85	11387.948
85	11382.005	83	11389.501
83	11383.655	81	11390.982
81	11385.322	79	11392.472
79	11386.77	77	11393.742
77	11388.199	75	11394.996
75	11389.552	73	11396.177
73	11390.832	71	11397.283
71	11392.046	69	11398.309
69	11393.187	67	11399.274
67	11394.257	65	11400.172
65	11395.265	63	11401.006
63		61	11401.776
61	11397.107	59	11402.494
59	11397.951	57	11403.158
57	11398.736	55	11403.773
55	11399.483	53	11404.336
53	11400.172	51	11404.862
51	11400.854	49	11405.35
49	11401.483	47	11405.802
47	11402.077	45	11406.223
45	11402.646	43	11406.61
43	11403.173	41	11406.968
41	11403.683	39	11407.297
39	11404.168	37	11407.619
37	11404.628	35	11407.9
35	11405.066	33	11408.162
33	11405.482	31	11408.397
31	11405.878	29	11408.612
29	11406.251	27	11408.81
27	11406.605	25	11408.986

25	11406.936	23	11409.138
23	11407.259	21	11409.275
21	11407.562	19	11409.395
19	11407.834	17	11409.49
17	11408.092	15	11409.565
15	11408.328	13	11409.625
v"=0	J"=71	n'=51	
P	Fluorescence	R	Fluorescence
93	11402.008	91	11410.208
91	11402.903	89	11410.925
89	11403.796	87	11411.648
87	11404.699	85	11412.369
85	11405.606	83	11413.106
83	11406.529	81	11413.854
81	11407.463	79	11414.613
79	11408.413	77	11415.389
77	11409.381	75	11416.175
75	11410.361	73	11416.981
73	11411.359	71	11417.805
71	11412.373	69	11418.638
69	11413.389	67	11419.485
67	11414.42	65	11420.339
65	11415.451	63	11421.197
63	11416.493	61	11422.059
61	11417.529	59	11422.919
59	11418.561	57	11423.773
57	11419.587	55	11424.62
v"=0	J"=71	n'=52	
P	Fluorescence	R	Fluorescence
79	11435.465	77	11442.438
75	11439.143	73	11445.764
73	11440.727	71	11447.175
71	11442.329	69	11448.603
69	11443.879	67	11449.975
67	11445.365	65	11451.287
65	11446.784	63	11452.529
63	11448.135	61	11453.701
61	11449.408	59	11454.799
59	11450.61	57	11455.826
57	11451.734	55	11456.769
55	11452.783	53	11457.642
53	11453.756	51	11458.439
51	11454.657	49	11459.162
49	11455.491	47	11459.817
47	11456.259	45	11460.41
45	11456.971	43	11460.945

43	11457.627	41	11461.423
41	11458.238	39	11461.854
39	11458.803	37	11462.241
35	11460.017	33	11463.101
v"=0	J"=71	n'=56	
P	Fluorescence	R	Fluorescence
97	11511.197	95	11519.739
95	11512.469	93	11520.833
93	11513.881	91	11522.077
91	11515.338	89	11523.36
89	11516.83	87	11524.676
87	11518.348	85	11526.019
85	11519.886	83	11527.384
83	11521.44	81	11528.764
81	11523	79	11530.146
79	11524.555	77	11531.526
77	11526.103	75	11532.902
75	11527.642	73	11534.263
73	11529.16	71	11535.606
71	11530.657	69	11536.925
69	11532.122	67	11538.217
67	11533.556	65	11539.476
65	11534.958	63	11540.703
63	11536.326	61	11541.893
61	11537.654	59	11543.044
59	11538.943	57	11544.157
57	11540.186	55	11545.223
55	11541.389	53	11546.247
53	11542.54	51	11547.228
51	11543.658	49	11548.165
49	11544.725	47	11549.054
47	11545.748	45	11549.901
45	11546.72	43	11550.696
43	11547.645	41	11551.441
v"=0	J"=71	n'=57	
P	Fluorescence	R	Fluorescence
95	11540.292	93	11548.662
93	11542.279	91	11550.476
91	11544.198	89	11552.219
89	11546.013	87	11553.862
87	11547.729	85	11555.4
85	11549.329	83	11556.829
83	11550.821	81	11558.143
81	11552.196	79	11559.345
79	11553.464	77	11560.438
77	11554.632	75	11561.428

75	11555.709	73	11562.333
73	11556.707	71	11563.156
71	11557.636	69	11563.909
69	11558.511	67	11564.608
67	11559.333	65	11565.252
65	11560.112	63	11565.857
63	11560.857	61	11566.422
61	11561.568	59	11566.959
57	11562.916	55	11567.953
55	11563.557	53	11568.416
53	11564.182	51	11568.863
51	11564.787	49	11569.293
49	11565.379	47	11569.707
47	11565.96	45	11570.111
45	11566.516	43	11570.49
43	11567.068	41	11570.862
41	11567.599	39	11571.217
39	11568.12	37	11571.559
37	11568.621	35	11571.883
35	11569.116	33	11572.201
33	11569.593	31	11572.495
31	11570.049	29	11572.77
29	11570.49	27	11573.041
25	11571.319	23	11573.508
23	11571.703	21	11573.716
21	11572.064	19	11573.901
19	11572.401	17	11574.058
v"=0	J"=71	n'=58	
P	Fluorescence	R	Fluorescence
87	11560.415	85	11568.085
85	11561.638	83	11569.135
83	11562.865	81	11570.19
81	11564.142	79	11571.291
79	11565.464	77	11572.438
77	11566.829	75	11573.626
75	11568.221	73	11574.84
73	11569.631	71	11576.075
71	11571.047	69	11577.319
69	11572.468	67	11578.563
67	11573.88	65	11579.792
65	11575.278	63	11581.018
63	11576.65	61	11582.217
61	11577.996	59	11583.391
59	11579.315	57	11584.533
57	11580.601	55	11585.64
55	11581.849	53	11586.711
53	11583.061	51	11587.744

51	11584.227	49	11588.733
49	11585.358	47	11589.686
47	11586.447	45	11590.595
45	11587.489	43	11591.461
43	11588.488	41	11592.282
41	11589.447	39	11593.065
39	11590.361	37	11593.801
35	11592.05	33	11595.132
v"=0	J"=71	n'=59	
P	Fluorescence	R	Fluorescence
89	11593.883	87	11601.729
87	11595.977	85	11603.651
85	11598.057	83	11605.554
83	11600.097	81	11607.422
81	11602.097	79	11609.242
79	11604.055	77	11611.027
77	11605.962	75	11612.761
75	11607.821	73	11614.443
73	11609.618	71	11616.063
71	11611.054	69	11617.328
69	11613.153	67	11619.249
67	11614.765	65	11620.682
65	11616.38	63	11622.126
63	11617.962	61	11623.532
61	11619.504	59	11624.896
59	11620.996	57	11626.219
57	11622.447	55	11627.485
55	11623.846	53	11628.716
53	11625.2	51	11629.89
51	11626.507	49	11631.015
49	11627.764	47	11632.097
47	11628.976	45	11633.127
45	11630.134	43	11634.112
43	11631.249	41	11635.042
41	11632.314	39	11635.933
39	11633.325	37	11636.769
37	11634.292	35	11637.556
35	11635.215	33	11638.299
33	11636.088	31	11638.989
v"=0	J"=71	n'=60	
P	Fluorescence	R	Fluorescence
87	11606.43	85	11614.103
85	11607.194	83	11614.692
83	11607.926	81	11615.248
81	11608.643	79	11615.789
79	11609.332	77	11616.306

77	11610.008	75	11616.805
75	11610.464	73	11617.084
73	11611.127	71	11617.576
71	11611.879	69	11618.149
v"=0	J"=71	n'=61	
P	Fluorescence	R	Fluorescence
97	11627.275	95	11635.816
95	11629.317	93	11637.684
93	11631.343	91	11639.539
91	11633.347	89	11641.37
89	11635.329	87	11643.176
87	11637.272	85	11644.943
85	11639.176	83	11646.674
83	11641.036	81	11648.355
81	11642.839	79	11649.981
79	11644.59	77	11651.558
77	11646.249	75	11653.039
75	11647.962	73	11654.579
73	11649.519	71	11655.963
71	11651.016	69	11657.287
69	11652.447	67	11658.544
67	11653.807	65	11659.726
65	11655.09	63	11660.833
63	11656.299	61	11661.865
61	11657.433	59	11662.824
59	11658.493	57	11663.705
57	11659.498	55	11664.546
55	11660.403	53	11665.261
v"=0	J"=71	n'=63	
P	Fluorescence	R	Fluorescence
		81	11688.323
		79	11689.323
		77	11691.567
		75	11693.128
75	11688.022	73	11694.647
73	11689.668	71	11696.113
71	11691.26	69	11697.528
69	11692.801	67	11698.892
67	11694.288	65	11700.206
65	11695.721	63	11701.459
63	11697.097	61	11702.658
61	11698.416	59	11703.805
v"=0	J"=71	n'=64	
P	Fluorescence	R	Fluorescence
89	11710.926	87	11718.767

87	11711.811	85	11719.485
		83	11720.139
		81	11720.758
81	11714.202	79	11721.35
79	11714.96	77	11721.935
77	11715.703	75	11722.511
75	11716.446	73	11723.075
73	11717.186	71	11723.634
71	11717.921		
69	11718.635	67	11724.739
67	11719.358	65	11725.277
65	11720.091	63	11725.837
63	11720.815	61	11726.381
61	11721.533	59	11726.913
59	11722.257	57	11727.465
57	11722.975	55	11728.009
55	11723.694	53	11728.55
		51	11729.18
51	11725.283	49	11729.786
49	11726.225	47	11730.458
		45	11731.188
v"=0	J"=71	n'=65	
P	Fluorescence	R	Fluorescence
85	11719.258	83	11726.758
83	11721.304	81	11728.629
81	11723.312	79	11730.458
		77	11732.239
77	11727.188	75	11733.992
75	11729.057	73	11735.684
73	11730.873	71	11737.325
71	11732.645	69	11738.919
69	11734.355	67	11740.454
67	11736.016	65	11741.938
65	11737.625	63	11743.366
63	11739.18	61	11744.744
61	11740.678	59	11746.066
59	11742.128	57	11747.338
57	11743.518	55	11748.553
55	11744.853	53	11749.717
53	11746.141	51	11750.823
51	11747.365	49	11751.878
49	11748.542	47	11752.872
47	11749.668	45	11753.819
45	11750.741	43	11754.712
43	11751.76	41	11755.554
41	11752.727	39	11756.346
v"=0	J"=71	n'=67	

P	Fluorescence	R	Fluorescence
87	11765.604	85	11773.278
85	11766.932	83	11774.435
83	11768.346	81	11775.672
81	11769.837	79	11776.985
		77	11778.361
77	11772.987	75	11779.779
75	11774.609	73	11781.227
73	11776.244	71	11782.686
71	11777.874	69	11784.147
69	11779.5	67	11785.595
67	11781.102	65	11787.021
		63	11788.423
63	11784.227	61	11789.792
61	11785.738	59	11791.128
59	11787.215	57	11792.427
57	11788.649	55	11793.686
55	11790.04	53	11794.9
		51	11796.075
51	11792.698	49	11797.204
49	11793.956		
47	11795.172	45	11799.322
45	11796.339	43	11800.312
43	11797.456	41	11801.255
v"=0	J"=71	n'=69	
P	Fluorescence	R	Fluorescence
85	11818.248	83	11825.748
83	11819.367	81	11826.693
81	11820.443	79	11827.593
79	11821.538	77	11828.517
77	11822.663	75	11829.463
75	11823.808	73	11830.435
73	11824.984	71	11831.434
71	11826.178	69	11832.457
69	11827.399	67	11833.498
67	11828.626	65	11834.547
65	11829.965	63	11835.61
63	11831.103	61	11836.677
61	11832.35	59	11837.74
59	11833.582	57	11838.796
57	11834.806	55	11839.841
55	11836.014	53	11840.871
53	11837.201	51	11841.888
51	11838.365	49	11842.874
49	11839.505	47	11843.835
47	11840.615	45	11844.767
45	11841.696	43	11845.663

43	11842.707	41	11846.501
41	11843.747	39	11847.36
v"=0	J"=71	n'=70	
P	Fluorescence	R	Fluorescence
83	11840.99	81	11848.314
81	11842.908	79	11850.054
79	11844.755	77	11851.733
77	11846.531	75	11853.34
75	11848.242	73	11854.87
73	11849.879	71	11856.332
71	11851.448	69	11857.725
69	11852.94	67	11859.037
67	11854.326	65	11860.244
65	11855.718	63	11861.464
63	11856.992	61	11862.557
61	11858.19	59	11863.584
59	11859.33	57	11864.541
57	11860.398	55	11865.437
55	11861.407	53	11866.267
v"=0	J"=71	n'=72	
P	Fluorescence	R	Fluorescence
85	11882.337	83	11889.828
83	11884.38	81	11891.704
81	11886.434	79	11893.583
79	11888.438	77	11895.411
77	11890.393	75	11897.187
75	11892.293	73	11898.914
73	11894.137	71	11900.588
71	11895.929	69	11902.2
69	11897.663	67	11903.76
67	11899.341	65	11905.261
65	11900.958	63	11906.706
63	11902.517	61	11908.087
61	11904.011	59	11909.405
59	11905.443	57	11910.661
57	11906.807	55	11911.849
v"=0	J"=71	n'=74	
P	Fluorescence	R	Fluorescence
79	11933.644	77	11940.618
77	11935.457	75	11942.256
75	11937.324	73	11943.948
73	11939.033	71	11945.486
71	11940.79	69	11947.063
69	11942.512	67	11948.604

67	11944.205	65	11950.125
65	11945.861	63	11951.6
63	11947.472	61	11953.037
61	11949.046	59	11954.439
v"=0	J"=71	n'=76	
P	Fluorescence	R	Fluorescence
79	11978.136	77	11985.107
77	11979.605	75	11986.404
75	11981.093	73	11987.718
73	11982.595	71	11989.044
71	11984.097	69	11990.371
69	11985.602	67	11991.698
67	11987.098	65	11993.016
65	11988.577	63	11994.316
63	11990.036	61	11995.602
61	11991.477	59	11996.864
59	11992.887	57	11998.098
v"=0	J"=71	n'=77	
P	Fluorescence	R	Fluorescence
79	12004.846	77	12011.821
77	12006.498	75	12013.296
75	12008.073	73	12014.695
73	12009.558	71	12016
71	12010.946	69	12017.218
69	12012.25	67	12018.342
67	12013.462	65	12019.376
65	12014.592	63	12020.333
63	12015.648	61	12021.214
61	12016.629		
59	12017.547	57	12022.762
v"=0	J"=71	n'=79	
P	Fluorescence	R	Fluorescence
73	12055.755	71	12062.209
71	12057.766	69	12064.039
69	12059.514	67	12065.611
67	12061.21	65	12067.13
65	12062.835	63	12068.579
v"=0	J"=71	n'=81	
P	Fluorescence	R	Fluorescence
75	12096.39	73	12103.012
73	12098.272	71	12104.72
71	12100.116	69	12106.389
v"=0	J"=71	n'=84	

P	Fluorescence	R	Fluorescence
73	12166.826	71	12173.279
71	12168.014		
v"=0	J"=84	n'=50	
P	Fluorescence	R	Fluorescence
86	11381.139	84	11388.724
84	11382.829	82	11390.239
80	11386.025	78	11393.086
78	11387.485	76	11394.37
76	11388.874	74	11395.585
v"=0	J"=84	n'=51	
P	Fluorescence	R	Fluorescence
		84	11412.748
84	11406.04	82	11413.467
v"=0	J"=84	n'=54	
P	Fluorescence	R	Fluorescence
86	11475.677	84	11483.258
84	11477.513	82	11484.926
v"=0	J"=84	n'=55	
P	Fluorescence	R	Fluorescence
108	11480.048	106	11489.525
106	11481.744	104	11491.061
104	11483.798	102	11492.944
102	11485.799	100	11494.771
100	11487.63	98	11496.427
98	11489.373	96	11497.998
96	11491.011	94	11499.463
94	11492.542	92	11500.824
92	11493.975	90	11502.082
90	11495.309	88	11503.241
88	11496.546	86	11504.31
86	11497.703	84	11505.289
84	11498.782	82	11506.192
82	11499.795	80	11507.029
80	11500.743	78	11507.799
78	11501.635	76	11508.515
76	11502.471	74	11509.181
74	11503.271	72	11509.805
72	11504.027	70	11510.387
70	11504.749	68	11510.933
68	11505.441		
66	11506.104		

v"=0	J"=84	n'=56	
P	Fluorescence	R	Fluorescence
		84	11526.672
84	11520.648	82	11528.061
v"=0	J"=84	n'=63	
P	Fluorescence	R	Fluorescence
		96	11675.659
		94	11677.214
		92	11678.914
92	11672.529	90	11680.636
90	11674.432	88	11682.365
88	11676.327	86	11684.089
86	11678.214	84	11685.8
84	11680.075		
82	11682.022	80	11689.326
80	11683.705		
78	11685.465		
v"=0	J"=84	n'=67	
P	Fluorescence	R	Fluorescence
86	11766.246	84	11773.833
84	11767.617	82	11775.03
82	11768.96	80	
v"=0	J"=84	n'=72	
P	Fluorescence	R	Fluorescence
		84	11888.664
84	11883.21		

Identified data from the Cs_2 polarization spectroscopy experiment:

J'	n'	Term Values
97	261	11118.486
99	261	11122.149
97	265	11156.622
99	265	11160.241
97	270	11194.729
99	270	11198.394
101	270	11202.138
97	274	11232.584
99	274	11236.237
101	274	11239.967
97	278	11270.113
99	278	11273.853
101	278	11277.638
83	284	11285.002
85	284	11288.07
99	283	11311.705
101	283	11315.358
81	289	11318.914
83	289	11321.946
85	288	11325.056
56	294	11327.033
57	294	11328.081
58	294	11329.152
59	294	11330.232
60	294	11331.335
61	294	11332.458
62	294	11333.597
63	294	11334.751
64	294	11335.931
65	294	11337.117
66	294	11338.331
67	294	11339.554
68	294	11340.801
69	294	11342.062
71	294	11344.634
72	294	11345.941
73	294	11347.277
74	294	11348.626
99	288	11348.965
75	294	11349.993
76	294	11351.367

101	287	11352.689
77	294	11352.775
79	294	11355.623
51	298	11358.395
81	294	11358.542
82	294	11360.021
53	298	11360.302
83	294	11361.526
55	298	11362.275
84	294	11363.038
57	298	11364.321
85	294	11364.58
86	294	11366.119
59	298	11366.43
87	294	11367.699
61	298	11368.624
62	298	11369.744
63	298	11370.883
89	294	11370.887
64	298	11372.043
65	298	11373.214
91	294	11374.137
66	298	11374.409
67	298	11375.613
68	298	11376.846
93	293	11377.455
69	298	11378.072
70	298	11379.349
71	298	11380.631
72	298	11381.925
73	298	11383.248
74	298	11384.577
75	298	11385.935
76	298	11387.297
99	293	11387.82
77	298	11388.687
78	298	11390.089
101	293	11391.41
79	298	11391.518
80	298	11392.95
81	298	11394.418
82	298	11395.886
83	298	11397.393
105	293	11398.784
84	298	11398.896
85	298	11400.442
58	302	11401.265
86	298	11401.985

59	302	11402.327
107	292	11402.573
60	302	11403.402
87	298	11403.555
61	302	11404.498
88	298	11405.139
62	302	11405.616
63	302	11406.751
89	298	11406.754
64	302	11407.904
65	302	11409.074
91	297	11410.019
66	302	11410.259
67	302	11411.469
68	302	11412.722
93	297	11413.36
69	302	11413.941
70	302	11415.206
71	302	11416.487
95	297	11416.775
72	302	11417.786
73	302	11419.108
97	297	11420.262
74	302	11420.438
75	302	11421.8
76	302	11423.176
99	297	11423.832
77	302	11424.574
78	302	11425.99
101	297	11427.479
80	302	11428.868
81	302	11430.345
121	291	11430.974
82	302	11431.853
83	302	11433.345
84	302	11434.886
105	297	11435
123	291	11435.307
85	302	11436.424
86	302	11437.988
107	297	11438.876
87	302	11439.578
88	302	11441.189
89	302	11442.811
90	302	11444.463
91	301	11446.123
92	301	11447.809
93	301	11449.518

94	301	11451.238
95	301	11452.987
91	303	11453.432
97	301	11456.531
93	303	11456.8
99	301	11460.17
101	301	11463.863
120	296	11465.989
103	301	11467.644
122	296	11470.458
105	301	11471.5
91	307	11485.331
93	307	11488.649
120	300	11502.851
121	300	11505.099
122	300	11507.343
85	311	11511.509
107	306	11513.766
87	311	11514.606
91	311	11521.01
120	305	11540.075
122	305	11544.416
105	310	11545.747
107	310	11549.583